ABSTRACT

Title of Dissertation:	DISTRIBUTED FIBER-OPTIC SENSORS FOR PRESSURE AND STRAIN MEASUREMENTS DURING SLAMMING OF A FLEXIBLE PLATE
	Kit Pan Wong, Ph.D. Dissertation, 2022
Dissertation Directed By:	Professor Miao Yu, Department of Mechanical Engineering and Institute for Systems Research, University of Maryland, College Park, MD

The investigation of fluid-structure interaction during the impact of a flexible plate on a water surface has received much attention. Measurement of highly transient, distributed strain and pressure of the plate during the slamming event is of great interest. Multiplexed fiber Bragg grating (FBG) strain sensors provide a promising solution for such measurement since these sensors are inherently waterproof and are immune to electromagnetic interference. However, in order to monitor the highly transient, distributed strain and pressure responses (up to 20 kHz), high-speed interrogation of multiplexed sensors is required, which is challenging by using commercial optical interrogators. Furthermore, it is challenging to use conventional piezoelectric sensors for pressure measurement on a flexible plate due to the intrusiveness of their size.

In this dissertation work, a distributed fiber optic sensor system is explored for strain and pressure measurement on a flexible plate during slamming. First, a high-speed optical interrogation system for multiplexed FBG strain sensors and Fabry-Perot pressure sensors is developed. The interrogation system employs a piezoelectric-transducer-controlled Fabry-Perot tunable filter. By operating the tunable filter at its resonant frequency and demodulating the sensor signal based on

a peak tracing method, the system can operate at the interrogation speed of 100 kHz, an interrogation range of 98 nm, and an interrogation resolution of 5 pm. To demonstrate its capability, the interrogation system is used to monitor the vibrational responses of a cantilever plate under impact loading and the measurement of vibration modes up to 6.785 kHz. The system is also demonstrated to be able to interrogate Fabry-Perot acoustic pressure sensors for up to 20 kHz. Second, miniature Fabry-Perot pressure sensors with temperature compensation are developed based on the additive manufacturing technique. Two types of miniature Fabry-Perot pressure sensors (a single cavity FP sensor and a dual cavity FP sensor) were designed and developed. Due to the large coefficient of thermal expansion of the polymer material, the change of the optical path length induced by the temperature can result in a large error in the pressure measurement. By characterizing the pressure and temperature sensitivity of the sensor, the experimental result shows the temperature compensated pressure response of the FP sensor agreed well with the reference sensor. Finally, the experimental study of the impact of a flexible plate on a water surface is carried out by using the distributed fiber optic strain and pressure measurement system. With multiplexed FBG strain sensors and FP pressure sensors mounted on the flexible plate, the dynamic strain and pressure responses occurred on the plate during the slamming event were successfully monitored. The maximum strain increased with increasing impact speeds, which was in good agreement with the behavior of the measured maximum deflection. The high-speed spectral domain optical interrogation system with FBG strain sensors and FP sensors can serve as a useful measurement tool for a better understanding of the fluid-structure interaction.

DISTRIBUTED FIBER-OPTIC SENSOR FOR PRESSURE AND STRAIN MEASUREMENTS DURING SLAMMING OF A FLEXIBLE PLATE

by

Kit Pan Wong

Dissertation submitted to the Faculty of the Graduate School of the
University of Maryland, College Park, in partial fulfillment
of the requirement for the degree of
Doctor of Philosophy
2022

Advisory Committee:
Professor Miao Yu, Chair
Professor James Duncan
Professor Kenneth Kiger
Professor Nikhil Chopra
Professor Stuart Laurence (Dean's Representative)

Dedication

To my parents and family

Acknowledgments

First and most important, I would like to express my deepest gratitude to thank my advisor, Professor Miao Yu for her unlimited support and guidance throughout my Ph.D. study. You are a light that has guided me through graduate school. You are always on my side and I can always rely on your advice. I am beyond grateful to her for providing this most important opportunity in my life! It was a great experience to learn from her through this journey, not only in engineering but also in the value of commitment. The most valuable lesson I learned from her is work-ethic. The education I have learned from her has served me well in both graduate school and industry. I will treasure the memories I have working with her.

I am also grateful to my mentor, Professor Hyun-Tae Kim. I could not finished the dissertation without his enormous help. Thank you for training me when I enrolled in Ph. D program. I would definitely quit the program if you did not help me. The transition between undergraduate and graduate school was one of the most challenging I had, thank you again for helping me through this journey.

Next, I would like to thank my fellow lab-mates in the Sensors and Actuators Laboratory: Hyungdae Bae, Randy Ganye, Keshav Rajasejaran, Amirhossein Yazdkhasti, Liuxian Zhao, Bala Sudhakar, for all the collaborations and discussions. I could not finish my research without your help. How lucky I am to be surrounded by such remarkable colleagues.

I also would like to thank the professors and students from the hydro-dynamic lab: Professor James Duncan, Professor Kenneth Kiger, Professor An Wang, Dr. Xinan Liu, Samuel En-Yih Lee, Chang Liu, and Martin Erinin. Thank you for providing the all hydro-dynamic facilities. Especially An and Sam, thank you for helping me to measure slamming experiments and

educating me on the knowledge of hydrodynamic. It was an absolute privilege to work with you as colleagues and mentors.

Thank you to the rest of the members of my dissertation committee: Nikhil Chopra and Professor Stuart Laurence. Thank Laurence for providing a rare opportunity to use a hypersonic tunnel from the High-Speed Aerodynamics and Propulsion Laboratory.

Finally, thank you to my family and friends who suffered so many moods from me. Thank you for your patience and support. It has been a wonderful journal in my life. I am so immensely proud of everything the team has achieved in collaboration. Thank you to the colleagues who inspire me every day with their commitment to pushing the boundaries of science further.

Table of Contents

List of Figures

1. Introduction

1.1 Problem of interest

Tailor-made miniature fiber-optic pressure sensors and a high-speed optical sensing interrogation system are desirable for experimental investigation of fluid-structure interaction during the impact of a flexible plate on a water surface. These slamming phenomena are common in boats, dams, and bridges. Those structures are damaged by suffering impact from the water waves that involve large dynamic force, pressure, and water spray generation. The investigation of slamming phenomena is challenging due to the large and violent motions of the hulls and the water-free surface. Monitoring structural response is vital for a better understanding of the complex fluid-structure interaction during the slamming event.

Structural health monitoring is often performed by using a large array of electrical strain gauges and pressure sensors. However, it is challenging to apply an electrical sensor to slamming experiments because the signal probably would be contaminated by the wet environment and suffered electromagnetic interference from the servo motor that controls the plate's motion. Moreover, instead of using a traditional electrical pressure sensor with a diaphragm of a millimeter-scale, a miniature pressure sensor with a diaphragm of a micrometer scale is a more attractive choice for pressure monitoring at high frequency. Optical sensing has become a more suitable alternative for such structural health monitoring owing to its advantages of small size, waterproof, immunity to electromagnetic interference, and multiplexing capability.

Optical sensing with fiber Bragg grating (FBG) sensors has been widely used for structural health monitoring in many applications. In structural health monitoring, the FBG sensor has been implemented for damage identification and structural condition assessment of the

structure, e.g., aircraft [1]–[4], railroads [5]–[8], dams [9]–[12], and bridges [13]–[17]. Wavelength-division multiplexing of a large number of FBG sensors can measure dynamic strain with ease of installation. However, most commercial optical interrogators require interrogation of multiplexed FBG sensors that have limited interrogation speed (up to tens of kHz), which makes it challenging to monitor dynamic structure response (up to 20 kHz) during the slamming event.

An optical interrogator employing a tunable wavelength filter and a broadband light source has become a more attractive alternative interrogation system for FBG sensors. This sensing system provides a compact and low-cost solution to high-speed and simultaneous interrogation of multiplexed FBG sensors. There have been a few research groups investigating the spectral-domain interrogation system based on a tunable wavelength filter and a broadband light source. The performance of the interrogation system is closely related to the tunable filter performance. For example, the interrogation speed, range, and resolution are influenced by the wavelength tuning speed, range, and fitness of tunable filters, respectively. An in-depth study of the spectral-domain interrogation system with a multiplexed FBG sensor can be useful in structural health monitoring.

Miniature fiber-optic pressure sensors exhibit great potential for structural health monitoring [18]–[22], biomedical [23]–[25], aerodynamic [26], [27], and acoustic [28]–[30], where minimal intrusiveness is required owing to its advantage of small size. The sensing mechanisms of fiber-optic pressure sensors are i). extrinsic Fabry-Perot Interferometer (EFPI), and ii). FBG. While FBG and FP-based fiber-optic sensors have been widely reported and used commercially, they still have drawbacks. EFPI is the most popular configuration for a pressure sensor, and most FP-based pressure sensors use silica or silicon as material. However, the

fabrication process often involves dangerous etching processes, such as hydrofluoric acid etching. Moreover, it is difficult to fabricate the sensor in batch, and the yield rate is low. The non-trivial fabrication process results in a high manufacturing cost. Hence, an alternative fabrication method for FP pressure sensors would be preferable.

Two-photon polymerization (2PP) direct laser writing (DLW) lithography is a micro-scale 3D printing that has been developed and used commercially over the past 20 years. This technique allows micro-scale 3D structure fabrication with feature sizes as small as 200 nm. This fabrication method provides a low-cost solution and flexibility of tailor-making structure for varying applications. However, the printing material is polymer-based, and its thermal stability and material strength are not as good as silica. Also, polymer-based pressure sensors are often suffered from temperature drift owing to its large coefficient of thermal expansion (CTE). Because of the material's properties, polymer-based pressure sensors result in large errors in pressure reading under temperature drift.

The focus of this dissertation work is to develop a spectral-domain interrogation system with multiplexed FBG strain sensors and miniature FP pressure sensors for the experimental investigation of the fluid-structure interaction of a flat plate slamming on the water surface.

1.2 Literature review

1.2.1 Spectral-domain interrogation

Spectral-domain interrogation is one of the widely used signal demodulation systems for FBG and FP fiber-optic sensors[31]–[34]. The interrogator consists of a broadband light source, tunable wavelength filter, function generator, and photodetector (PD). Figure 1-1 shows the block diagram and photograph of the full spectral interrogator. The light source is coupled to the sensor and tunable filter driven by the function generator. The output signal from the

tunable filter is coupled to the PD, which is connected to the data acquisition system for signal demodulation.

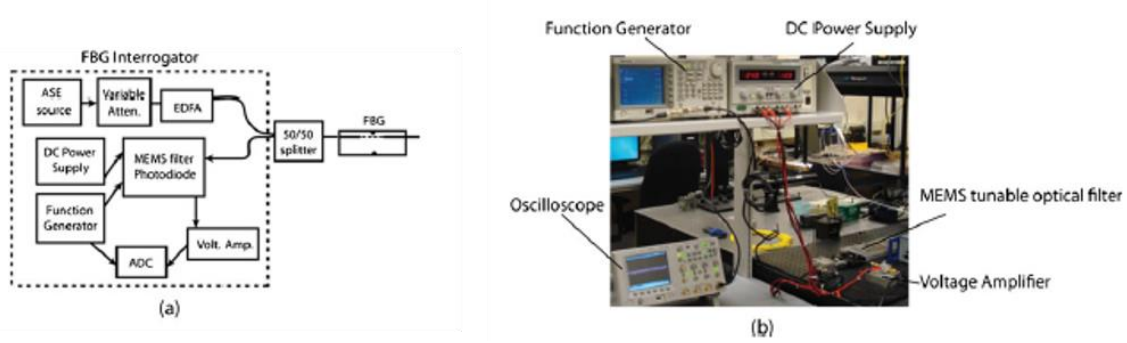

Figure 1-1: (a) Block diagram of FBG full-spectral interrogator. (b) Photograph of the interrogator [10].

The spectral-domain interrogation system has been widely used due to the following advantages. First, the operating wavelength range is highly flexible. Depending on the application and sensor configuration, such as multiplexed FBG sensors, the operating wavelength range can vary from 10 to 100 nm. Second, the FP sensor with multiple optical cavities requires a spectral domain for signal demodulation. The spectrum of the multi-cavity has a combination of distinctive optical frequencies, which can be obtained by applying the Fast Fourier transform to the spectrum. Figure 1-2 shows the spectrum of the multi-cavity FP sensor and the FFT result from the spectrum of the sensor.

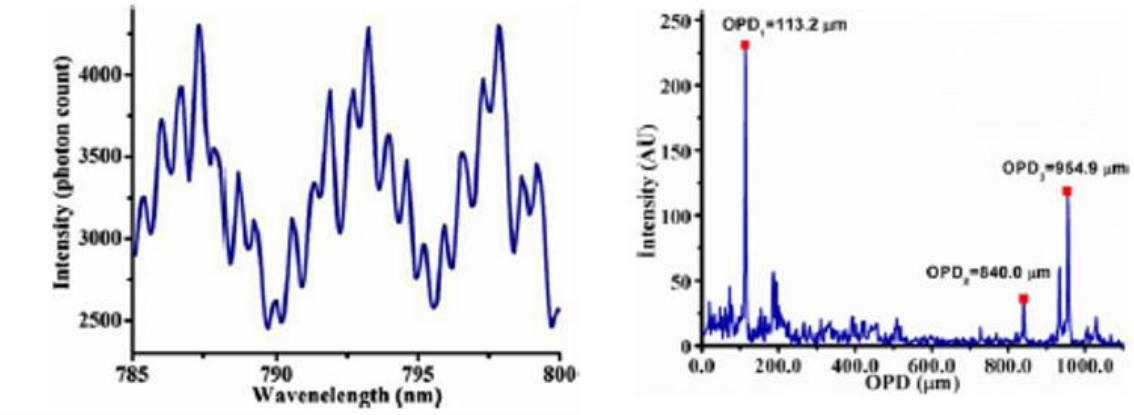

Figure 1-2: Spectrum of the multi-cavity FP sensor and FFT result from the spectrum [11].

The wavelength-tunable filter is a vital component of the interrogation system. The combined spectrum of the light source and tunable filter produces a narrowband tunable optical source for scanning the spectrum of the optical sensor[35]–[37] The time-varying transmitted optical power intensity is recorded for signal processing. Vella *et al.* demonstrated the high-speed spectral-domain interrogation of FBG sensors with electrostatic microelectromechanical systems (MEMS) tunable filter [38]–[40]. The electrostatic MEMS filter is an FP cavity consisting of two thin-film reflective membranes separated by a small air gap. The distance between the two membranes is controlled by applying voltage. Figure 1-3 shows the transmitted wavelength vs. applied voltage. Vella *et al.* showed the interrogation system captures FBG spectrum data at a rate of 100 kHz. The system offers high-speed sampling capability for spectral-domain interrogation. This is possible to monitor transient load with a standard signal processing method that has been used for a quasi-static spectral-domain interrogation system. Figure 1-4 shows the advantage of the high-speed sampling rate of the FBG spectrum. As a transient load is applied to the FBG sensor, the scanning frequency of the tunable filter operates at different frequencies from 500 Hz to 100 kHz. Silicon-ring-resonator-

based thermally tunable filter(SRRTF) is an alternative wavelength tunable filter for spectral-domain interrogation [41], [42]. Unlike the MEMS tunable filter, SRRTF does not require any moving part. The wavelength scanning is done by thermal expansion. Figure 1-5 shows the relationship between heating power and the transmitted wavelength.

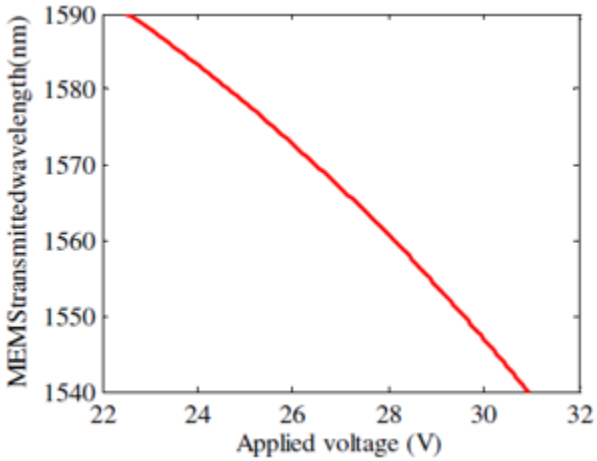

Figure 1-3: Electrostatic MEMS tunable filter static response.

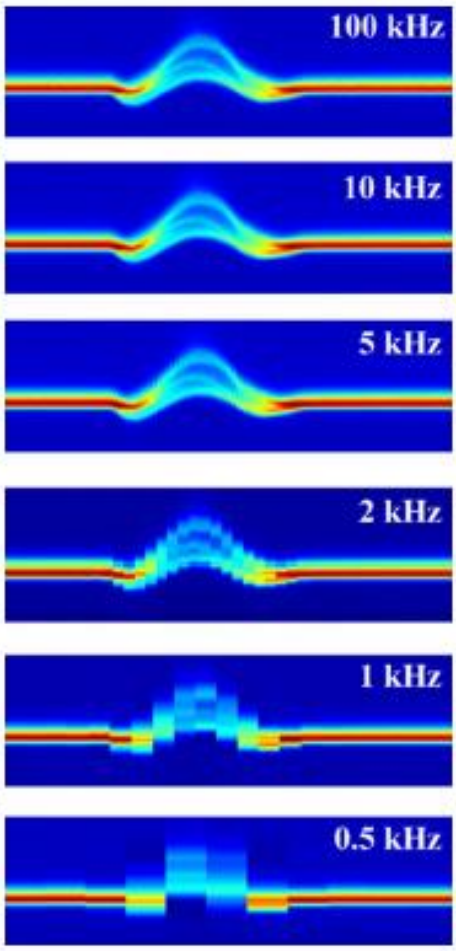

Figure 1-4: Down-sampled images from 100 kHz to 0.5 kHz [12].

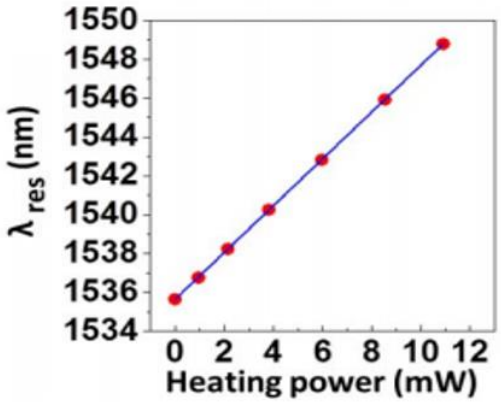

Figure 1-5: SRRTF static response.

1.2.2 Fiber Bragg Grating

Fiber Bragg Grating (FBG) is made of a periodic Fabry-Perot interferometer, which acts as a filter for certain wavelength filters. This is achieved by the periodic variation in the refractive index of the fiber core. The periodic changed refractive index is in phase with a certain wavelength, which is the only wavelength that will be reflected. The reflected wavelength (λ_B) is defined by the relationship of effective refractive index (n_e) of the grating in the fiber core and grating period (Λ) as Figure 1-6 shown.

$$\lambda_B = 2n_e\Lambda, \tag{1,1}$$

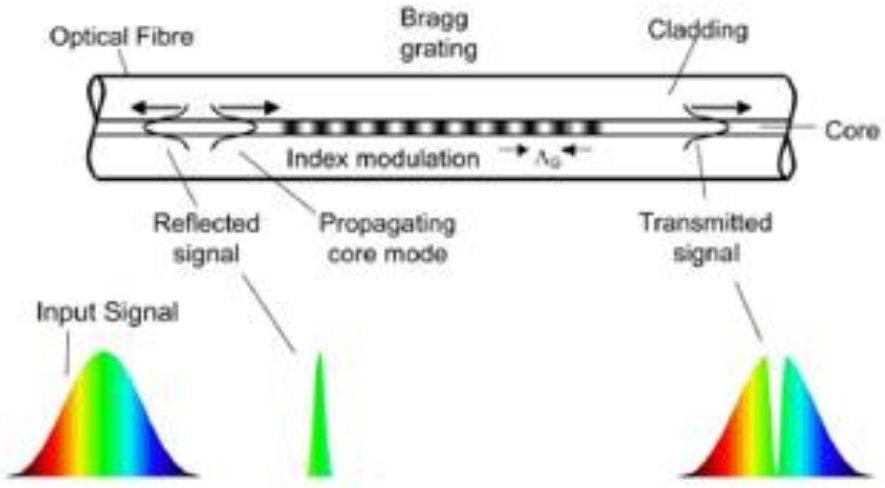

Figure 1-6: Schematic diagram of an FBG [14].

FBG sensors are widely used in many applications such as health monitoring [22], [43], [44], Civil engineering[45]–[51], and high-temperature detection[52]–[55]. The FBG is used as a

sensor because the Λ in equation (1.1) is dependent on the strain ($\Delta\varepsilon$) and temperature (ΔT). The λ_B shifts to the $\lambda_B + \Delta\lambda$ in the following relationship:

$$\Delta\lambda = k_\varepsilon \Delta\varepsilon + k_T \Delta T, \tag{1.2}$$

where k_ε and k_T are strain-optic and thermo-optic sensitivities, respectively.

FBG sensors can work either as a single-element or multiplexing array, each having a distinct Bragg wavelength. In sensing applications, peak tracing is commonly used for signal processing. This method is monitoring wavelength shift $\Delta\lambda$, which it is possible to estimate $\Delta\varepsilon$ or ΔT from Equation (1.2).

1.2.3 Fabry-Perot interferometer

A Fabry-Perot interferometer (FPI) is an optical cavity that consists of two reflecting mirrors. The mirrors are assumed to be flat and high reflecting, and the incident light is to be normal to the mirrors. When light enters the FPI with an intensity of I_0will be partially reflected and transmitted. Figure 1-7 shows how the light enters FPI and undergoes multiple internal reflections. The transmitted intensity (I_t) is a function of the reflectance (R), phase increment ($\Delta\phi$), and initial intensity (I_0):

$$F = \frac{4R}{(1-R)^2}, \tag{1.3}$$

$$I_t = \frac{I_0}{1 + Fsin^2\left(\frac{\Delta\phi}{2}\right)}. \tag{1.4}$$

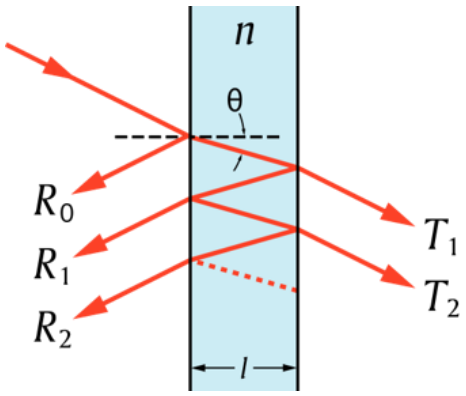

Figure 1-7: Schematic diagram of FPI. T_1 and T_2 are the transmitted light and R_0, R_1, and R_2 are the reflected light.

There have been many studies for applying FPI on the fiber-optic pressure sensor[56]–[62]. The working principle is inserting fiber into the housing structure, which consists of a membrane/ diaphragm. When the pressure was applied to the diaphragm, the cavity length changed as well. The pressure measurement is done by measuring the deflection of the diaphragm, which acted as a mirror of FPI.

1.2.4 Two-photon polymerization Fabry-Perot pressure sensor

3D printed miniature fiber-optic polymer-based FPI pressure sensor has received much attention. Instead of MEMS [63]–[70] or splicing fabrication [71]–[75], two-photon polymerization (2PP) provides a simple fabrication and relatively higher pressure sensitivity owing to its elastic property. H Wei et al. demonstrate 3D FPI on an optical fiber tip for a gas pressure sensor [76]–[81]. A 3D structure with a diaphragm is printed on a single-mode fiber tip, as shown in Figure 1-8. The light is partially reflected from the diaphragm, which acted as an FPI mirror. Wei characterized the pressure and temperature sensitivities of the sensors. As shown in Figure 1-9, the light spectrum of the sensor shifted as the load was applied. The static

calibration of pressure and temperature is done by the peak tracing method, as shown in Figure 1-9. The pressure and thermal response of the sensor can be expressed as:

$$\frac{d\lambda}{dT} = \lambda\left(\frac{1}{n}\frac{dn}{dT} + \frac{1}{L}\frac{dL}{dT}\right), \tag{1.5}$$

$$\frac{d\lambda}{dP} = \lambda\left(\frac{1}{n}\frac{dn}{dP} + \frac{1}{L}\frac{dL}{dP}\right). \tag{1.6}$$

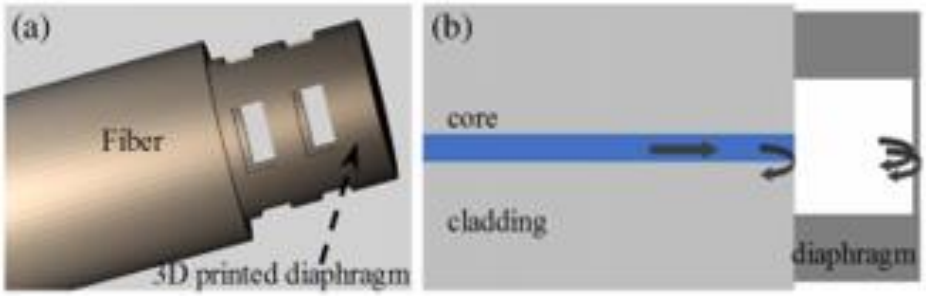

Figure 1-8: (a) Schematic diagram of the FPI pressure sensor. (b) side view of the sensor.

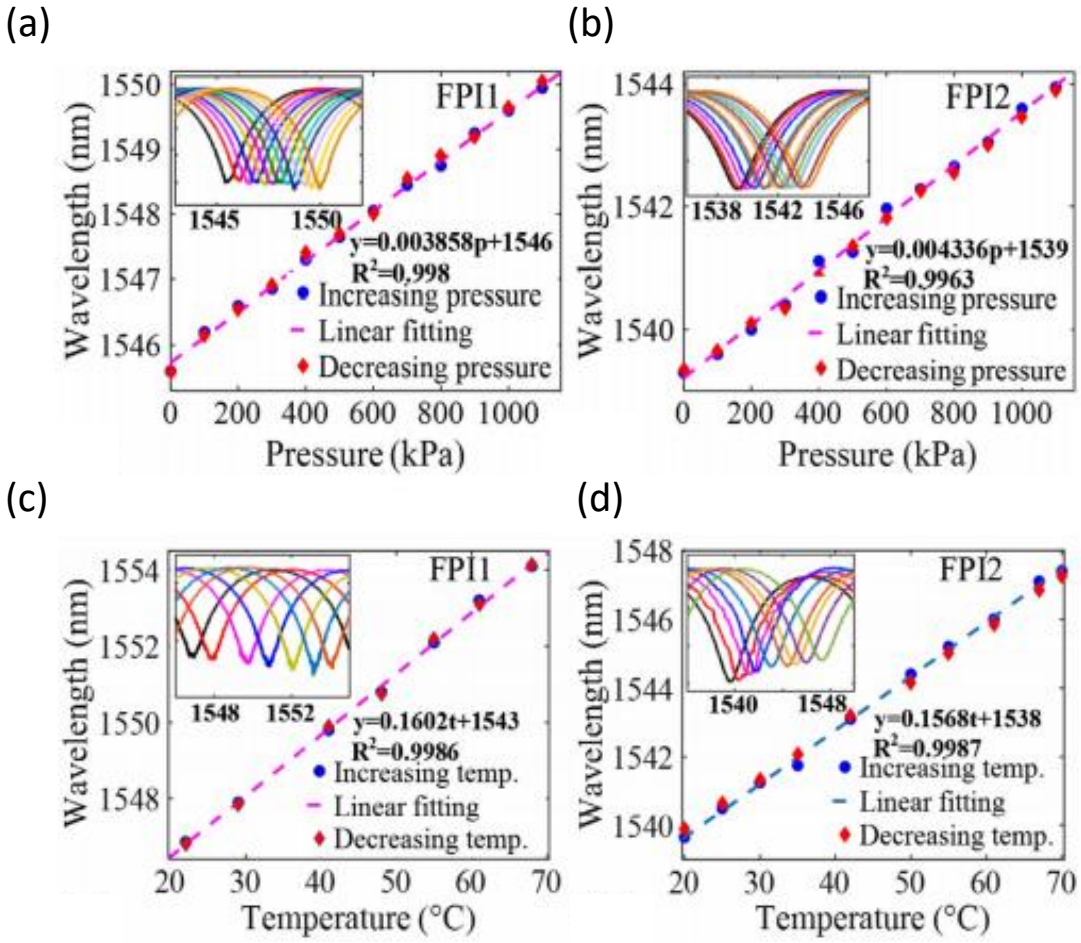

Figure 1-9: Wavelengths of the fabricated EFPI pressure sensors with a cavity length of (a) 140 µm and (b) 90 µm versus pressures. Wavelengths of the fabricated EFPI pressure sensors with a cavity length of (c) 140 µm and (d) 90 µm versus temperature.

A 3D-printed miniature optic-fiber polymer-based FPI sensor exhibits good pressure and temperature sensing. However, temperature sensitivity (0.16 nm/°C) is significantly larger than the pressure sensitivity (0.00385 nm/kPa). Without temperature compensation, the temperature effect on the cavity length change would cause an error in the pressure reading.

1.2.5 Temperature compensation for FPI pressure sensors

As previously mentioned in Section 1.2.4, polymer-based FPI sensors are often suffered temperature drift. Given the large temperature sensitivity of the polymer sensor[76], small temperature fluctuation can cause an error in pressure reading. Thus, compensating for the temperature drift is necessary for polymer-based FPI sensors. There are two different approaches to compensate for the temperature drift: additional structure and multi-parameter sensing.

The first temperature compensation method is to suppress the thermal expansion effect of the polymer by adding a ring-shaped structure to the diaphragm [82]. Hao *et al.* demonstrated that the pressure sensor with and without temperature compensation by simulation and experiment. The ring-shaped structure has a different thermal expansion coefficient (CTE) than the housing structure and is developed on the diaphragm surface, as Figure 1-10 shown. The diaphragm without compensation structure will bend upward when the temperature rises from T to T+ΔT due to the gas expansion. Similarly, the diaphragm will bend downward when the temperature falls from T to T-ΔT. However, the diaphragm with a compensation ring with a higher CTE material than the diaphragm will bend downward when the temperature rises because of the bimetal effect as shown in Figure 1-11. The zero-temperature sensitivity on the sensor can be achieved by changing the dimensions of the compensation structure, such as inner diameter and thickness.

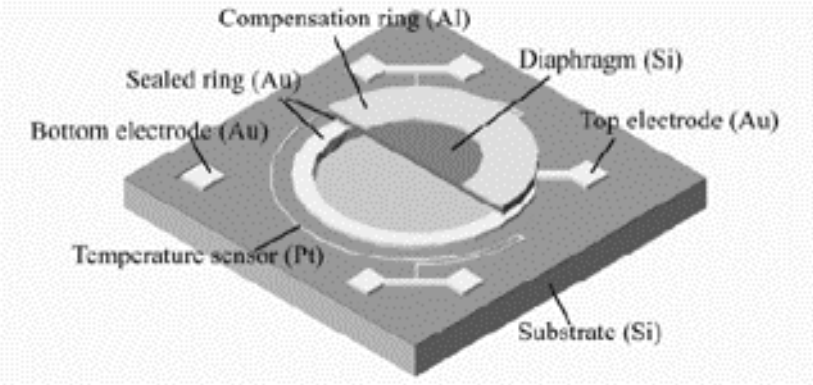

Figure 1-10: Schematic structure of the capacitive pressure sensor with a temperature compensation ring [23].

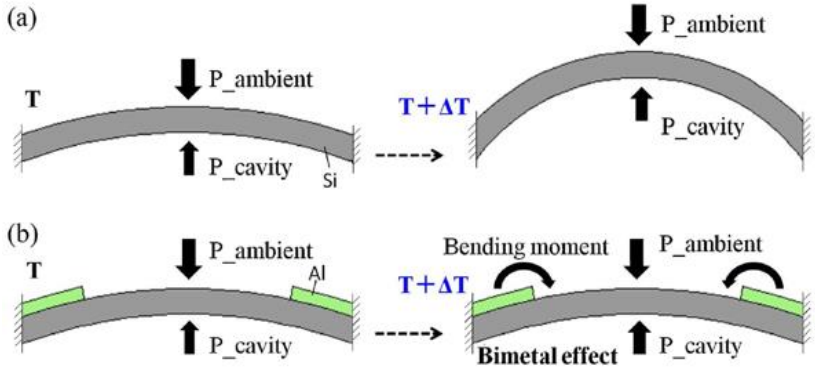

Figure 1-11: (a) The diaphragm without a compensation ring. (b) The diaphragm with a compensation ring [24].

The other temperature compensation method is multi-parameters sensing. The working principle is adding an extra sensing signal to the sensor, such as FBG. Bae et al. reported a miniature FP pressure sensor created by UV-molding with an FBG sensor. The polymer-based pressure sensor has built-in temperature measurement and compensation capability. Figure 1-12 shows polymer-based FP housing molded at the cleaved FBG fiber end. The spectrum of this sensor does not only consist of FPI but also consists of FBG as well. Figure 1-13 shows

the spectrum of the sensor at 25°C and 45°C. It is clear the spectrum of FPI and FBG shifted due to the temperature. The cavity length L of the sensor can be retrieved from the reflection spectrum, and can be written as:

$$L = \frac{\lambda_1 \lambda_2}{2n(\lambda_2 - \lambda_1)}, \tag{1.7}$$

where λ_1 and λ_2 are two adjacent peak wavelengths, and n is the refractive index of the FP cavity.

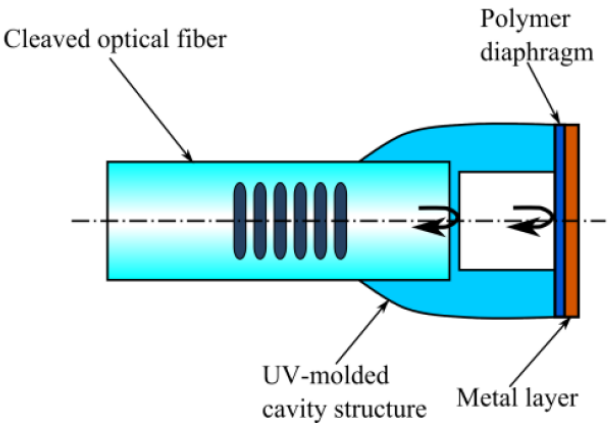

Figure 1-12: Schematic of UV-molded FP pressure sensor with temperature compensation[83].

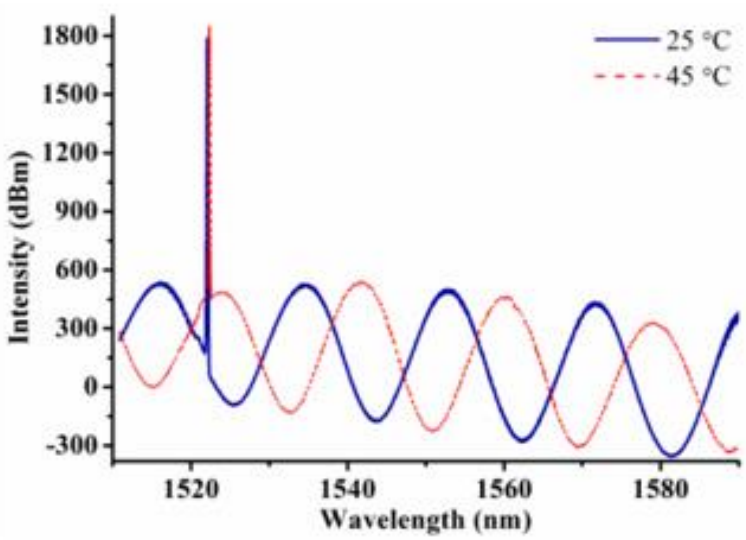

Figure 1-13: A representative interference spectrum was obtained by using the fabricated sensor with a built-in Bragg grating [25].

On the other hand, when the pressure was applied to the sensor, only the FP spectrum shifted. The FBG is insensitive to the pressure load due to the configuration of the design. Hence, the linear relationship between pressure and temperature can be expressed as the following:

$$\begin{bmatrix} \Delta\lambda_{FBG} \\ \Delta T \end{bmatrix} = \begin{bmatrix} 0 & 0.012\ \text{nm/k} \\ 10.6\ \text{nm/psi} & 15.8\ nm/k \end{bmatrix} \begin{bmatrix} \Delta P \\ \Delta T \end{bmatrix}. \quad (1.8)$$

Here, the pressure sensitivity of FBG is 0, the pressure sensitivity of FP is 10.6 nm/psi, the temperature sensitivity of FBG is 0.012 nm/K, and the temperature sensitivity of FP is 15.8 nm/K. By using the sensitivity matrix, both pressure and temperature values can be retrieved simultaneously.

1.3 Overview of the dissertation work

The overall goal of this dissertation is to develop a high-speed distributed fiber optic strain and pressure sensor system and use the system to perform experimental studies of the fluid-structure interaction of a flexible plate during slamming.

Research Thrust 1: Development of a high-speed spectral-domain optical system for interrogation of multiplexed fiber Bragg grating sensors and fiber optic Fabry-Perot sensors

This research thrust will focus on developing a high-speed, large dynamic range optical system for simultaneous interrogation of FBG sensors and Fabry-Perot sensors. A high-speed spectral-domain interrogation system is developed and characterized for a range of parameters such as sampling rate, scanning speed, resolution, and scanning range. Furthermore, experimental studies are carried out to investigate the performance of the high-speed spectral domain interrogation system that is used with Fabry-Perot pressure sensors and FBG strain sensors.

Research Thrust 2: Design and fabrication of miniature fiber optic pressure sensors with temperature compensation

In this research thrust, miniature FPI polymer-based pressure sensors are developed and fabricated by two-photon polymerization. These sensors are capable of monitoring high transient pressure load. Different temperature compensation methods are investigated to enhance the accuracy of the pressure measurement.

Research Thrust 3: Experimental investigation of the flexible plate slamming using a distributed fiber optic sensor system

In this research thrust, the high-speed spectral-domain interrogation system with FBG strain sensors and miniature FPI pressure sensors is employed to monitor the dynamic strain and pressure on the flexible plate during the slamming experiments. The dynamic strain and pressure responses that occurred on the plate during the slamming event are monitored.

The rest of the dissertation is organized as follows. The abovementioned research thrusts will be detailed in Chapters 2 to Chapter 4. In Chapter 5, a summary of the dissertation contributions and suggestions of future work will be provided.

2. High-speed spectral-domain interrogation system for multiplexed fiber optic sensors

2.1 Introduction

As discussed in the previous chapter, the slamming events induce large dynamic force and pressure on the hull, water spray generations, and rapid acceleration of the boat and the water. An optical sensing system has the capability of multiplexing and immunity to electromagnetic interference and is inherently waterproof. This sensing system is desirable for the study of slamming events. Recently, optical interrogators employing a tunable wavelength filter and a broadband light source have received much attention. This provides a compact and low-cost solution to realize high-speed, simultaneous interrogation of multiplexed FBG sensors or FP sensors. The performance of the interrogation system is determined by the tunable filter performance and the signal demodulation method.

In this chapter, an in-depth study of high-speed spectral-domain interrogation based on an FP tunable filter is presented. The optical interrogation system and its working principle will be discussed. Two types of signal sensor demodulation methods are investigated, which can be performed with or without reference to FBG sensors. The performance of the interrogation system will be characterized in experiments under different interrogation conditions such as sampling rate, scanning speed, and resolution.

Next, two proof-of-concept experiments are demonstrating the capability of the interrogator. One of the experiments is using a multiplexed FBG sensor to measure the modal shape of a cantilever, and the objective of this experiment is to show the capability of the multiplexing of FBG. The other proof-of-concept experiments are using the interrogator and FP sensor to

obtain an acoustic wave signal. The objective of this experiment is to demonstrate the ability of high-frequency sampling signals.

2.2 Overview of the high-speed interrogation system

2.2.1 High-speed interrogation system with FBG sensors

Figure 2-1 shows the proposed optical interrogation system with multiplexed FBG strain sensors. A broadband light source (EBS300006-03, Exalos) is coupled to a PZT FPTF (FFP-TF, Micron Optics). The finesse, free spectral range, and center wavelength of the tunable filter are 2000, 220 nm, and 1550 nm, respectively. For tuning purposes, a sinusoidal voltage is applied to the tunable filter by using a function generator. In this way, a narrow bandwidth light with a temporally oscillating center wavelength (i.e., scanning wavelength) is generated, as shown in Figure 2-2. The scanning range is adjusted by the amplitude and offset of the sinusoidal voltage so that it can cover all the Bragg wavelengths of the FBG strain sensors. Note that a sinusoidal waveform is used for achieving better scanning performance at high frequencies. The output light from the tunable filter is coupled to the multiplexed FBG strain sensors through a circulator (6015-3-FC, Thorlabs). The reflected light intensity from the sensors is measured by using a 10 MHz photodetector (PD) (2053-FC, Newport), and the PD output signal is received by using a data acquisition (DAQ) system (Picoscope, Pico Technology).

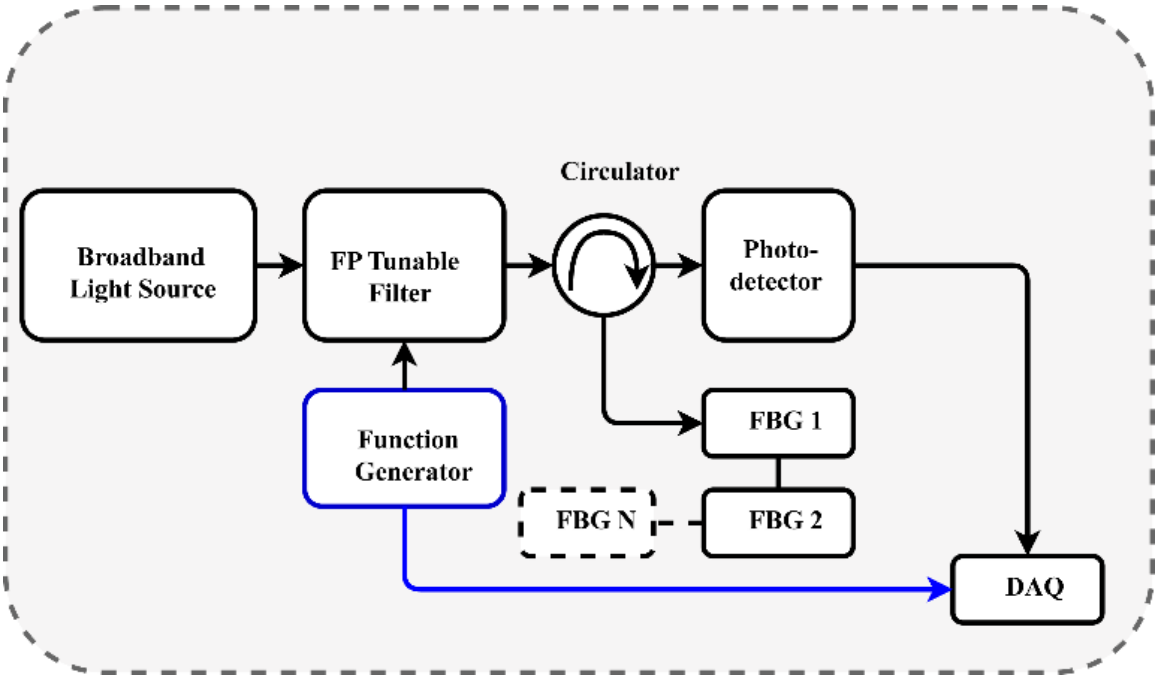

Figure 2-1: Schematic diagram of the proposed optical interrogation system with multiplexed FBG strain sensors.

2.2.2 High-speed interrogation system with FP sensors

The schematic diagram of the high-speed interrogation system with a fiber-optic FP interferometric sensor is shown in Figure 2-2. A broadband light source (EBS300006-03, Exalos) coupled with a piezoelectric FPTF (FFP-TF, Micron Optics) generates a narrow-linewidth scanning light Figure 2-3(a)]. A function generator provides the FTFP with a sinusoidal driving signal for tuning the wavelength of the scanning light. A scanning range is adjustable with the amplitude and offset of the driving signal. The scanning light is split by a 1×2 coupler and coupled into two subsystems, i.e., sensing and reference arms through a circulator (6015-3-FC, Thorlabs). The reflected light from the FP sensor in the sensing arm and the FBGs array in the reference arm is received by photodetectors (PD) (2053-FC,

Newport). The output signals of the photodetectors are recorded by using a data acquisition (DAQ) system (6404D, Pico Technology).

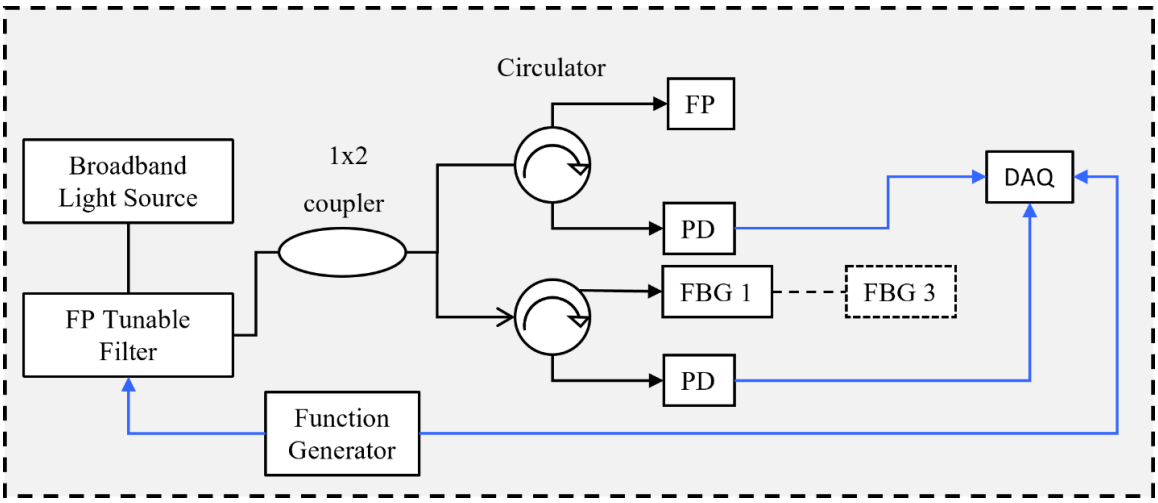

Figure 2-2: Schematic diagram of the high-speed interrogation system with a fiber-optic FP interferometric sensor.

2.2.3 Sensor signal demodulation

2.2.3.1 Acquisition of FBG sensor spectrum

The acquired sensor signal is demodulated to retrieve the Bragg wavelengths by using a peak tracing method, as illustrated in Figure 2-3(c) and Figure 2-3(d). Two signal demodulation methods are investigated, which can be performed either with (Figure 2-3(d)) or without a reference FBG (Figure 2-3(c)). For the signal demodulation method with a reference FBG, the reference FBG that is not subjected to any load is serially connected to the FBG sensor array. During each scan cycle (one period of the sinusoidal signal) of the FP tunable filter, the time-domain PD output signal has a series of peaks that correspond to the Bragg wavelengths of the reference FBG (marked in red) and the sensor FBGs (marked in black) [Figure 2-3(d)]. The time difference (Δt) between the reference peak and the sensor peak is used to retrieve the

Bragg wavelength of each FBG sensor based on the experimentally characterized Δt-to-wavelength conversion relation. Before performing strain measurements with the system, the conversion relation is obtained by measuring the Δts with respect to known Bragg wavelengths of the FBGs (see Figure 2-3(c)). On the other hand, for the signal demodulation method without a reference FBG, each Bragg wavelength is determined from the Δt between the two peaks of the PD output: one in the forward scanning period and the other in the backward scanning period [Figure 2-3(c)].

The major difference between the two signal demodulation methods is interrogation speed. The signal demodulation with a reference FBG allows the determination of Bragg wavelength twice during each scanning cycle (i.e., Δt1 during the forward scanning and Δt2 during the backward scanning), while in the method without reference, the Bragg wavelength is only obtained once. Therefore, for a given scanning frequency (f), the signal demodulation method with a reference FBG renders a two times faster interrogation speed (i.e., 2f) compared with that without reference. However, the reference FBG needs to be isolated from external loads. In the remainder of the paper, the sensor signal is demodulated with a reference FBG to leverage the fast interrogation speed.

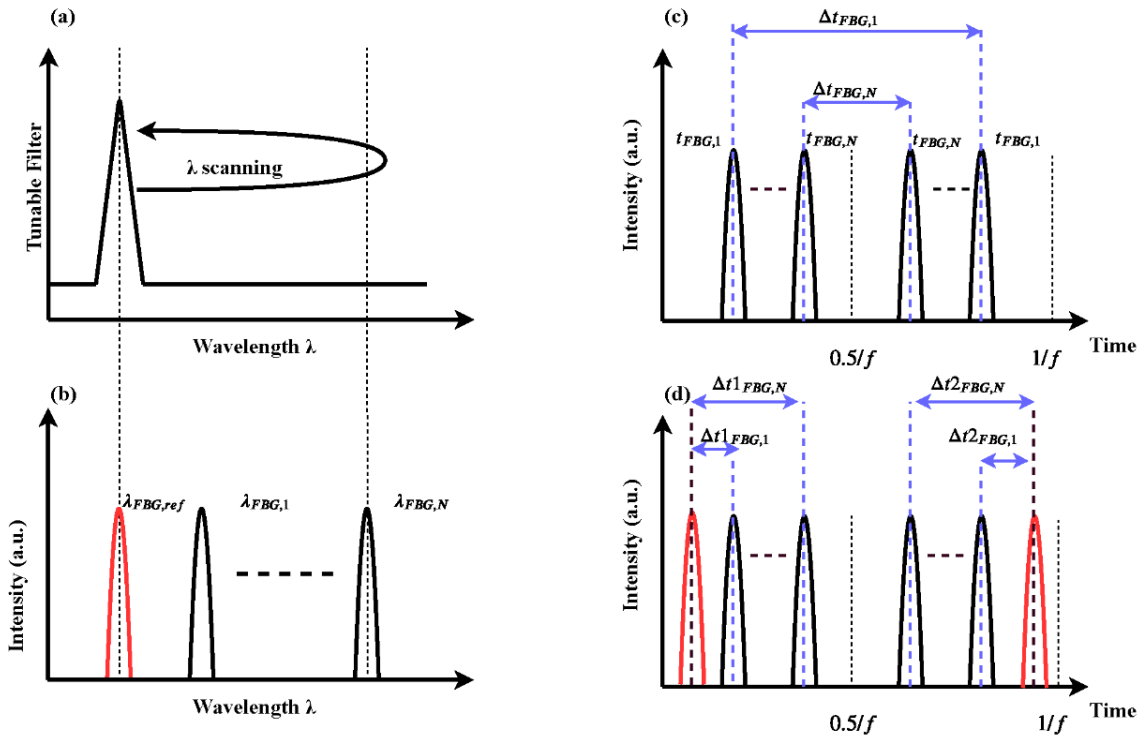

Figure 2-3: Schematic of the principle of simultaneous interrogation of multiplexed FBG strain sensors by using a peak tracing method. (a) The transmission spectrum of the tunable filter. (b) The reflection spectrum of the multiplexed FBG strain sensors with a reference FBG. Time-domain PD output signals during one scanning cycle for (c) the method without a reference FBG and (d) the method with a reference FBG. The Δts are used to determine the Bragg wavelengths. The forward scanning period is from 0 to 0.5/f, and the backward scanning period is from 0.5/f to 1/f.

2.2.3.2 Acquisition of FP sensor spectrum

The reflection spectrum of the FP sensor is obtained by converting the time-domain output signal of the PD in the sensing arm into a wavelength domain signal [see Figure 2-3(c)]. A time-to-wavelength relationship for the conversion is obtained from a time-domain output signal of the PD in the reference arm. Specifically, the time-domain signal from the reference arm has three peaks in each half cycle of the wavelength tuning [Figure 2-4(b)]. The peaks occur when the center wavelength of the scanning light (λ_{TF}) (Figure 2-4(a)) coincides with

the Bragg wavelengths of the FBG array. Therefore, each peak time is paired with the corresponding Bragg wavelength (e.g., t_1-λ_{FBG_1}, t_2-λ_{FBG_2}, and t_3-λ_{FBG_3}) (Figure 2-4(c)). From these three FBG pairs, a linear time-to-wavelength conversion relationship is obtained. Note that the FBG array should not be subjected to any load so that the Bragg wavelengths remain constant.

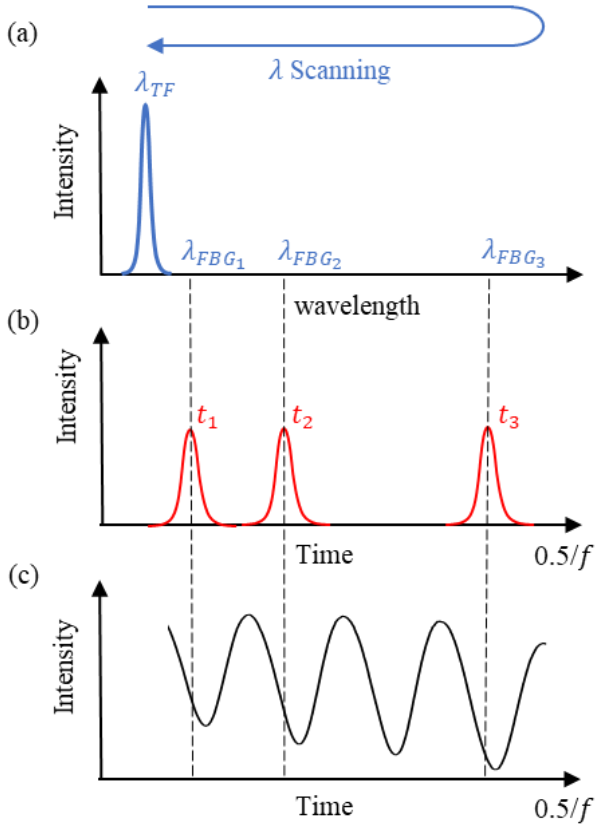

Figure 2-4: Schematics showing the principle of the high-speed interrogation of a fiber-optic FP interferometric sensor. (a) Transmission spectrum of the FPTF. (b) The time-domain output signal of the PD in the sensing arm. (c) The time-domain output signal of the PD in the reference arm. f is a tuning frequency of the FPTF.

Figure 2-5(a) shows representative time-domain output signals of the PDs in the sensing and reference arms along with a sinusoidal driving signal for the FPTF. Here, the amplitude and frequency of the driving signal were set to 1.4 V and 1 kHz, respectively. Three FBGs with Bragg wavelengths of 1539.63 nm, 1549.69 nm, and 1569.99 nm were used and the corresponding time-differences were measured to 0.00 µs, 56.3 µs, and 83.2 µs. The pairs of Δt_{FBG} and λ_{FBG} are in a good linear relationship with a coefficient of determination (R^2) of 0.99. Based on this experimentally characterized, linear time-to-wavelength conversion curve, the time-domain signal from the sensing group was converted into a sensor reflection spectrum, as shown in Figure 2-5(b).

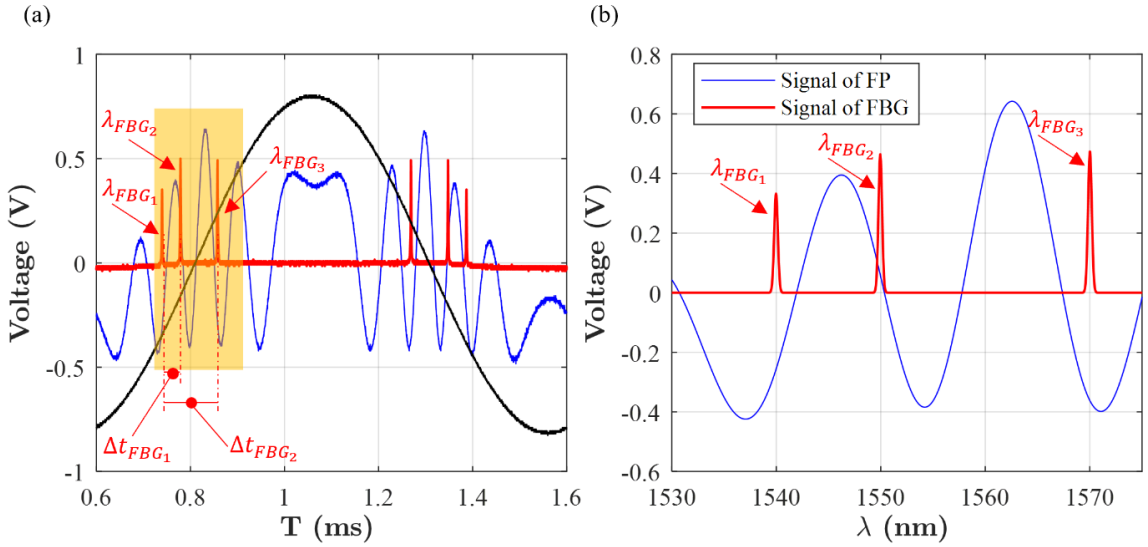

Figure 2-5: (a) Representative time-domain output signals of the PDs (shown in blue) in the sensing and reference groups (shown in red) along with a sinusoidal driving signal for the FPTF (shown in black). The amplitude and frequency of the driving signal were 1.4 V and 1 kHz, respectively. (b) Reflection spectra of the FP sensor and FBGs were obtained from the time-domain output signals which are labeled in the orange region from (a).

2.2.4 Performance of the interrogation system with FBG sensors

The performance of the interrogation system with FBG sensors was characterized in experiments under different interrogation conditions. First, the influence of the wavelength tuning speed (i.e., scanning frequency) on the interrogation range and resolution was investigated. Figure 2-6(a) shows the measured interrogation ranges at different scanning frequencies. Note that the amplitude of the sinusoidal voltage was fixed (1 V in this case). The interrogation range was found to decrease with increasing scanning frequencies until 35 kHz. After 35 kHz, it started increasing and reached a maximum of 98 nm at the resonant frequency of the PZT tunable filter (50 kHz). Note that there was a secondary peak at 128 kHz, which corresponded to the second harmonic of the PZT filter. The interrogation resolution, which was determined by the standard deviation of the Bragg wavelength monitored in the steady-state condition, was also affected by the scanning frequency. The interrogation resolution degraded with increasing scanning frequencies when the scanning frequency was below the resonant frequency of 50 kHz. For example, the interrogation resolutions at a scanning frequency of 10 kHz are approximately twice those at 1 kHz, as shown in Figure 2-6(b). At the resonant frequency of 50 kHz, the tunable filter was shown to have much better performance in the wavelength tuning, which rendered greatly enhanced interrogation resolution.

Furthermore, influences of the data sampling rate and the signal processing for the peak detection on the interrogation resolution were characterized. Figure 2-6(b) indicates that using a high sampling rate and performing Gaussian curve fitting of the raw data [84][85] could help improve the interrogation resolution. For example, at a scanning frequency of 50 kHz, an interrogation resolution of 5 pm was achieved by using a sample rate of 625 MS/sec and performing a Gaussian curve fitting to the acquired data in the signal processing for peak

detection. However, it should be noted that using a higher sampling rate and performing Gaussian curve fitting result in increased data size and data processing time.

In the following experimental studies, the sensor interrogation was carried out with a 1V sinusoidal waveform, a wavelength tuning speed of 50 kHz, a data sampling rate of 62.5 MS/sec, and a Gaussian curve fitting of the raw data was performed during the peak detection. The Δt-to-wavelength conversion relation for the signal demodulation can be obtained from either nonlinear or linear curve fitting of the measured Δt with respect to the known Bragg wavelengths of the FBGs. The nonlinear curve fitting method can provide the conversion relation over the entire scanning range. A large number of FBGs with different Bragg wavelengths distributed over the entire scanning range are required to obtain an accurate conversation relation. These interrogation conditions enable the sensor interrogation with a high speed of 100 kHz, a large range of 98 nm (capable of interrogating 97 FBG sensors of 1 nm spacing), and a high resolution of 10 pm (~ strain resolution of 8.3 με). On the other hand, the linear curve fitting method provides the conversion relation only for the linear region of the sinusoidal waveform and thus decreases the interrogation range. However, it helps simplify the post-processing. In the following experimental studies, the linear curve fitting method was used to obtain Δt-to-wavelength conversion relations.

Figure 2-6(c) shows the experimentally characterized Δt-to-wavelength conversion relations for the sensor signal demodulation. Eight FBGs with pre-calibrated Bragg wavelengths were used for the characterization, and the Δts corresponding to the Bragg wavelengths were measured for both forward and backward scanning processes. Note that the eight FBGs were not subjected to any load, and an FBG with a Bragg wavelength of 1570 nm was used as a reference. The conversion relations for both forward and backward scanning exhibited good

linearity with a wavelength scanning speed of 13.88 nm/μsec. The linear conversion relations were achieved by adjusting the offset of the sinusoidal voltage so that the peaks of the sensor output (e.g., the output signal of PD) were located in the linear region of the sinusoidal waveform, as shown in Figure 2-6(d). At the interrogation speed of 100 kHz, the linear spectral range was approximately 76 nm (= 5.5 μs). Note that the number of FBG sensors that can be interrogated is determined by the spectral range of the linear region and the wavelength spacing between the FBG sensors. Given the spectral range, more FBG sensors can be interrogated with smaller wavelength spacing, which, however, decreases the dynamic response range of the FBG sensors due to crosstalk interference. Therefore, suitable wavelength spacing should be chosen according to the dynamic response range and the number of sensors needed for the specific sensing application.

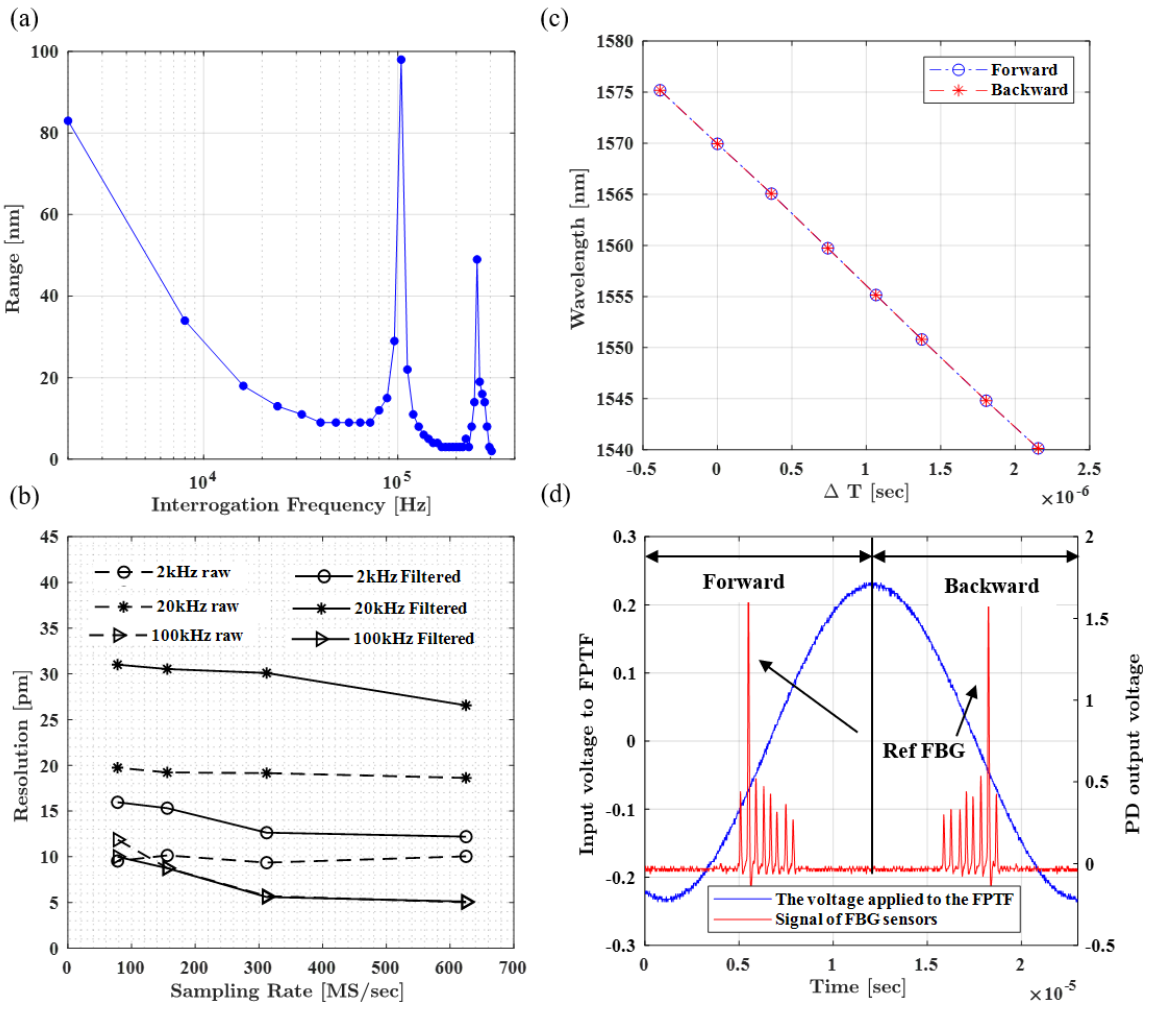

Figure 2-6: Experimental characterizations of the interrogation system. (a) Interrogation range as a function of scanning frequency. (b) Interrogation resolution as a function of data sampling rate at various scanning frequencies (1 kHz, 10 kHz, and 50 kHz). The markers in blue were obtained by performing a Gaussian curve fitting to the raw data, and the markers in red were obtained by using the peaks detected from the raw data. (c) Δt-to-wavelength conversion relations at a scanning frequency of 50 kHz and a data sampling rate of 62.5 MS/sec with a Gaussian curve fitting in the peak detection. (d) Time-domain signals of the applied voltage to the tunable filter and the obtained corresponding PD output voltage.

2.3 Characterization of a dynamic pressure sensor: pressure range and robustness to intensity noise

To demonstrate the performance of high-speed interrogation of an FP pressure sensor using the spectral domain interrogation system, a polymer-diaphragm-based fiber-tip FP pressure sensor was developed [Figure 2-7(b)]. The fiber end-face and the diaphragm serve as the two mirrors of the FP cavity. The cavity housing along with the diaphragm was fabricated by using 3D printing. The radius and thickness of the diaphragm were 75 μm and 2 μm, respectively. A 60-nm-thick aluminum layer was deposited on the diaphragm to enhance the mirror reflectivity. The 3D printed cavity housing was aligned and bonded to a cleaved single-mode optical fiber (SMF) using a UV curable adhesive to make a 60-μm-long FP cavity. The fabricated FP pressure sensor was characterized by the experimental setup shown in Figure 2-7(a). The FP sensor was characterized by a pressure chamber. The pressure inside the chamber was controlled by using a pressure regulator and a reference pressure sensor (PX429-SGV, OMEGA). Note that the pressure calibration range (0 – 70 kPa) was limited by that of the pressure chamber.

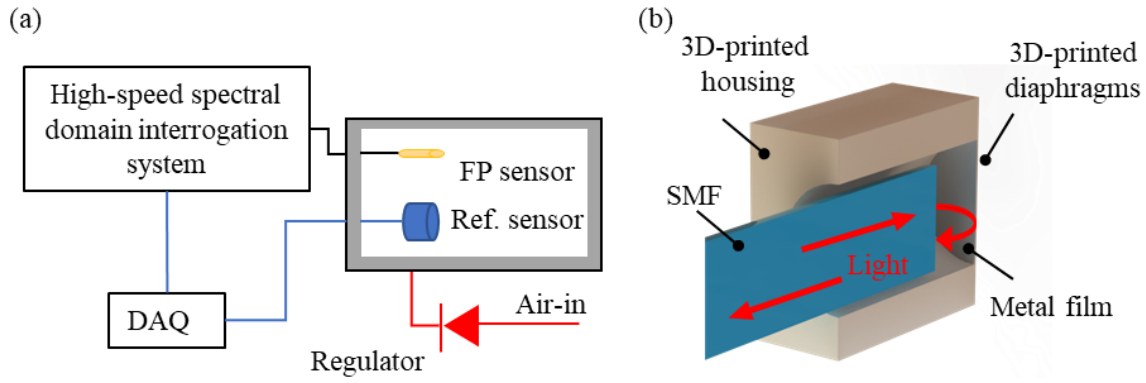

Figure 2-7: Schematics of (a) the experimental setup for pressure measurement and (b) the polymer-diaphragm-based fiber-optic FP pressure sensor.

Figure 2-8 shows the measured cavity lengths of the FP sensor at different chamber pressures. Note that the initial cavity length was obtained by applying a Fast Fourier Transform (FFT) to the acquired reflection spectrum of the FP sensor. Thereafter, the changes in the cavity length were obtained by tracing one of the peaks in the sensor reflection spectrum, i.e., the one peak tracing method [14]. The cavity length decreased linearly with increasing chamber pressure with a sensitivity of -0.012 μm/kPa (R^2 = 0.99). The dynamic range of the FP sensor was larger than ±70 kPa and the pressure resolution was 0.15 kPa. In addition, the same FP sensor was characterized by the intensity-based interrogation method. In this case, only the sensing arm of the setup in Figure 2-2 was used. The scanning light was tuned to locate at a quadrature operating point, which is at the steepest slope of the sinusoidal profile of the sensor reflection spectrum, by supplying a fixed DC voltage to the FPTF. Based on the results shown in Fig. 2-8, the dynamic range of pressure measurement using the intensity-based interrogation method was only ±17 kPa, which confirms that the high-speed spectral domain interrogation method has the advantage of a larger dynamic pressure range (more than ±70 kPa). Furthermore, it is challenging to deploy the intensity-based interrogation method outside of controlled environments because the sensor operating point often suffers from drifting due to environmental temperature perturbation. Moreover, any change in the interrogation system such as patch cord bending and light source replacement would change the output light intensity level. The sensor operation point drift and the change in the intensity level will induce sensitivity drift, which, if not recalibrated, would result in large measurement errors. Meanwhile, the high-speed spectral domain interrogation method, which allows for measuring the absolute cavity length, does not suffer from such sensitivity drift.

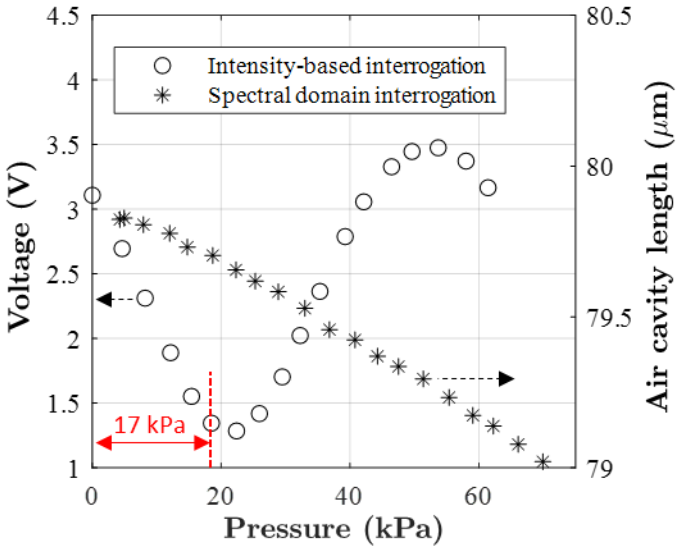

Figure 2-8: Response of the FP pressure sensor as a function of chamber pressure obtained with intensity-based interrogation method and high-speed, spectral-domain interrogation method. The intensity-based interrogation method shows a linear pressure response up to 17 kPa (dynamic range: ±17 kPa).

Figure 2-9 shows the transient responses of the FP sensor. Both high-speed, spectral-domain interrogation and intensity-based interrogation methods were used for the sensor interrogation. The profile of the transient responses from the spectral domain interrogation (at 2 kHz interrogation speed) [Figure 2-9(b)] agreed well with that of the intensity-based interrogation [Figure 2-9(a)]. In addition, the influence of light intensity noises on the sensing performance was examined. Light intensity noises were introduced to the interrogation system by applying impact loading to the optical fiber. The impact loading induced insertion losses in the optical fiber. The light intensity noises severely disrupted the sensor response from the intensity-based interrogation (see the pressure perturbations at ~30 sec in Fig. 2-9(a)). However, the sensor response from the high-speed spectral domain interrogation had negligible perturbations under the same level of noise (see at ~35 sec in Figure 2-9(b)). Such robustness to light intensity

noises attributes to the signal demodulation mechanism. For the high-speed spectral domain interrogation, the pressure measurement was based on the cavity length variation, which was obtained by using the profile of the sensor spectrum. As shown in Figure 2-9(c)-(e), the light intensity noises induce significant fluctuations in the overall intensity of the sensor spectrum, but these noises do not affect the spectral profile (Figure 2-9(b)). Therefore, the cavity length measurement using the spectral domain interrogation method is not susceptible to the noises.

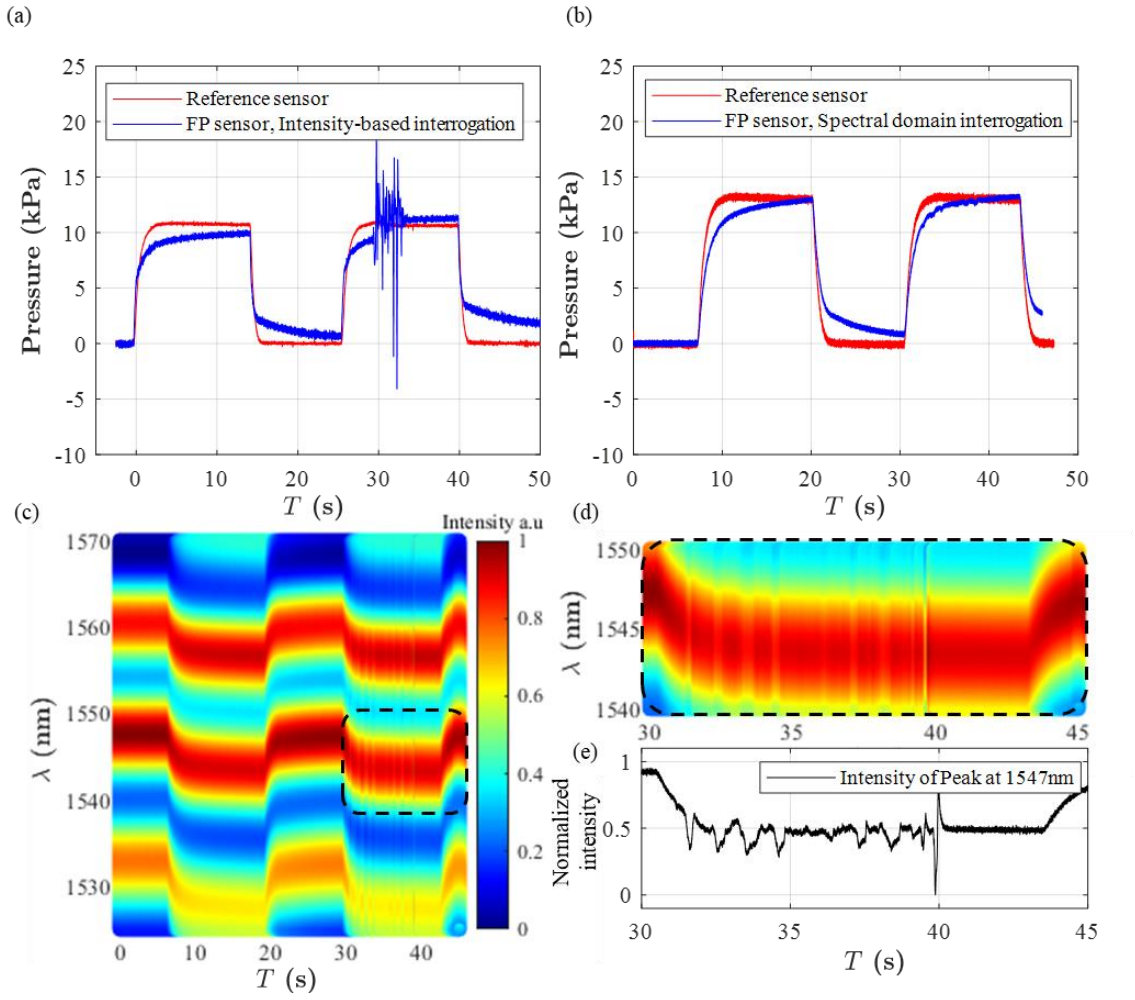

Figure 2-9: Transient responses of the FP pressure sensor obtained by using (a) the high-speed spectral domain interrogation and (b) intensity-based interrogation methods. Light intensity noises were introduced at ~30 sec in (a) and ~ 35 sec in (b). (c) The reflection spectrum of the FP pressure sensor as a function of time was obtained with the high-speed, spectral-domain interrogation method. (d) Zoom-in of the black dotted box in (c) showing the light intensity noise. (e) Time response of reflection intensity at 1547 nm showing the intensity noise introduced in (b).

2.4 Proof-of-concept study 1: vibration response of a cantilever plate under impact loading

2.4.1 Experimental arrangement

Four FBG strain sensors were mounted on the top surface of an aluminum cantilever plate (250 mm × 50 mm × 3 mm), as shown in Figure 2-10. The Bragg wavelengths of FBG 1, 2, 3, and 4 were 1565 nm, 1560 nm, 1555 nm, and 1545 nm, respectively. The FBG strain sensors were aligned with a 135° angle along the longitudinal direction of the cantilever plate to capture the plate bending-induced strains in both x and y directions. The aligned FBG strain sensors were bonded to the cantilever plate by using instant glue (Loctite 495) and Kapton tapes. An impact load was applied at the free end of the cantilever plate by using a piezoelectric impact hammer (PCB Piezotronics), which triggered the DAQ system to record the sensor signals.

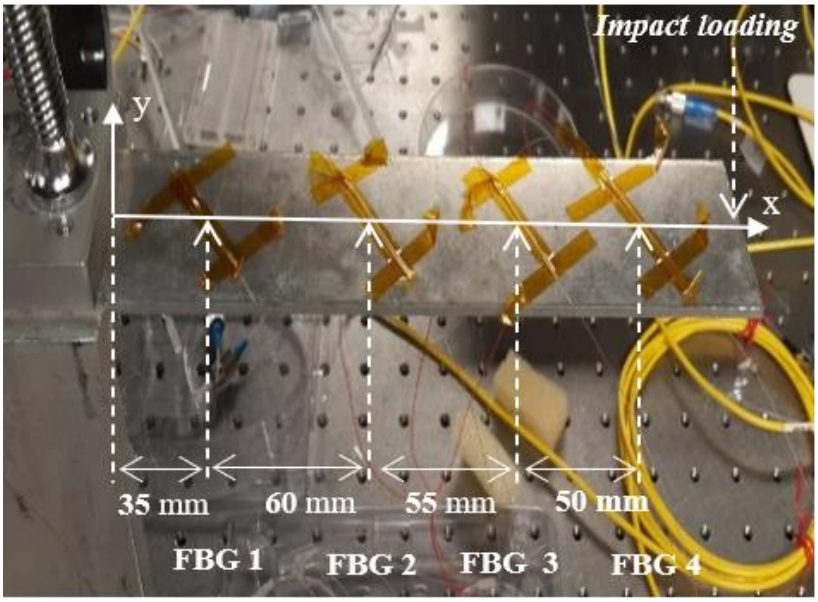

Figure 2-10: Image showing the four FBG strain sensors mounted on the top surface of the aluminum cantilever plate. An impact load was applied at the free end of the cantilever plate.

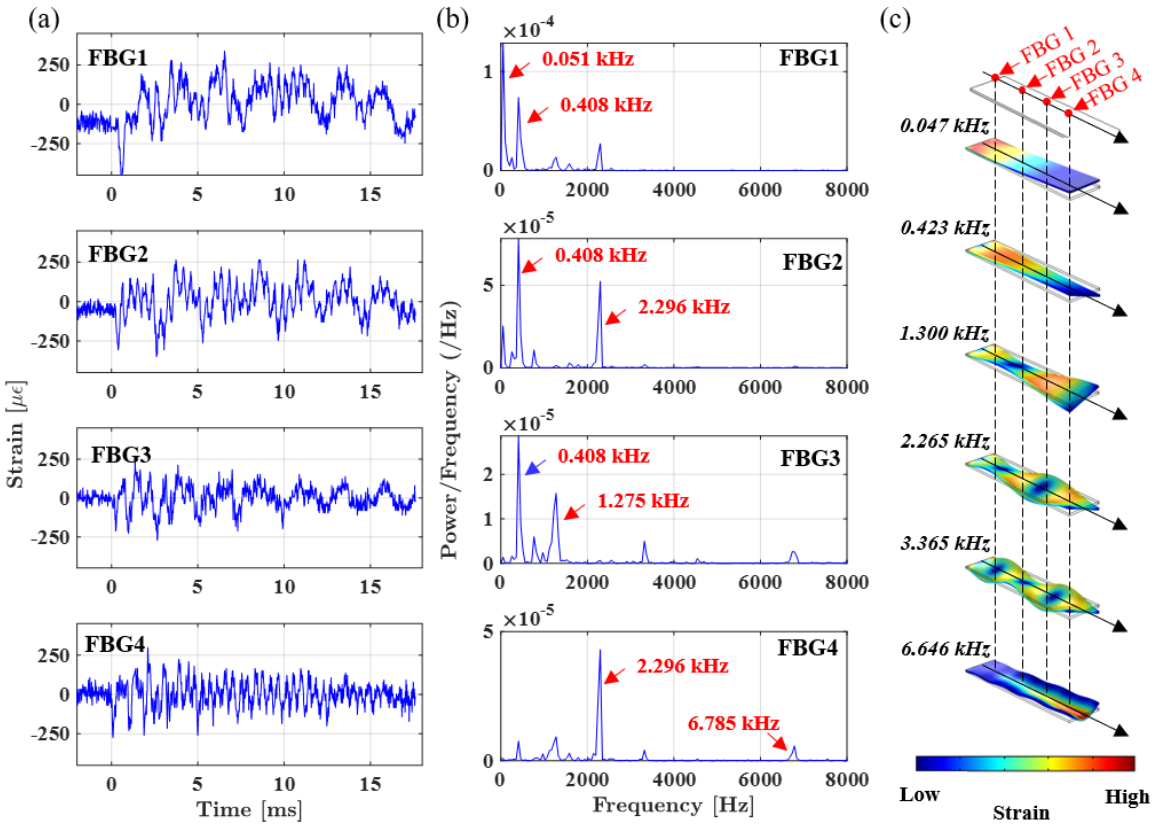

Figure 2-11: (a) Strain was measured by the four FBG strain sensors on the cantilever plate under impact loading. The nominal strain sensitivity of 1.2 pm/με is used for the conversion. (b) Frequency spectra of the measured strain signals. (c) Vibration mode shapes of the cantilever plate with corresponding first principle strain profiles were obtained in numerical simulations.

2.4.2 Result and discussion

Figure 2-11**Error! Reference source not found.**(a) shows the strain measured by the four FBG strain sensors on the cantilever plate under impact loading. The measured strain profiles revealed vibrational responses of the cantilever plate with multiple frequency components. To obtain the frequency responses of the strain, a fast Fourier transform was performed on the time-domain strain signals. As shown in Figure 2-12**Error! Reference source not found.**(b),

the obtained frequency spectra exhibited multiple harmonics with resonant frequencies up to 6.785 kHz. The measured resonant frequencies compared well with the natural frequencies of the cantilever plate obtained through a finite element analysis solver (COMSOL Multiphysics) Figure 2-11**Error! Reference source not found.**(c)]. Furthermore, at each resonant frequency, the peak amplitudes obtained from different FBG strain sensors agreed well with the location-dependent deformations due to the mode shapes. For example, at the resonant frequency of 0.051 kHz, the sensor close to the free end of the cantilever plate exhibited a lower peak amplitude. The profile of the peak amplitudes along the longitudinal direction of the cantilever plate agreed well with the simulated strain profile due to the mode shape at the natural frequency of 0.047 kHz. Therefore, the amplitude profile obtained from the FBG strain sensors can be used to analyze the vibrational mode shapes of the cantilever plate. More accurate analyses can be achieved by mounting a large number of FBG strain sensors on the cantilever plate in a two-dimensional array.

2.5 Proof-of-concept study 2: acoustic wave detection with Fabry-Perot pressure sensor

2.5.1 Experiential arrangement

A graphene-diaphragm-based fiber-tip FP acoustic sensor was developed for acoustic measurement [Figure 2-12(a)-(b)]. The design and fabrication process of the sensor is similar to those of the FP pressure sensor. However, graphene was used as a diaphragm material to enhance the sensitivity to acoustic waves. A graphene film was transferred to the 3D printed cavity housing by using the floating transfer method [34]. The reflection spectrum of the fabricated FP sensor is shown in Figure 2-12(c). Figure 2-12(d) shows the experimental setup for acoustic measurement. A loudspeaker (Pattersson) was used as a sound source and input signals were applied to the speaker by using a function generator (AFG3101, Tektronix). The

FP sensor was positioned so that the sensor diaphragm faced the loudspeaker. The interrogation of the FP sensor was carried out at a speed of 109 kHz. A reference microphone (4939-L-002, Brüel & Kjær) with a sensitivity of 100 mV/Pa was placed beside the FP sensor.

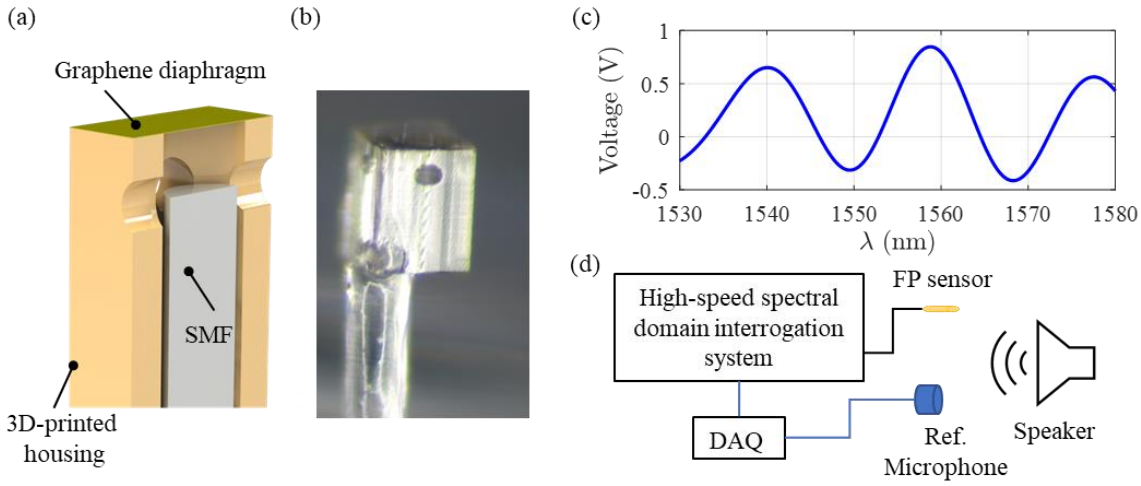

Figure 2-12(a) Schematic of the graphene-diaphragm-based fiber-optic FP acoustic sensor. (b) SEM image of the fabricated FP acoustic sensor. (c) The reflection spectrum of the FP acoustic sensor was obtained by using the high-speed spectral domain interrogation system. (d) Schematic of the experimental setup for acoustic measurement.

2.5.2 Result and discussion

Figure 2-13 shows the responses of the FP sensor and reference microphone to pure tones with frequencies of 12 kHz, 16 kHz, and 20 kHz and a Gaussian-modulated sinusoidal pulse with a center frequency of 16 kHz and a bandwidth of 1 kHz. The measured responses of the FP sensor agreed well with those of the reference microphone. These results demonstrated the capability of the high-speed spectral domain interrogation system for acoustic measurements up to 20 kHz.

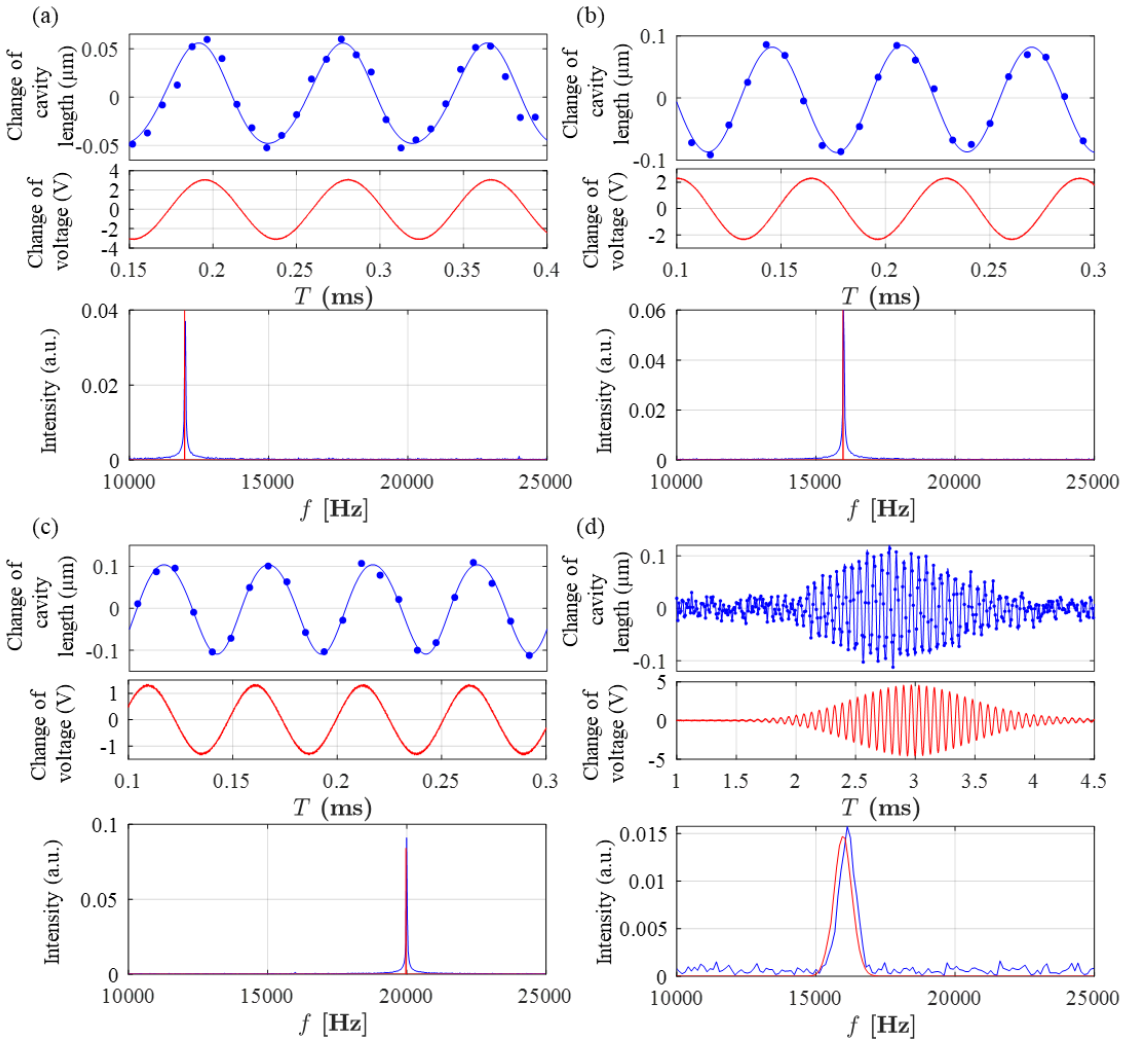

Figure 2-13 Responses of the FP acoustic sensor and reference microphone to different sound signals: pure tones with frequencies of (a) 12 kHz, (b) 16 kHz, and (c) 20 kHz, and (d) a Gaussian-modulated sinusoidal pulse at a center frequency of 16 kHz with a 1 kHz bandwidth. The top plots are the time-domain responses of the FP acoustic sensor (the blue markers are the experimental data and the blue line is the fitted curve). The middle plots are the time-domain responses of the reference microphone. The bottom plots are the frequency spectra of the FP sensor (blue curve) and the reference microphone (red curve).

2.6 Summary

A high-speed optical interrogation system based on piezoelectric FPTF for simultaneous interrogation of multiplexed FBG strain sensors and FP pressure sensors is presented. By operating the tunable filter at its resonant frequency and demodulating the sensor signal based on the peak tracing method, the optical interrogation system can achieve an interrogation speed of 100 kHz, an interrogation range of 98 nm, and an interrogation resolution of 5 pm. For proof-of-performance, the interrogation system was used to measure the vibrational responses of a cantilever plate under impact loading and strain responses up to 6.785 kHz were successfully detected. Furthermore, the performance of the proposed high-speed spectral domain interrogation scheme was investigated with two diaphragm-based fiber-tip FP sensors: a pressure sensor and an acoustic sensor. The acoustic measurement results demonstrated the ability of the high-speed spectral domain interrogation method for the measurement of dynamic parameters as high as 20 kHz.

3. Fabry-Perot pressure sensors with temperature compensation

3.1 Introduction

A Fabry-Perot (FP) pressure sensor is one of the widely used fiber optic pressure sensors that offer a multitude of potential applications owing to its advantages, such as miniature size, lightweight, and immunity to electromagnetic interference. A flexible, reflective diaphragm is usually used as the pressure sensing element. The diaphragm serves as one mirror of the FP cavity and the fiber end-face serves as another mirror. The sensing is based on the detection of deformation of the diaphragm, which induces optical path difference change of the FP interferometer. Many different types of miniature FP pressure sensors have been reported in the literature. Most of these FP sensors involve complicated fabrication processes. In this dissertation work, an additive manufacturing-based fabrication method; namely, the two-photon polymerization (2PP) method is explored for the development of miniature FP pressure sensors.

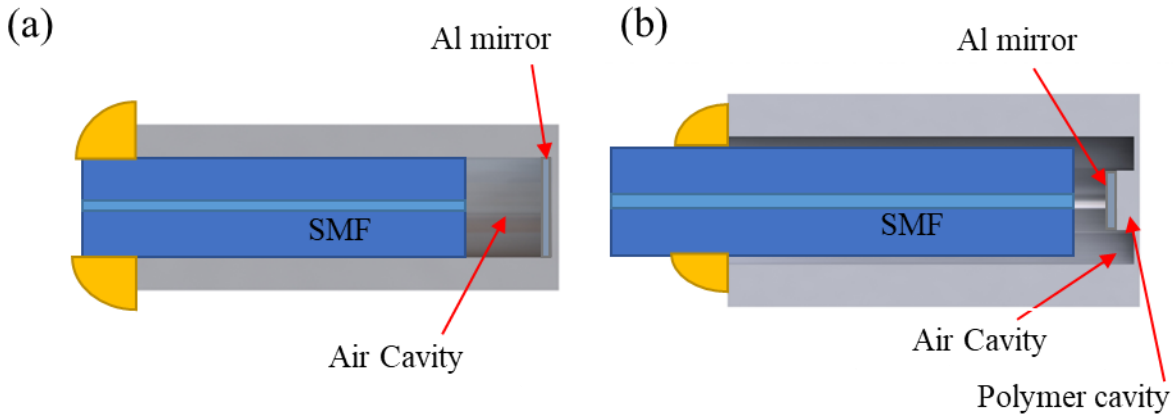

Figure 3-1: Schematic of the single and dual cavity pressure sensor.

In this chapter, two types of Fabry-Perot pressure sensors with temperature compensation sensors are presented: a single cavity FP sensor and a dual cavity FP sensor. Both of them have a sealed air cavity and the initial pressure in the cavity is the same as ambient pressure. When the ambient pressure changes, the diaphragm will bend downward or upward, depending on the pressure difference between ambient pressure and inner cavity pressure. The schematic of the two sensor designs is shown in Figure 3-1. The difference between a single cavity FP sensor and a dual cavity FP sensor is the diaphragm design. The single cavity sensor has a flat diaphragm, while the dual cavity sensor has a diaphragm with a mesa structure [86]. Both single and dual cavity sensors are made of polymer-based material. However, polymer-based pressure sensors are often suffered from temperature drift owing to their large thermal expansion. Without temperature compensation, the pressure measurement would have large errors due to the temperature drift. In order to resolve the temperature drift issue, temperature compensation methods are investigated.

3.2 Sensor design

The single cavity gas-sealed optical FP pressure sensor is illustrated in Figure 3-3. The sensor consists of a single-mode fiber (SMF) inserted in the polymer-based housing structure and the sensing diaphragm located at the end-face of the housing structure. The reflection spectrum of the FP sensor is determined by the optical path length (OPL) (OPL=2nCL, where n is the reflective index, and CL is the cavity length). In this design, the reflective index of air is 1, and cavity length can be adjusted to meet the requirement of the interrogation system. By using the relationship between two adjacent peaks of the sensor's reflection spectrum, the cavity length of the sensor can be calculated by the following equation:

$$CL = \frac{\lambda_1 \lambda_2}{2n(\lambda_2 - \lambda_1)}, \tag{3.1}$$

where $\lambda_1$and λ_2 are the adjacent peak wavelength as Figure 3-2 shown, and n is the reflective index of the cavity.

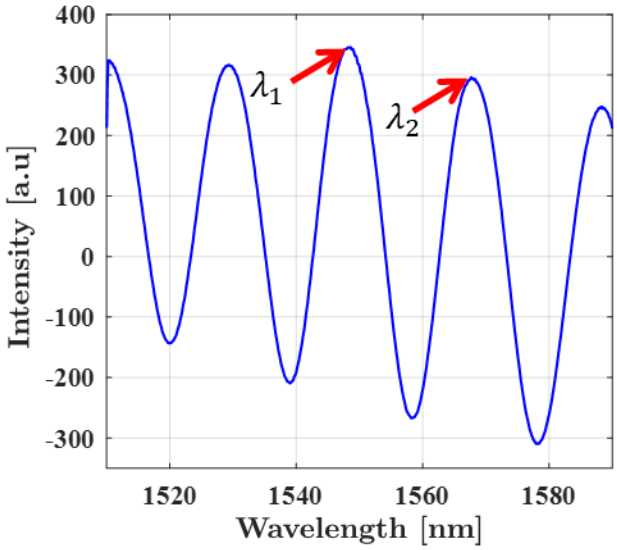

Figure 3-2 Reflection spectrum of FP sensor.

In this work, the spectral-domain interrogation method is proposed. If the 3dB bandwidth of the light source is 110 nm, and the cavity length of the FP is 60 μm. The reflection spectrum of the FP sensor should consist of 4 to 5 peak wavelengths. A stopper was included in the sensor structure to help the assembling process of the optical fiber with the sensing structure as Figure 3-3 shown. When the single-mode fiber (diameter = 125 μm) is inserted into the housing structure, the stopper will help ensure the fiber is positioned at the proper location. The inner radius of the stopper (r_i) is 80 μm, and the radius of the housing (r) is 150 μm. The length of the housing (L) is 250 μm; thus, the thickness of the housing is 50 μm. When designing the thickness of the diaphragm (t), several design factors need to be considered. As the thickness of the diaphragm is getting smaller, the pressure sensitivity is getting larger. It

can be explained by the large deflection model. The max deflection occurred at the center of the diaphragm, and it can be calculated as the following equation:

$$w_{max} = \frac{Pr_0^4}{64D}, \tag{3.2}$$

Where P is the pressure applied on the diaphragm, r_0 is the radius of the diaphragm and D is flexural rigidity, which is defined as:

$$D = \frac{Et^3}{12(1-v^2)}, \tag{3.3}$$

Where E is Young's modulus of the diaphragm, v is the Poisson's ratio, t is the thickness of the diaphragm. Therefore, a suitable thickness of the diaphragm should be chosen according to the dynamic response for the specific applications. Second, the OPL of the polymer cavity will interfere with the OPL of the air cavity when the thickness of the diaphragm is too large.

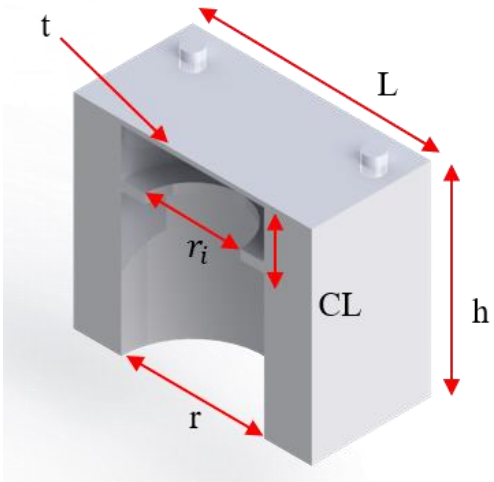

Figure 3-3: Schematic of the single cavity pressure sensor.

The dual cavity FP pressure sensor employs a different design for the diaphragm structure. As shown in Figure 3-1, a mesa structure is used. In this case, the sensor will have two FP cavities,

an air cavity between the bottom surface of the diaphragm and the fiber endface and a polymer cavity between the top and bottom surfaces of the diaphragm. The reflection spectrum of the dual cavity sensor is shown in Figure 3-4(b). Note that both the air cavity and the polymer cavity are sensitive to pressure and temperature. Using the temperature and pressure coefficient from both air and polymer cavities, a sensing matrix can be constructed as:

$$\begin{bmatrix} \Delta L_{air} \\ \Delta L_{polymer} \end{bmatrix} = \begin{bmatrix} S_{PA} & S_{TA} \\ S_{PP} & S_{TP} \end{bmatrix} \begin{bmatrix} \Delta P \\ \Delta T \end{bmatrix}, \tag{3.2}$$

where ΔL_{air} and $L_{polymer}$ are the changes in cavity length air and polymer, respectively, ΔP and ΔT are the changes in pressure and temperature. S_{PA} and S_{TA} are pressure and temperature sensitivity of the air cavity, and S_{PP} and S_{TP} are pressure and temperature sensitivity of polymer cavity.

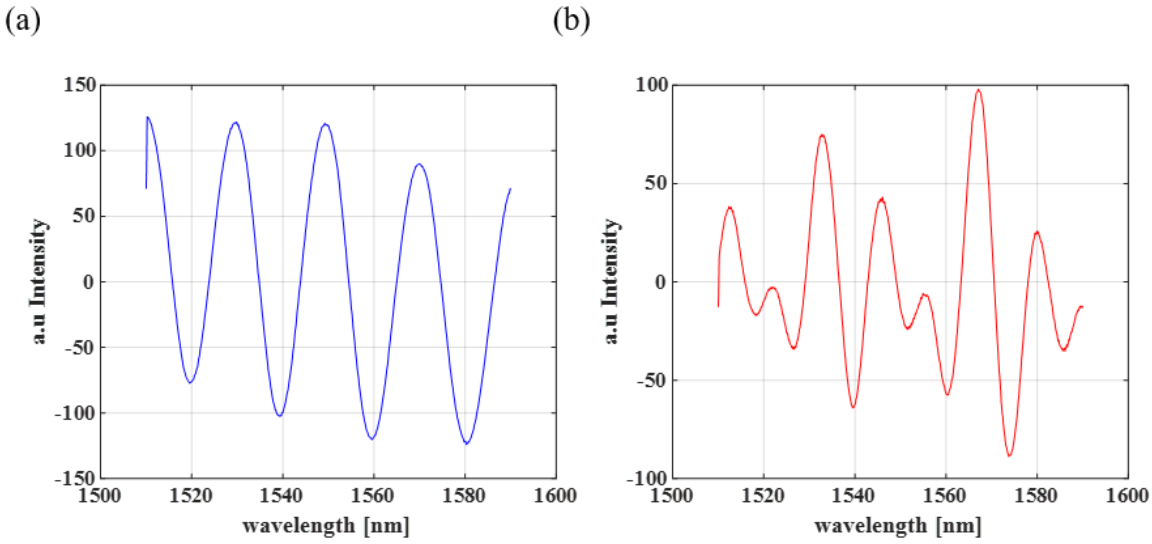

Figure 3-4: (a) Reflection spectrum of the single cavity FPI sensor. (b) The reflection spectrum of the dual cavity FPI sensor.

3.3 Sensor fabrication

The housings of single and dual cavity FP pressure sensors are fabricated by using a direct laser writing (DLW) fabrication process (nanoscale 3D printing) followed by thin metal layer deposition. Compared with previously reported FP sensors based on MEMS or splicing fabrication methods, the 2PP fabrication method provides a simple, high-resolution fabrication with a good device to device uniformity. The polymer used for the 3D microfabrication is IP-S polymer resin which is manufactured by the Nanoscribe (Photonic Professional GT Nanoscribe GmbH, Karlsruhe/Germany). After the housing of the sensor is fabricated, a thin layer of aluminum is deposited into the diaphragm by physical vapor deposition (PVD) to enhance reflectivity. Finally, the SMF is inserted into the housing structure and the housing is sealed with UV glue.

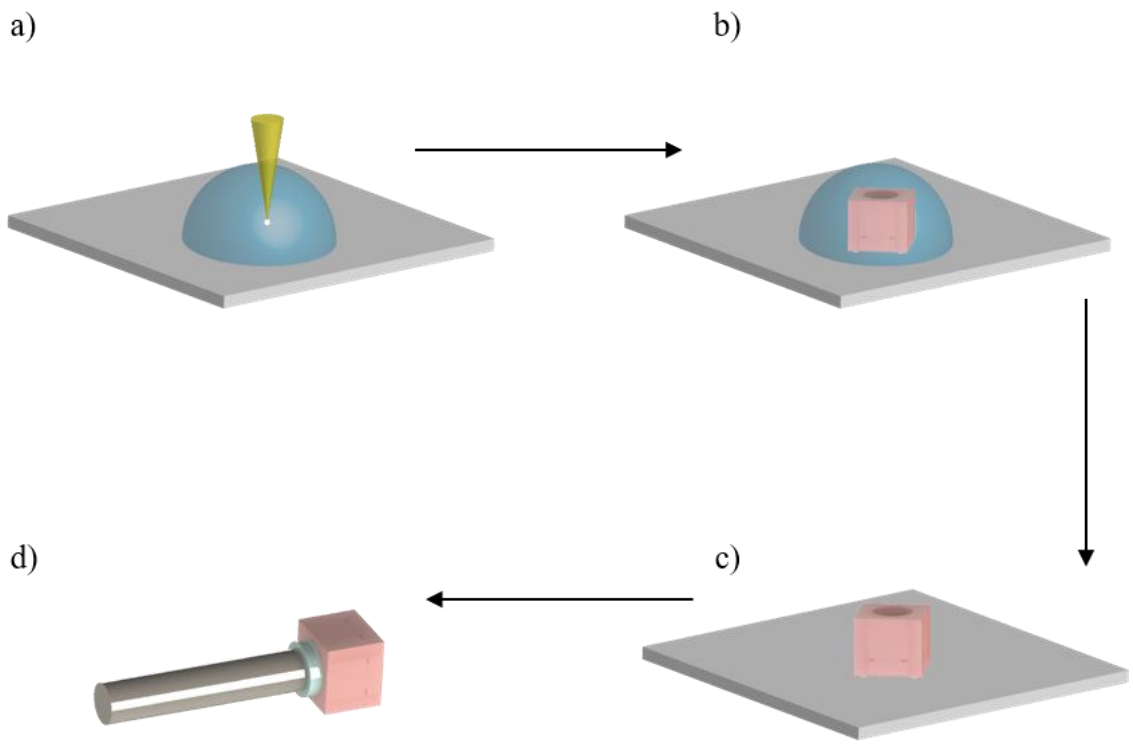

Figure 3-5: Fabrication procedure for the FP pressure sensor. (a) The polymer resin IP-S is dropped on the ITO-coated glass, and a laser is focused inside the resin to cure the IP-S. (b) The FP pressure sensor housing is printed using DLW. (c) The printed sensor is developed with PGMEA to remove the uncured polymer. Used IPA to remove the residue of PGMEA. Used PVD to deposit the Al layer inside the sensor to enhance reflectivity. (d) SMF is inserted inside the housing and sealed by UV glue.

The fabrication procedure of the FP sensor consists of 3 major steps: (i) DLW printing the housing, (ii) depositing an Al layer inside the housing, and (iii) assembling the sensor. First, the liquid-phase IP-S is prepared on the indium tin oxide (ITO) coated glass substrate, which is then placed into the DLW printer. Second, the STL file is converted into writing language as a gwl file by using the DeScribe software, where the printing conditions such as slicing,

hatching, and splitting can be changed to achieve an optimized printing setting. Next, the gwl file is loaded into Nanowrite software for printing. As shown in Figure 3-5(a), the DLW 3D printing is implemented by a focused Gaussian beam with a center wavelength of 780 nm and the beam is moved by using a piezo stage. After the solid-phase structure is printed, as shown in Figure 3-5(b), the glass substrate is removed from the DLW printer. The glass substrate is placed into the Propylene glycol methyl ether acetate (PGMEA) for 10 minutes and then isopropyl alcohol (IPA) for 2 minutes for development. The uncured IP-S is removed by the PGMEA, and the solid-phase structure is cleaned by the IPA, as shown in Figure 3-5(c). Next, a thin layer of aluminum (approximately 60nm) is deposited inside the housing by PVD. The metallic layer acts as a mirror to enhance the reflectivity inside the air cavity. Finally, the SMF is inserted into the housing by using the manual positioning stage (MBT501, Thorlabs). Once the fiber is inserted with a desired optical path length, the housing is sealed by UV glue.

3.4 Calibration

The calibration of the FP sensor for pressure and temperature measurement was performed in a sealed chamber with a reference pressure sensor (LL-080-35A, Kulite Semiconductor) and a temperature controller (CN77333, Omega Engineering Inc.), as shown in Figure 3-6. The internal chamber pressure is controlled by using either a manual or electrical pressure regulator with a range of 0 to 344 kPa. The internal chamber temperature is controlled by using the temperature regulator with a polyimide-insulated flexible thermocouple (CO1-K Omega Engineering Inc.) and a polyimide-insulated flexible heater (KH 103/10, Ocean Engineering Inc.). The heater and the thermocouple are placed next to the FP sensor to minimize error. The acquired optical sensor signal is retrieved by using an optical sensing interrogator (SM130, Micron optical), and the electrical reference sensor signal is obtained by using a DAQ card.

The commercial optical sensing interrogator is used to obtain the spectra, which are composed of a light source with a center wavelength of 1550 nm and a spectrum width of 80 nm, and a spectrometer.

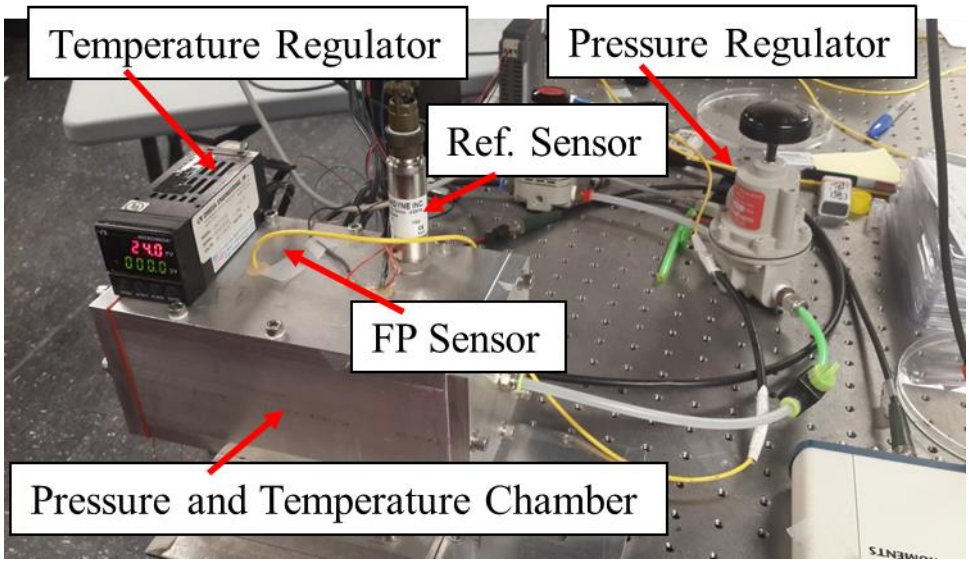

Figure 3-6: Experimental arrangement for pressure and temperature measurement.

The static pressure sensitivity of the FP sensor was calibrated against the reference sensor in the chamber. The cavity length of the FP sensor should remain constant while a fixed pressure load is applied in the chamber. If the FP cavity is not properly sealed, the cavity length will drift over time. Figure 3-7 shows the spectrum and calibration results of the single cavity FP with a 5μm thick diaphragm, while pressure and temperature load are applied. In this experiment, at a room temperature of 26.9 °C, the pressure in the chamber was increased from 0 to 4.87 psi. Figure 3-7(a) shows the reflection spectra of the single cavity FP sensor obtained for different applied pressure loads. The reflection spectra were shifted from right to left as the applied pressure increased. The membrane of the FP pressure sensor was compressed when pressure was applied. Figure 3-7(b) shows the optical path length decreased as the applied

pressure increased. The pressure calibration exhibits a good linearity (R^2=0.979) over the entire pressure range with pressure sensitivity (S_P) = -0.019 μm/psi. Next, the temperature sensitivity (S_T) was evaluated at atmospheric pressure. As the sensor was heated from 26.9°C to 31.5°C, the reflection spectra shifted from the left to the right, as shown in Figure 3-7(c). The temperature sensitivity of the FP sensor is 0.05 μm/°C. As previously discussed, polymer-based pressure sensors suffer from the drift due to temperature variations. Figure 3-8 shows the reflected spectrum of the dual cavity FP sensor and the corresponding temperature and pressure calibration results. The pressure sensitivities of air and polymer cavities are -0.061 μm/psi and -0.0026 μm/psi, respectively. The temperature sensitivities of air and polymer cavities are 0.054 μm/°C and 0.0037 μm/°C. Noted that the pressure and temperature sensitivities of the polymer are much lower than the sensitivities of air cavity. The temperature compensation of current dual cavities design might not be effective. To improve the sensitivities matrix, the structure of sensor needs to be redesigned. For example, the temperature sensitivity of the polymer cavity can be improved by enlarging the length of the mesa structure. The temperature sensitivity of the polymer is function of the length of the mesa structure. The temperature sensitivity of the polymer would increase as the length increase. As a result, the new design of the dual cavity should improve the temperature compensation.

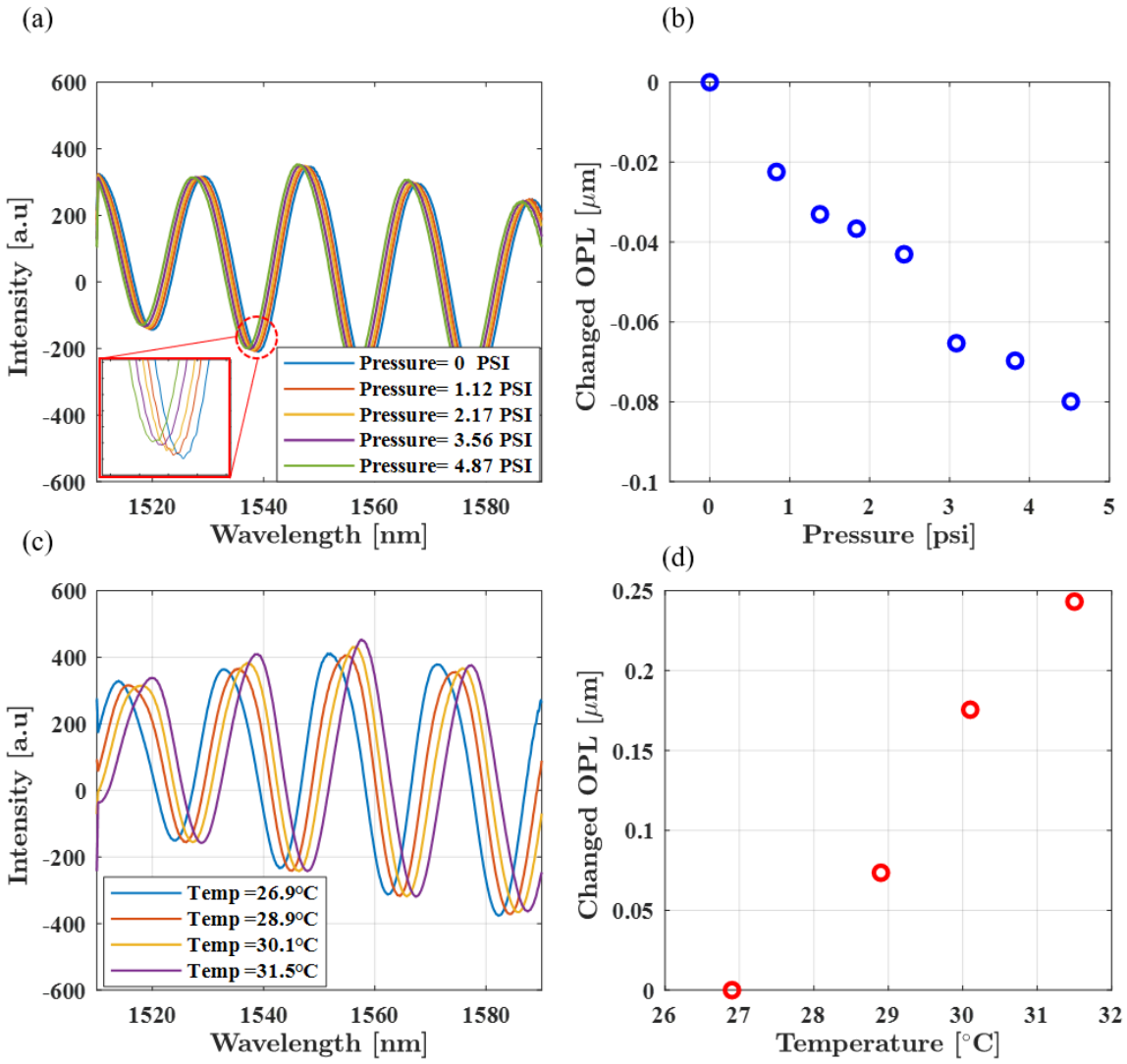

Figure 3-7: Reflection spectra of the FP sensor with different pressure (a) and temperature (c) load. The change of cavity length versus pressure (b) and temperature (d).

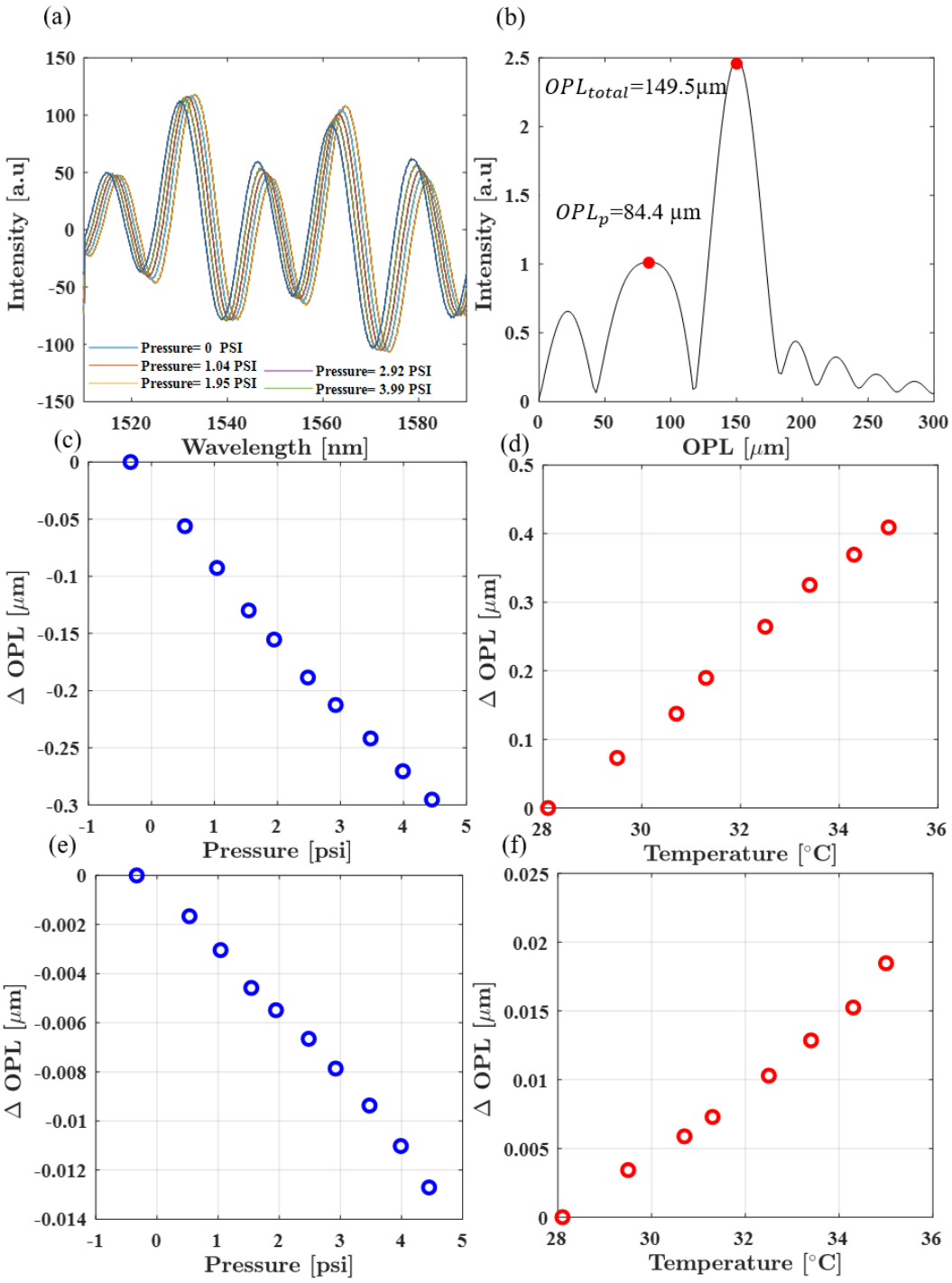

Figure 3-8: (a) The reflection spectra of the dual cavity FP sensor with different pressure loads. (b) The spatial FFT result from the wavenumber spectrum of the sensor. Pressure calibration curve of the air cavity (c) and polymer cavity (e). Temperature calibration curve of the air cavity (d) and polymer cavity (f).

3.5 Temperature compensation: dynamic response

As mentioned previously, due to the large CTE of the polymer material, the polymer-based FPI sensors suffer from temperature drift. Temperature compensation is needed to retrieve an accurate pressure value from a high-temperature fluctuation environment. To compensate for the temperature effect, the total optical path length of the FP sensor is decoupled to the pressure loading and thermal loading, $OPL_{total} = OPL_{pressure} + OPL_{temp}$. The $OPL_{pressure}$ and OPL_{temp} can be expressed as $OPL_{pressure} = \Delta P * S_P$ and $OPL_{temp} = \Delta T * S_T$, where S_p and S_T are the pressure and temperature sensitivities, respectively.

To demonstrate the temperature compensation, a single cavity FP pressure sensor with a higher pressure sensitivity was used in the following experiments. A thinner thickness of the diaphragm (t = 2 μm) was used and the cavity length remained at 80 μm, as shown in Figure 3-9(a). The pressure sensitivity (S_P = -0.816 μm/psi) is four time higher than the FP sensor with t = 5 μm (S_P = - 0.019μm/psi), but the temperature sensitivity remains the same (S_T = 0.05μm/°C) as shown in Figure 3-9(c)-(d).

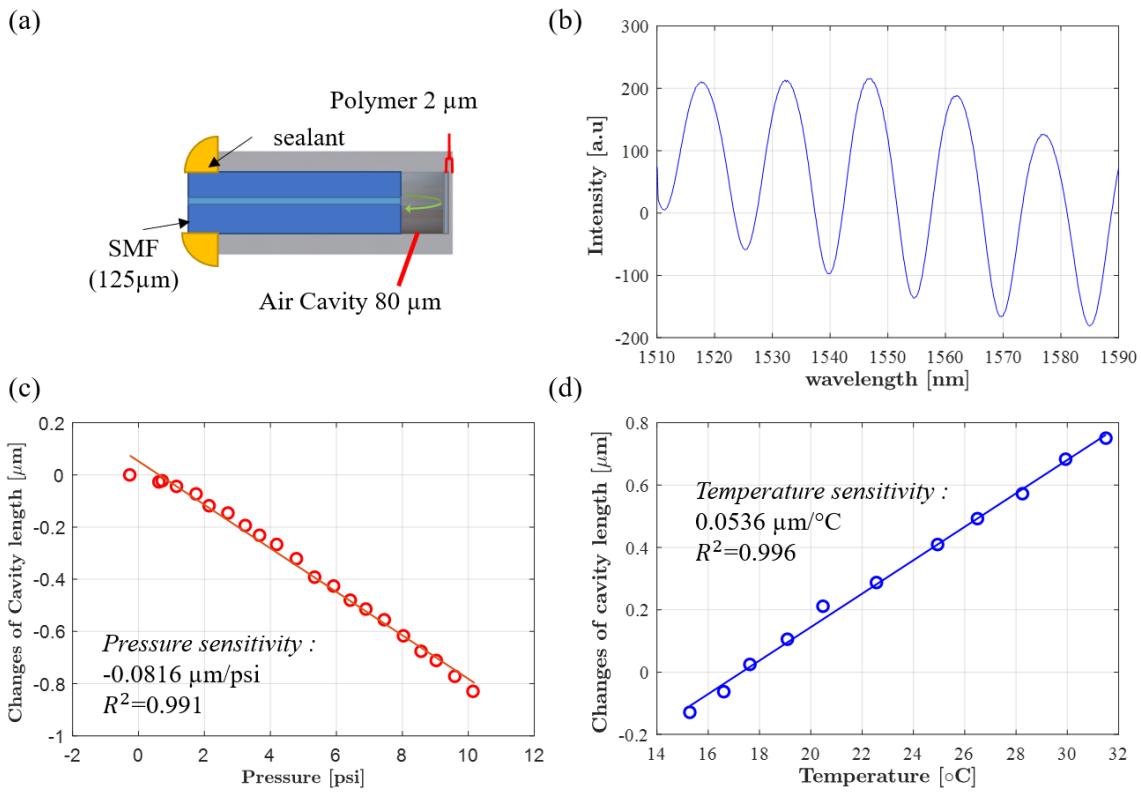

Figure 3-9: (a) Schematic of the single FP sensor. (b) The reflection spectra of the FP sensor. Pressure (c) and temperature (d) sensitivity of the FP sensor.

Next, the FP sensor was deployed in the enclosed pressure chamber with both reference pressure and temperature sensors in it. A step function of the pressure loading was applied to the pressure chamber, which is controlled by the electrical pressure regulator. The pressure was instantly increased from 0 psi to 4.5 psi and maintained at the pressure level for 15 seconds. Next, the pressure was decreased to 0 psi and the cycle was repeated.

Figure 3-10(a) shows that when the pressure increased, the temperature increased as well. The temperature change was caused by the temperature of the intake of cool air and the isometric process. Note that the poor resolution of the OPL_{temp} was caused by the thermal coupler which had a low sample rate and poor sensitivity inherently. Figure 3-10(b) shows the pressure

response of the FP sensor with and without temperature compensation. Without the temperature compensation, the pressure response was not able to reach the maximum pressure value (P = 4.5 psi) and failed to return to 0 psi. Pressure response with the temperature compensation shows good agreement with the reference sensor.

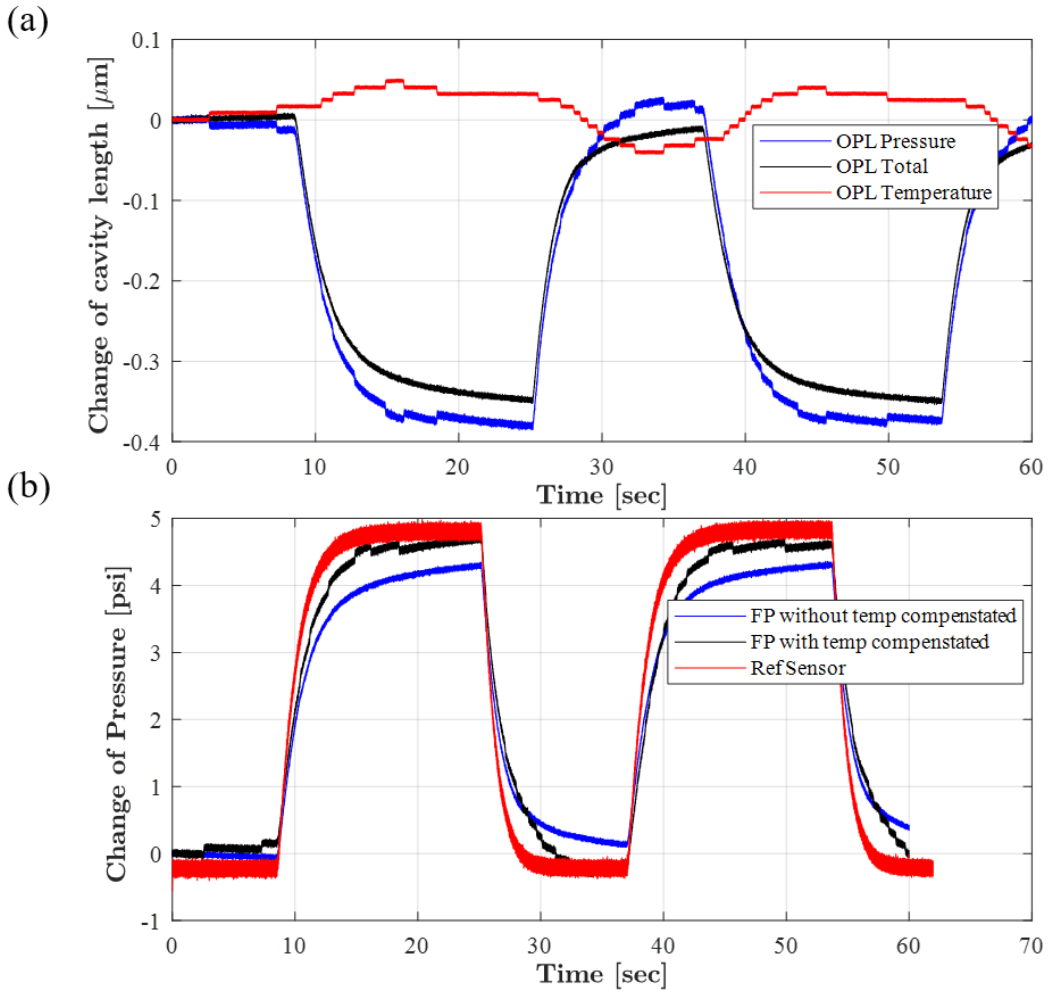

Figure 3-10: (a) The response of the optical path lengths to pressure loading. (b) Pressure response with and without temperature compensation.

3.6 Summary

Two types of miniature Fabry-Perot pressure sensors (a single cavity FP sensor and a dual cavity FP sensor) were designed. The sensors were fabricated by using the additive

manufacturer technique. Effective temperature compensation by using super-positioning the change of optical-path lengths induced by pressure and temperature is presented. By tracing the change of the optical path lengths of the dual cavity sensor, pressure and temperature sensitivities of the air and polymer cavities were obtained. By super-position the change of total optical-path lengths and the optical-path lengths induced by the temperature, the optical-path lengths change due to pressure was retrieved. The obtained pressure response after the temperature compensation exhibited a good agreement with that obtained from the reference sensor.

4. Experimental investigation of flat plate slamming with distributed fiber optic sensors

4.1 Introduction

Planing boats moving at high speeds in rough seas frequently slam into the water surface. The slamming event involves large dynamic forces and pressures on the hull, water spray generations, and rapid accelerations of the boat and the water. The investigation of the slamming phenomenon is challenging due to the large and violent motions of the hull and the water-free surface. There have been efforts for investigating the slamming phenomenon, and many of them have focused on the study of fundamental problems such as the impact of a flat or wedge plate on the water surface [87][88]. In such studies, monitoring the structural responses is important for a better understanding of the complex fluid-structure interaction during the slamming event.

Structural monitoring has often been performed by using a large array of electrical strain gauges. However, it is hard to apply electrical strain gauges to the slamming experiments because the electrical signals may be contaminated by the wet environment and the electromagnetic interference by a servo motor that controls the plate motion. Moreover, the electrical routing of a large array of strain gauges over long cables complicates the monitoring system. Optical sensing with fiber Bragg grating (FBG) strain sensors offers an attractive alternative to electrical sensing owing to their advantages of being waterproof, robustness to corrosive environments, immunity to electromagnetic interference, and multiplexing capability. The conventional electrical pressure sensor also suffers the same problems as electrical strain gauges. Furthermore, the bulky electrical pressure sensor would be damaged due to the large deformation of the plate during the slamming. Miniature optical pressure sensors have become

an attractive choice for pressure monitoring owing to its small size and immunity to electromagnetic interference.

4.2 Experimental facilities

The experiments were performed in the hydrodynamic laboratory at the University of Maryland. The slamming experiments were carried out in a towing tank system, which is 13.4 m long by 2.44 m wide by 1.35 m tall, as shown in Figure 4-1 and Figure 4-2. Details of the towing tank system have been discussed in [87]. An aluminum plate was mounted on a carriage with a pitch angle α and a roll angle β. The carriage was driven by an electric servo motor so that the plate could move simultaneously at different impact speeds in horizontal (*U)* and vertical (*W)* directions along a fixed trajectory, and the total speed $V_{total} = \sqrt{U^2 + W^2}$.

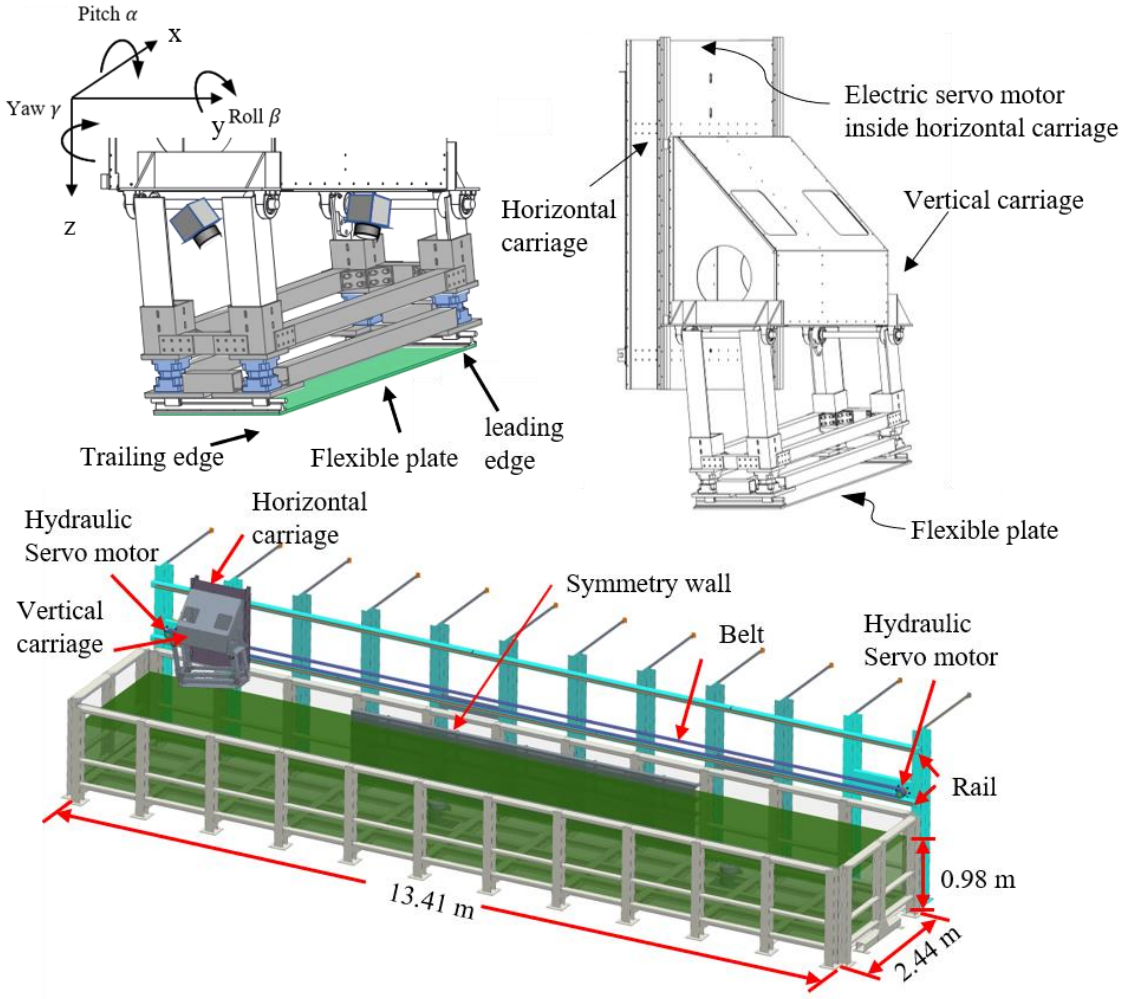

Figure 4-1: Schematic of the towing tank system.

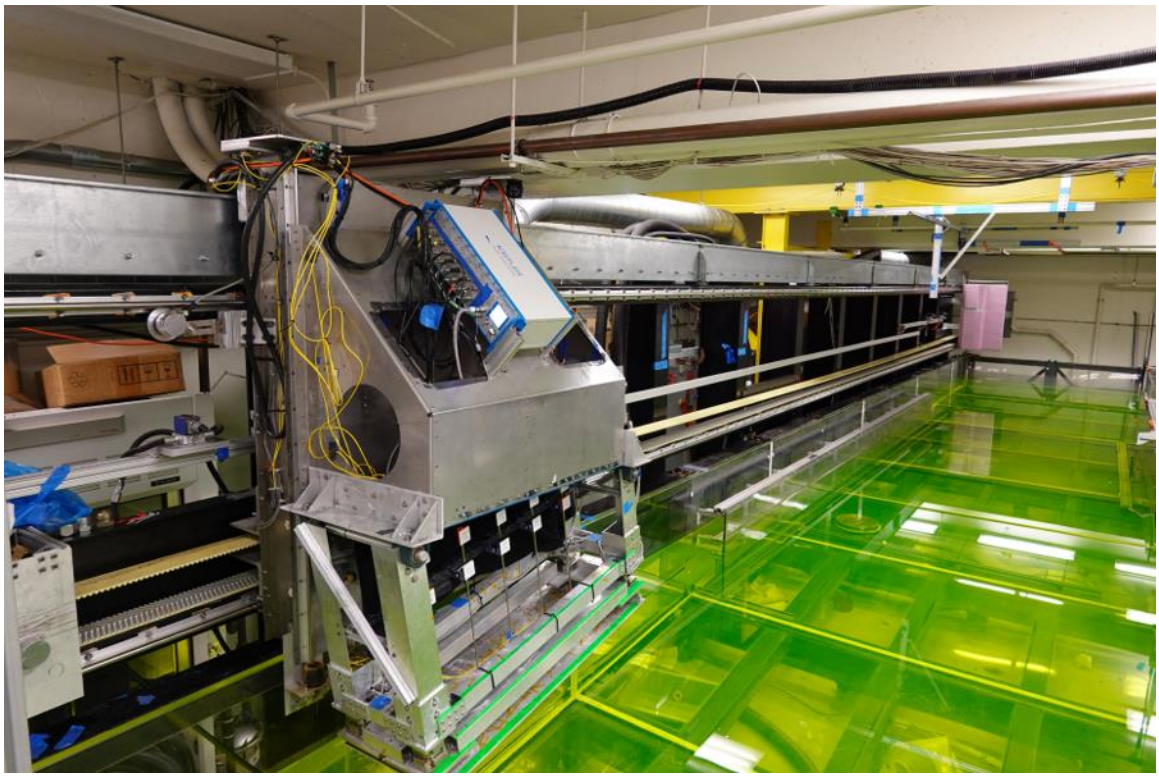

Figure 4-2: A photograph of the experiment facility.

4.3 The experiment of strain sensing

4.3.1 Experimental conditions

Two different sets of experimental conditions were used for investigating the effect of the thickness of the impact plates and the pitch angles. In 2020, two solid aluminum plates with thicknesses h= 6.35 and h = 7.95 mm and the same plan dimensions (1.08 x 0.406 m) were used with test conditions in Figure 4-3. Noted that only one pitch angle ($\alpha = 10°$) was used. 15 FBG strain sensors were mounted to the top of the plate to measure the strain response during the slamming impact. One FP pressure sensor was used later for vertical slamming impact with thickness h = 7.95mm. In 2021, a different set of slamming conditions was used. Only one solid aluminum plate with thickness h = 6.35 mm was used. The objective of this set slamming condition is to investigate the effect of the pitch angles α = 12.5°, 10°, and 7.5°.

Two solid aluminum plates with thicknesses h = 6.35 and h = 7.95 mm and the same plan dimensions (1.08 x 0.406 m) were mounted with a pin support at the leading and trailing edge with a pitch angle α=10° on the carriage. Figure 4-3 shows the matrix of carriage velocity components of the ratio of U/W (4.5, 5.5, 6.3, and 8.3) and normal impact velocity $V_n = U\,sin\,\alpha + W cos\,\alpha$. For all the testing conditions, the carriage started at the same initial position, and the horizontal and vertical carriages then accelerated to a constant speed U and W. The carriages maintained their speeds until the leading edge reached the still water level (SWL), and then slowed down with a constant deacceleration.

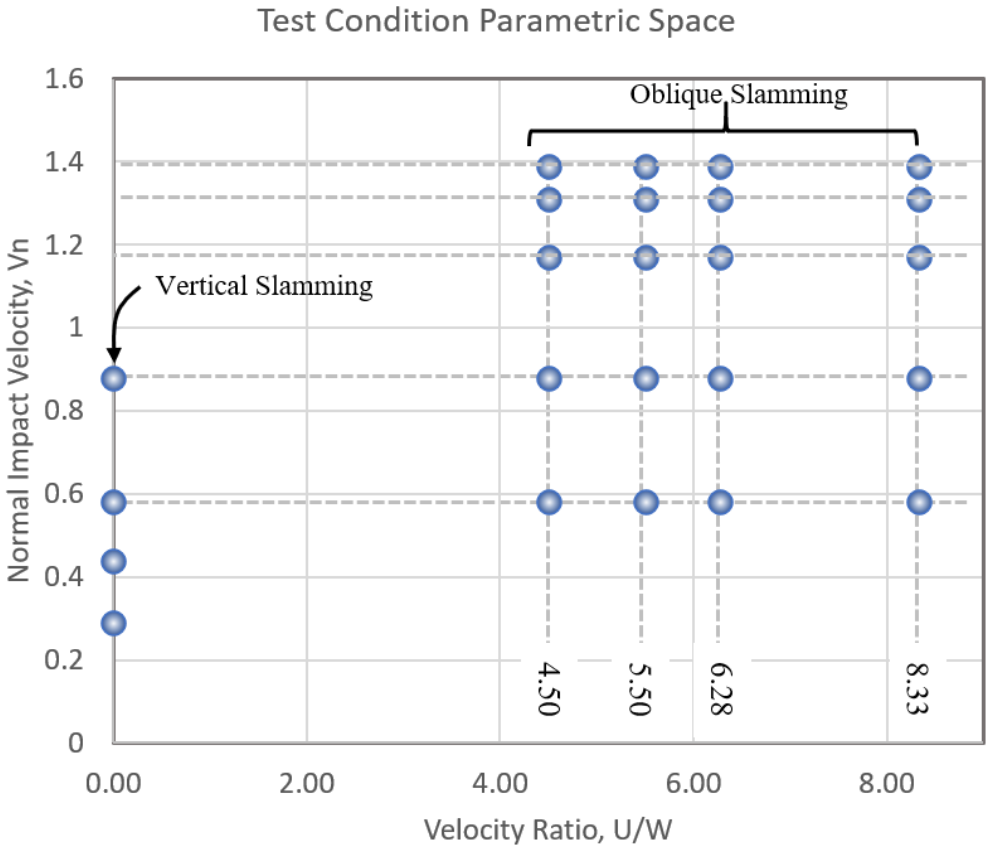

Figure 4-3: Test conditions for slamming experiments.

α						
7.5°	*U (m/s)*	3.969	5.570	5.754	6.727	7.375
	W (m/s)	0.875	0.665	0.64	0.512	0.427
	V_n (m/s)	1.386	1.386	1.386	1.386	1.386
	U/W	4.534	8.38	8.984	13.128	17.273
10°	*U (m/s)*	3.149	3.546	4.116	4.760	
	W (m/s)	0.852	0.782	0.682	0.568	
	V_n (m/s)	1.386	1.386	1.386	1.386	
	U/W	3.969	4.534	6.038	8.38	
12.5°	*U (m/s)*	1.613	2.571	3.21	4.163	
	W (m/s)	1.062	0.85	0.708	0.497	
	V_n (m/s)	1.386	1.386	1.386	1.386	
	U/W	1.519	3.026	4.534	8.38	

Table 1:Parameters of the 2nd set of slamming conditions.

The 2nd set of slamming conditions was focusing on varying the pitch angles and a higher U/W ratio while keeping the V_n constant. Note that only thickness of the ¼ inch plate was used for this set of slamming conditions. Table 1 shows the 2nd set test condition experiment.

4.3.2 Experimental arrangement of strain sensors

Here, the multiplexed FBG strain sensor interrogation system was used to monitor the dynamic strain responses of a flexible plate during its oblique impact with a quiescent water surface. 15 FBG strain sensors were mounted on the top of the plate, as shown in Figure 4-4. The sizes of the aluminum plates were 1080 mm long x 406 mm wide × 7.9 mm height and 1080 mm long x 406 mm wide × 6.35 mm height. The sensors were divided into three groups to avoid overlapping the Bragg wavelength. The Bragg wavelengths of these FBG sensors were 1555 nm, 1560 nm, 1565 nm, 1570 nm, and 1575 nm. Note that the wavelength spacing of 5 nm was chosen to avoid the crosstalk between the FBG sensors under a large strain. Given the FBG's

nominal strain sensitivity of 1.2 pm/με, the FBG sensors can measure tensile and compressive strains up to 2083 με without crosstalk interference. The FBG strain sensors were bonded to the plate by using instant glue. Additionally, 15 electrical strain gauges (MMF307441, Micro-Measurements) were mounted on the plate adjacent to each FBG strain sensor. The electrical strain gauges were used to calibrate the sensitivities of the mounted FBG strain sensors before the slamming experiments.

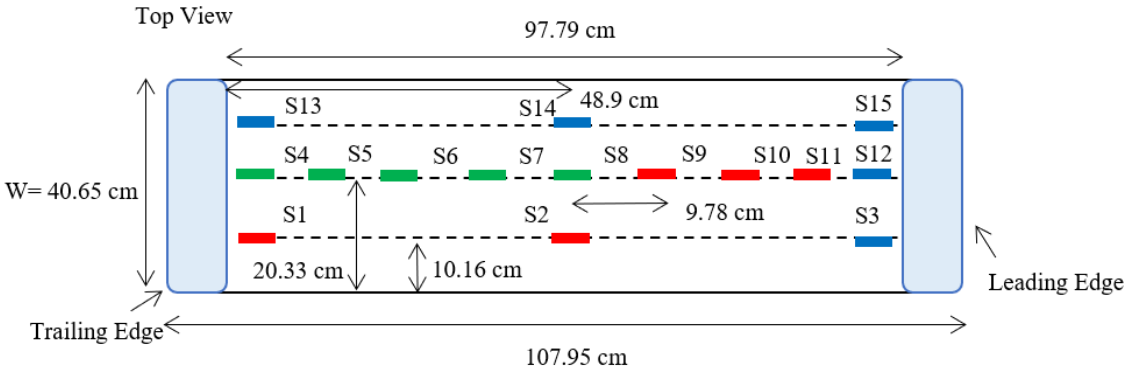

Figure 4-4: The top surface of the aluminum plate is instrumented with 15 FBG strain sensors.

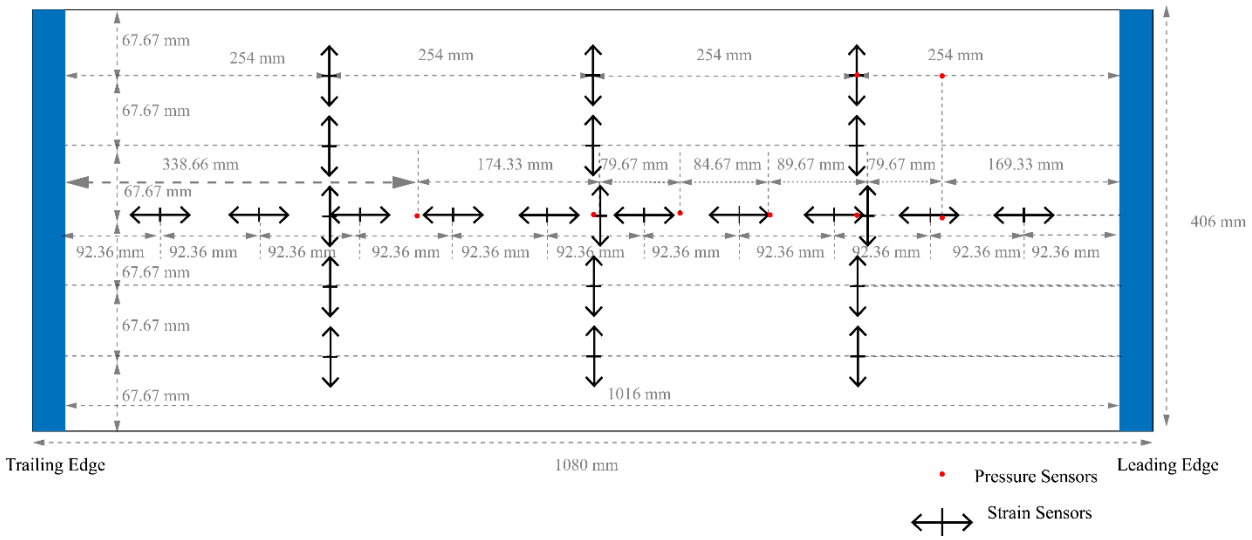

Figure 4-5: Schematic of the experimental setup for dynamic strain and pressure measurements of the flexible plate during 2nd water slamming test. 10 and 15 FBG strain sensors were installed longitudinal and transverse along the top surface of the plate, respectively. 8 FP pressure sensors were flushed-mounted and on the bottom surface of the plate.

25 FBG strain sensors and 8 FP pressure sensors were deployed for the 2nd slamming conditions experiment. The 1st slamming experiment result showed the strain response of along the transverse direction is similar. Thus, more sensors were deployed along the centerline to increase the spatial resolution. 10 FBG strain sensors were mounted at a uniform distance along the centerline. Furthermore, 15 FBG strain sensors were deployed transverse along with the plate. The primary goal of this set of sensors was to measure the modal shape of the plate.

The sensitivities of the mounted FBG strain sensors were calibrated against the adjacent electrical strain gauges. For sensor calibration, static loads were applied at the center of the aluminum plate by using a set of weights, as shown in Figure 4-6. Figure 4-7(a) shows the reflection spectra of the multiplexed FBG strain sensors obtained for different applied weights. The Bragg wavelengths of the FBG strain sensors were redshifted as the applied weight

increased. Figure 4-7(b) shows the measured Bragg wavelengths of a representative FBG sensor at different weights, and Figure 4-7(c) shows the corresponding strain measured by the reference electrical strain gauge. When the plate was free of loading, the non-zero initial strain was due to the self-weight of the plate. The measured Bragg wavelengths were matched to the corresponding strain, as shown in Figure 4-7(d). Figure 4-8 shows the surface plot of the strain response under 200 lbs loads by interpolating the scatted data across the plate. The largest strain was observed at the center of the plate, where the applied load was concentrated.

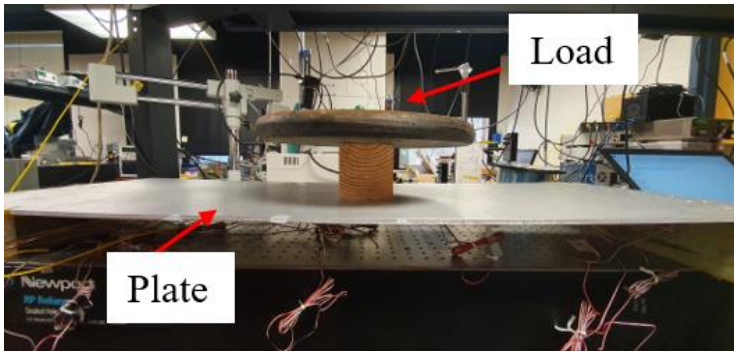

Figure 4-6: Photograph of the experiment of strain sensitivity calibration. Static loads were applied at the center of the plate.

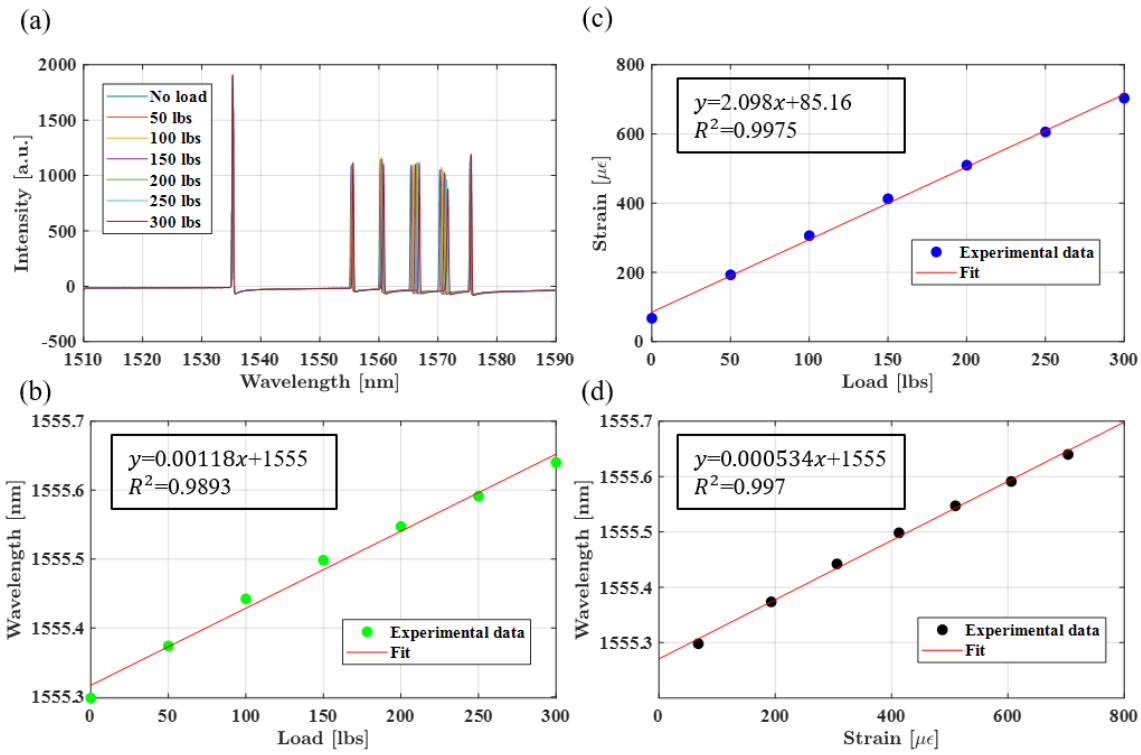

Figure 4-7: Sensor calibration results. (a) Reflection spectra of the multiplexed FBG strain sensors on the aluminum plate at different weights. (b) Bragg wavelength shifts under static weight loadings were obtained for a representative FBG strain sensor and (c) the corresponding strain as a function of applied weight. (d) Bragg wavelengths of the representative FBG strain sensor as a function of strain.

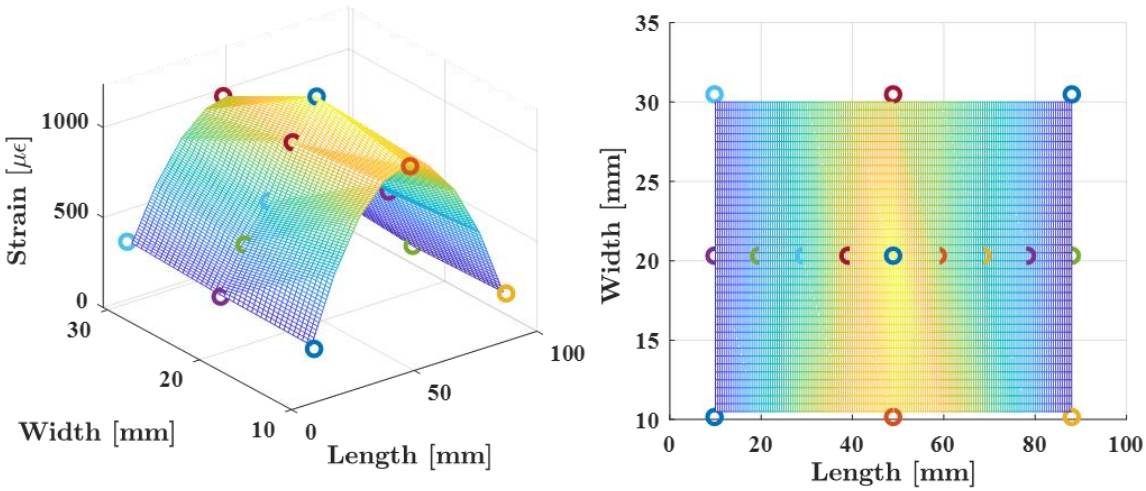

Figure 4-8: Strain distribution along with the plate at 200lbs load. The circle dots represent the FBG sensors.

4.3.3 Result and discussion

4.3.3.1 Strain response of 1st set of slamming experiment

Figure 4-9 shows the strain response obtained with the fifteen FBG strain sensors on the plate in the V_n=1.38 m/s with U/W = 8.3. Prior to the time when the trailing edge passed through SWL (t = 0.33 sec and z = -117.7 mm), the small strain was due to the vertical and horizontal accelerations of the plate in the air. After the plate hit the water surface, a large strain was developed on the plate due to the water flow-induced pressure. The strain peaks occurred before the plate was fully submerged in the water (t = 0.66 sec), and the maximum strain (1200 με) was obtained from the FBG strain sensor (S7) located at the center of the plate. Furthermore, the peak strain occurrence time was influenced by the sensor location. The strain peaked occurred earlier for the sensor close to the trailing edge. The Peak strain of S6 (700 με) is larger than S10 (412με) become of the asymmetrical mounting (α = 10°).

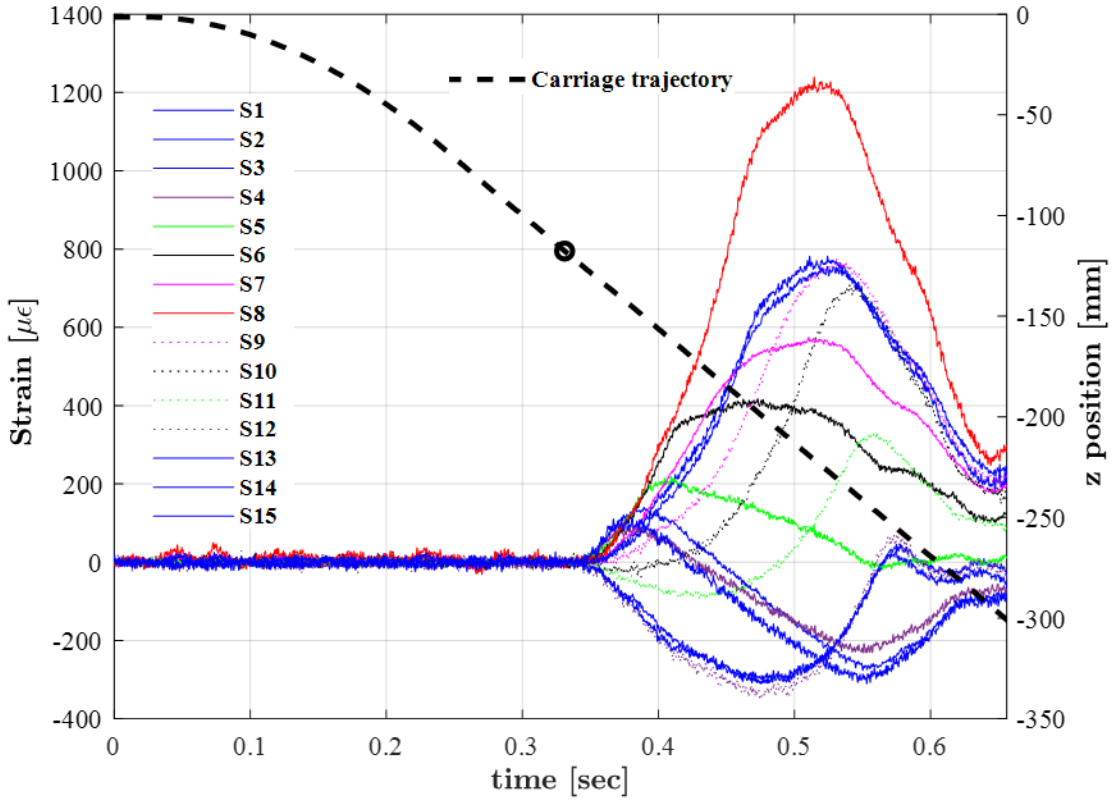

Figure 4-9: Strain response of 15 FBG strain sensors mounted on the plate during the oblique impact of the plate on the water surface at $V_n = 1.38$ m/sec with $U/W = 8.3$. The black dashed line indicates the vertical position of the carrier as a function of time. The mean water surface is at z= -117.7 mm. The lowest and highest corners of the plate passed the mean water surface at 0.33 sec and 0.66 sec, respectively, as indicated by the circles.

Plots of strain versus time for a variety of U/W (8.33, 6.28, 5.5, and 4.5) and thickness of the plate (h = 7.95 mm and h = 6.35 mm) are presented in Figure 4-10. Subplots (a) and (b) the time is the dimensional data ($t - t_i$) while subplots (c) and (d) the time is the nondimensional data by submergence time $T_s = Lsin\alpha/W$. Figure 4.11(d) shows the peak strain occurred at the same dimensional time (~0.9) for all cases of U/W, h = 6.35 mm. The peak strain value is

lower as the U/W decreases. However, Figure 4-10 (c) shows the peak strain occurred later as U/W decreases. Furthermore, the strain almost reached zero before the plate (h = 7.95 mm) was fully submerged in the water. The plate (h = 6.35 mm) took more time to reach the peak value in nondimensional time.

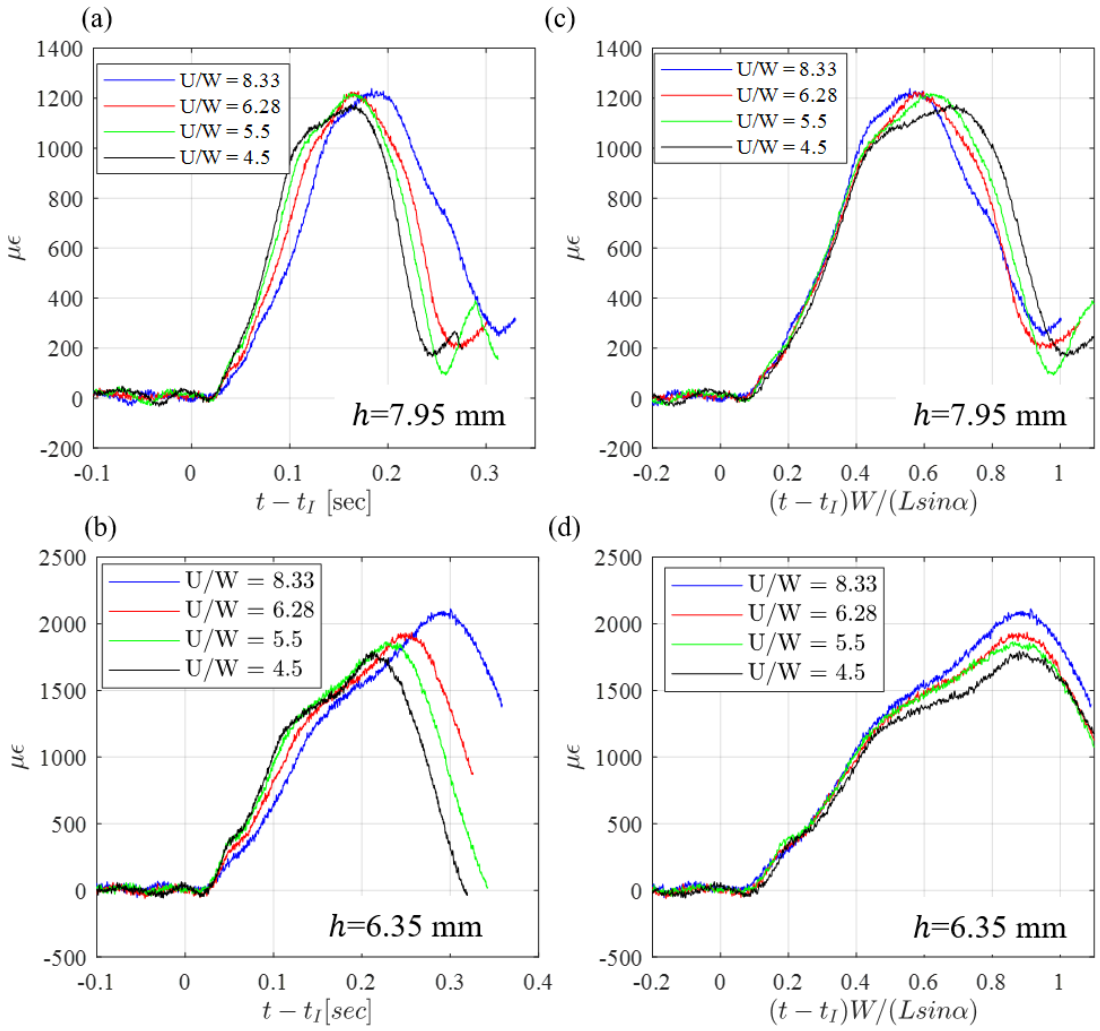

Figure 4-10: Strain measured by the FBG sensor at the center of the plate versus time for various impact U/W ratio at V_n =1.39 m/s with various thicknesses of plates. (a) Strain response obtained by the FBG S7 versus time after the initial impact (t-t_i, where t_i is the time when the trailing edge of the plate reaches the SWL), h=7.95mm. (b) Strain response vs. nondimensional time for various U/W at V_n = 1.39 m/s, h=7.95mm. (c) Strain response vs. time after initial impact for various U/W, h =6.95mm. (d) Strain response vs. nondimensional time for various U/W at V_n = 1.39 m/s, h =6.95mm.

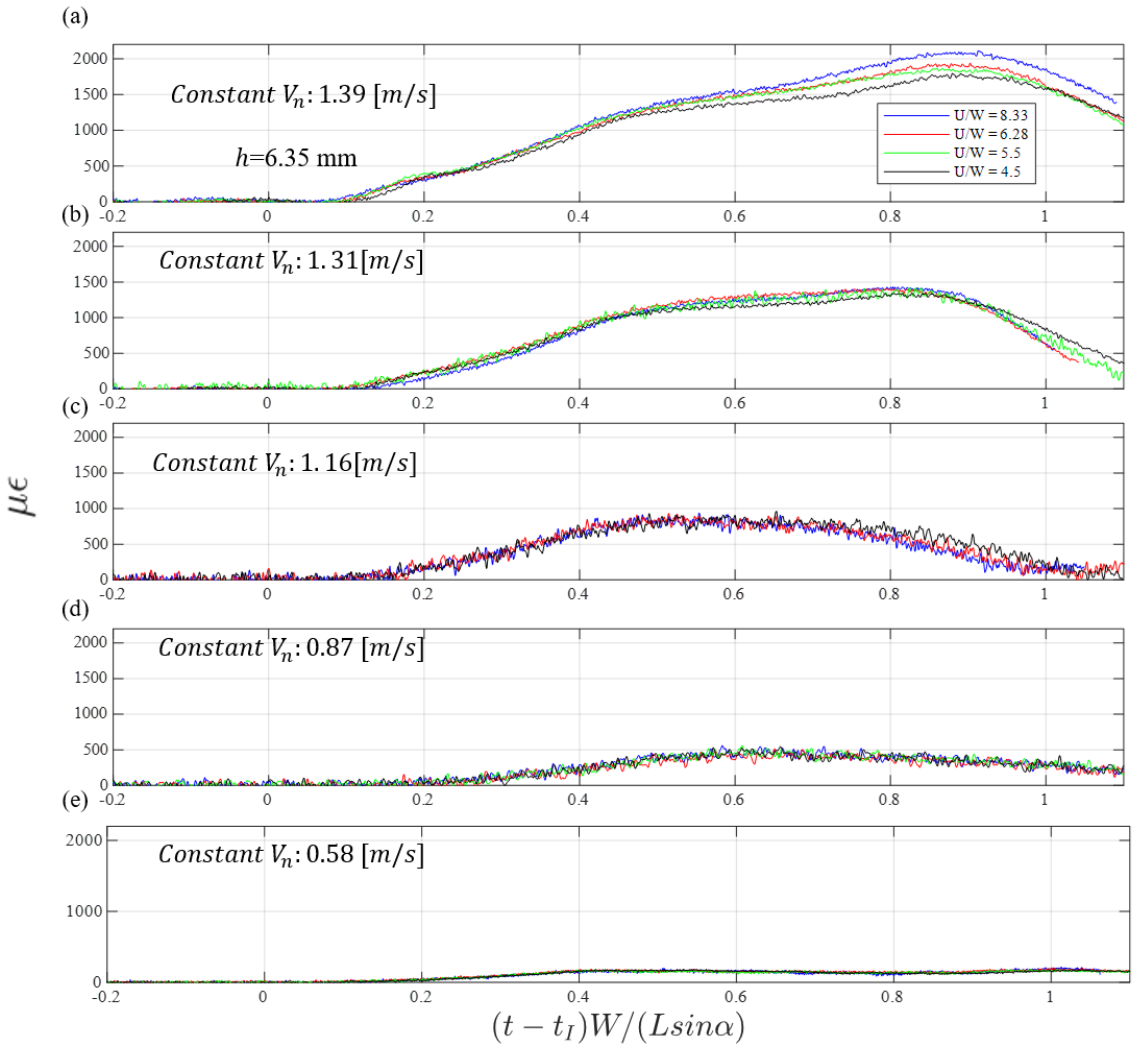

Figure 4-11: Strain response obtained by the FBG S7 mounted on the plate (h= 6.35 mm) versus nondimensional time for various U/W and various normal impact velocity (a) V_n = 1.39 m/s, (b) V_n= 1.31 m/s, (c) V_n= 1.16 m/s, (d) V_n= 0.87 m/s and (f) V_n= 0.58 m/s.

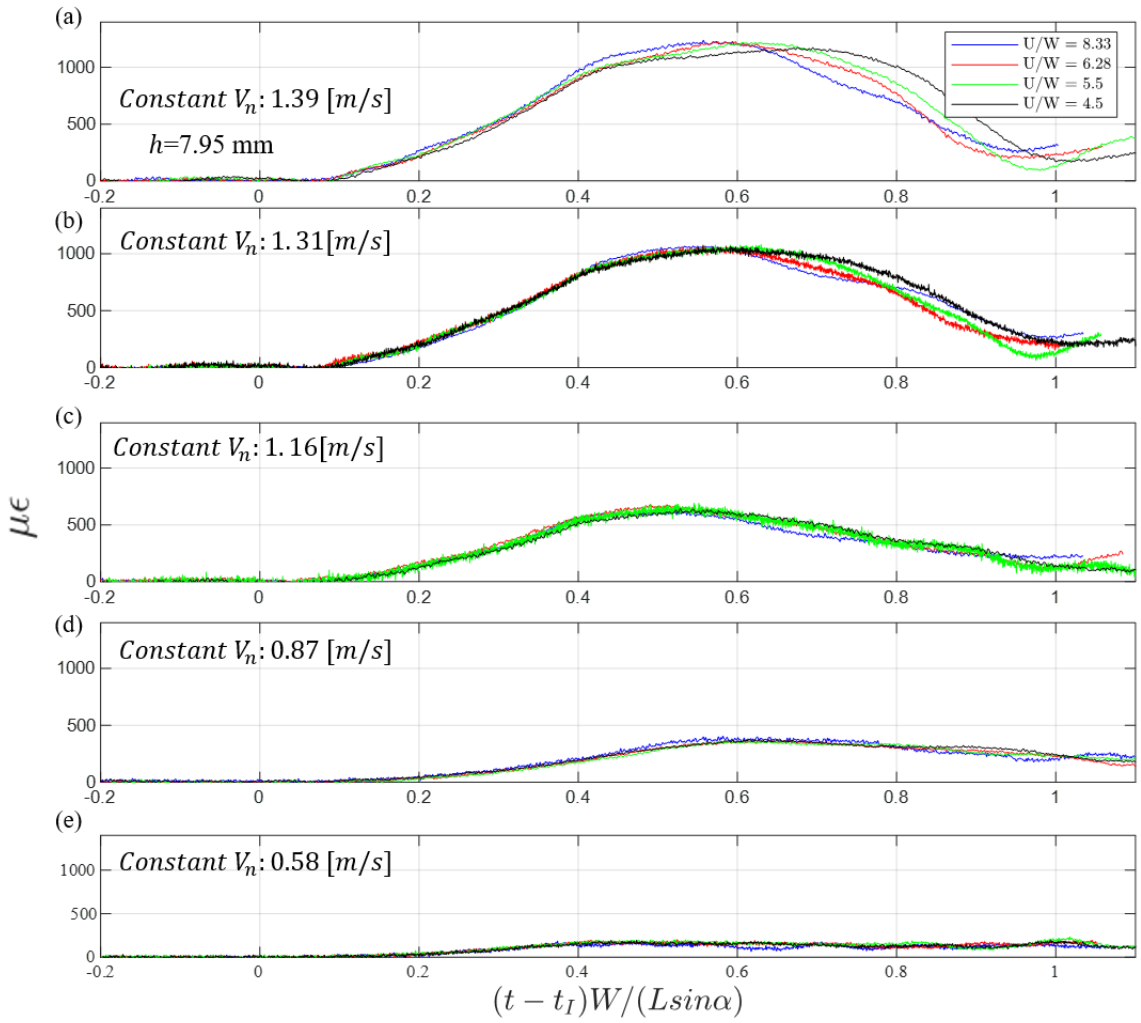

Figure 4-12: Strain response obtained by the FBG S7 mounted on the plate (h=7.95 mm) versus nondimensional time for various U/W and various normal impact velocity (a) V_n= 1.39m/s, (b) V_n= 1.31m/s, (c) V_n= 1.16m/s, (d) V_n= 0.87m/s and (f) V_n= 0.58m/s.

Figure 4-11 and Figure 4-12 show the strain obtained by S7 versus nondimensional time for various U/W and V_n (1.39 m/s, 1.31 m/s, 1.16 m/s, 0.87 m/s, and 0.58 m/s). Given the same slamming condition, the maximum strain value of plate (h= 6.35 mm) is larger than the thickener plate (h= 7.95 mm). As V_n increase, the maximum strain value between U/W is larger. The strain data almost overlap for various U/W with V_n= 1.16, 0.87, and 0.58 m/s as Figure 4-13 shown.

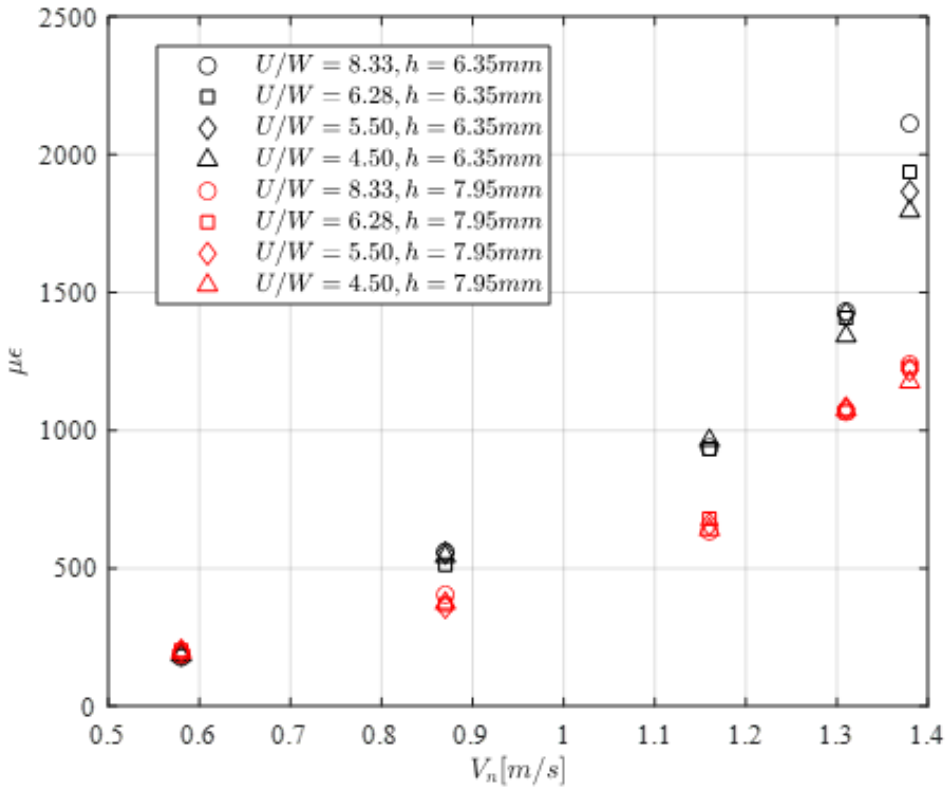

Figure 4-13: Maximum strain at the center of plate versus V_n for the plate with thickness h= 6.35 mm and h= 7.95 mm for various U/W.

Figure 4-14 and Figure 4-15 show the strain response obtained from S7 versus various scaling in time for vertical slamming. For the slower slamming conditions (V_n = 0.59, 0.44, 0.30 m/s), strain response is flat out until the plate fully submerged into the water.

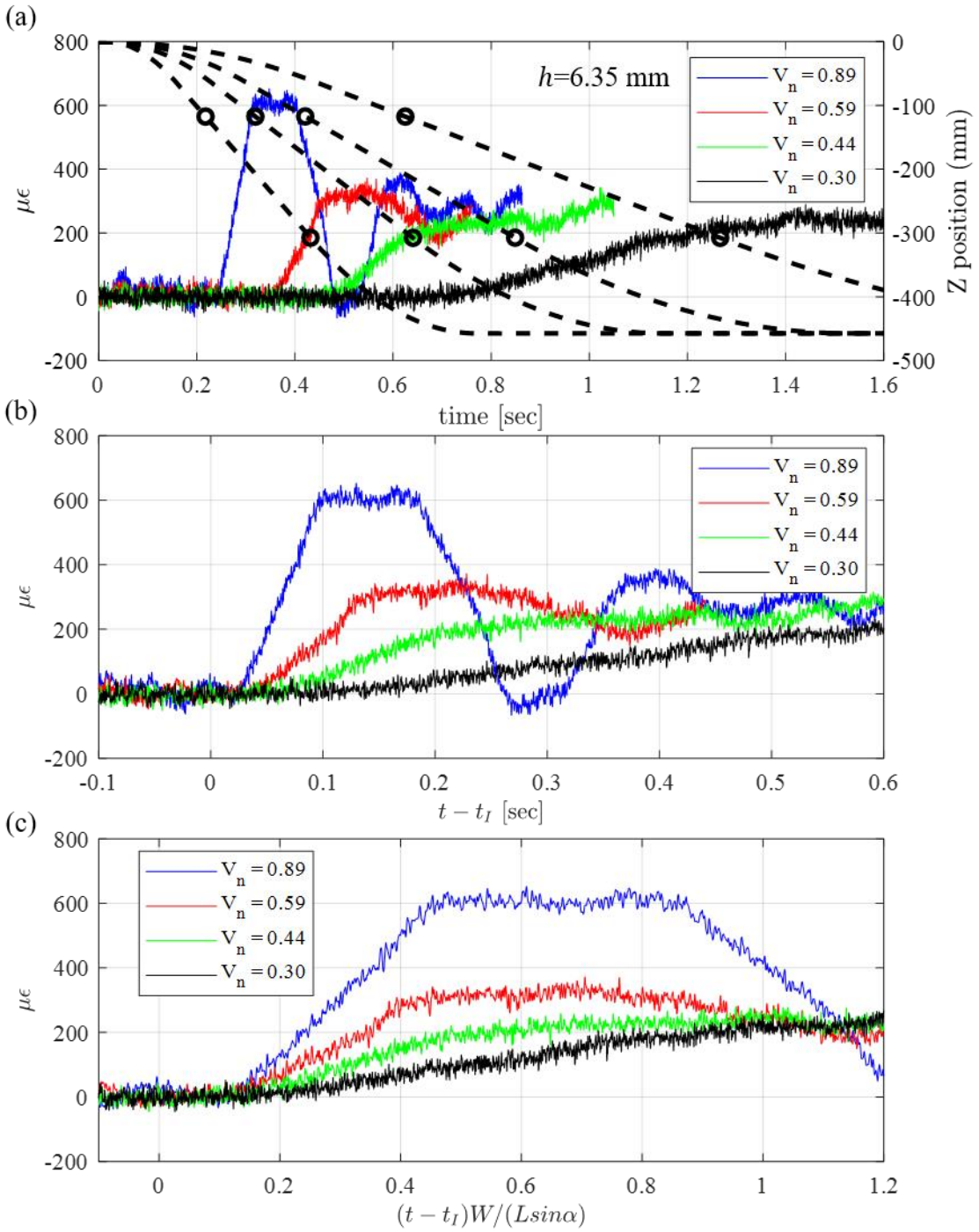

Figure 4-14: Strain response obtained by the FBG S7 mounted on the plate (h=6.35 mm) for the vertical slamming result for various V_n versus (a) non-scaled time, (b) time after initial impact, and (c) non-dimensional time.

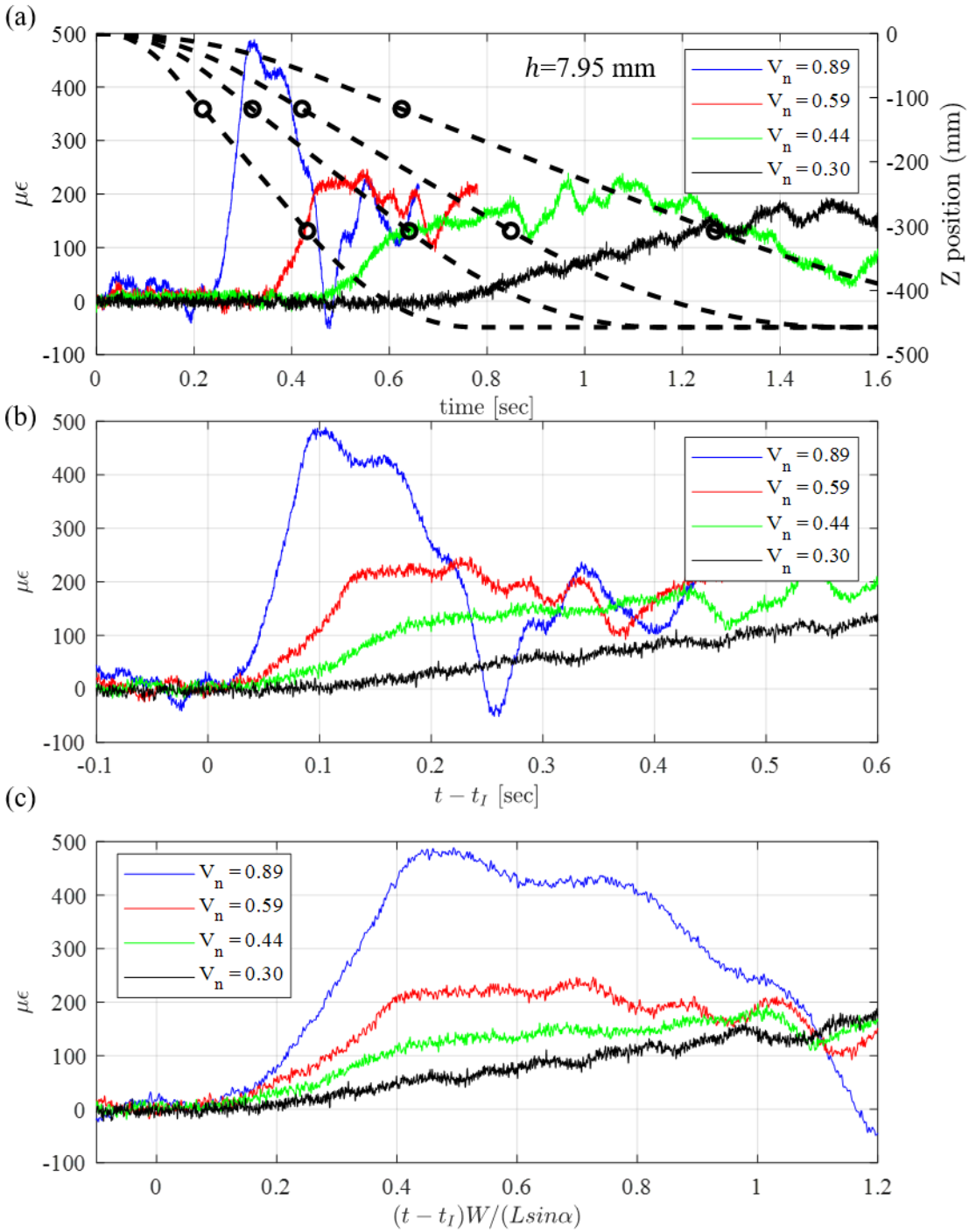

Figure 4-15: Strain response obtained by the FBG S7 mounted on the plate (h=7.95 mm) for the vertical slamming result for various V_n versus (a) non-scaled time, (b) time after initial impact, and (c) non-dimensional time.

4.3.3.2 Strain response of 2nd set of slamming experiment

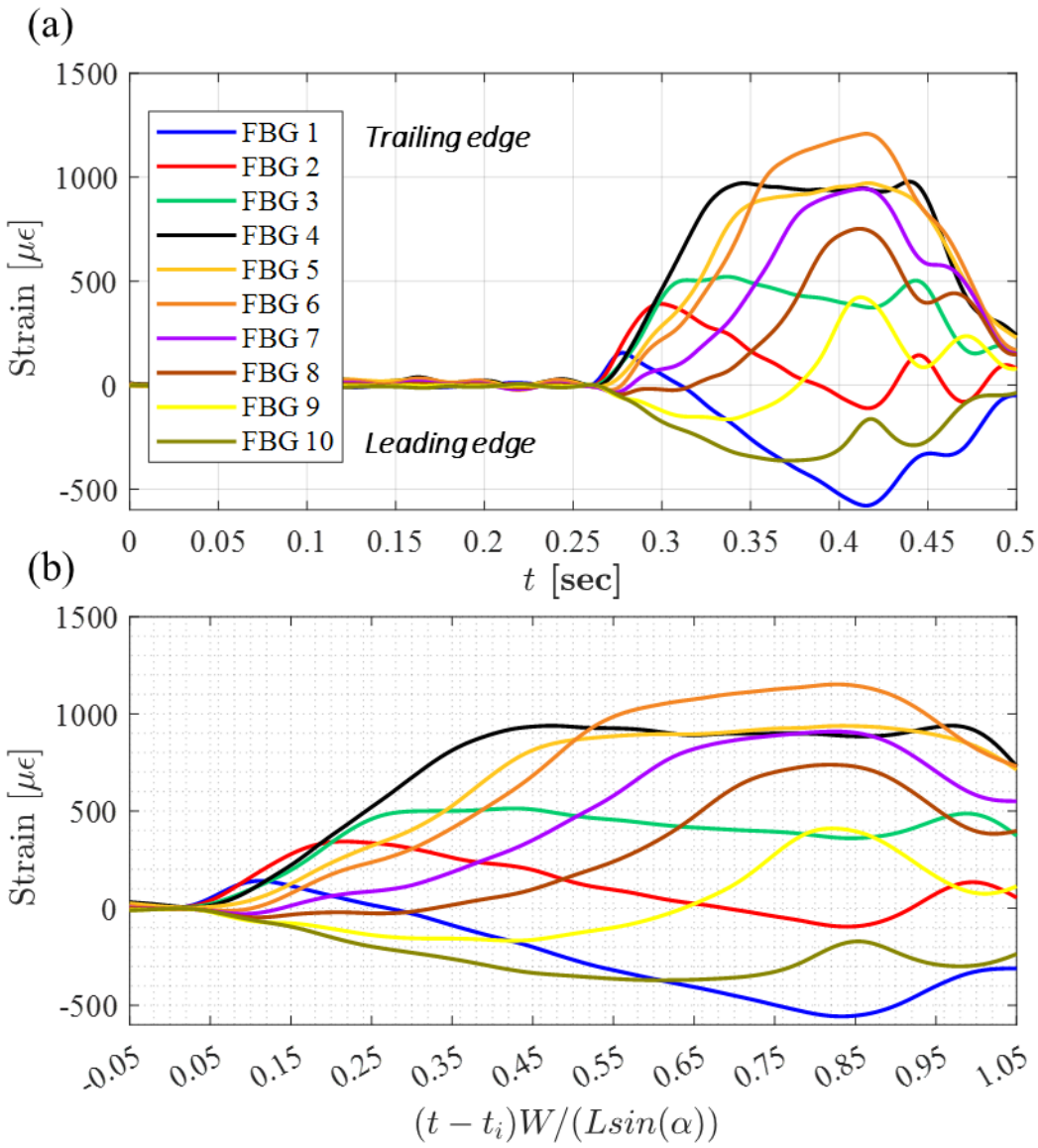

Figure 4-16: Strain response obtained by the FBG longitudinal strain sensors mounted on the plate (h= 6.35 mm) versus time (a) and nondimensional time (b) with a pitch angle of 7.5° at V_n *= 1.18 m/s and* U/W *=4.53.*

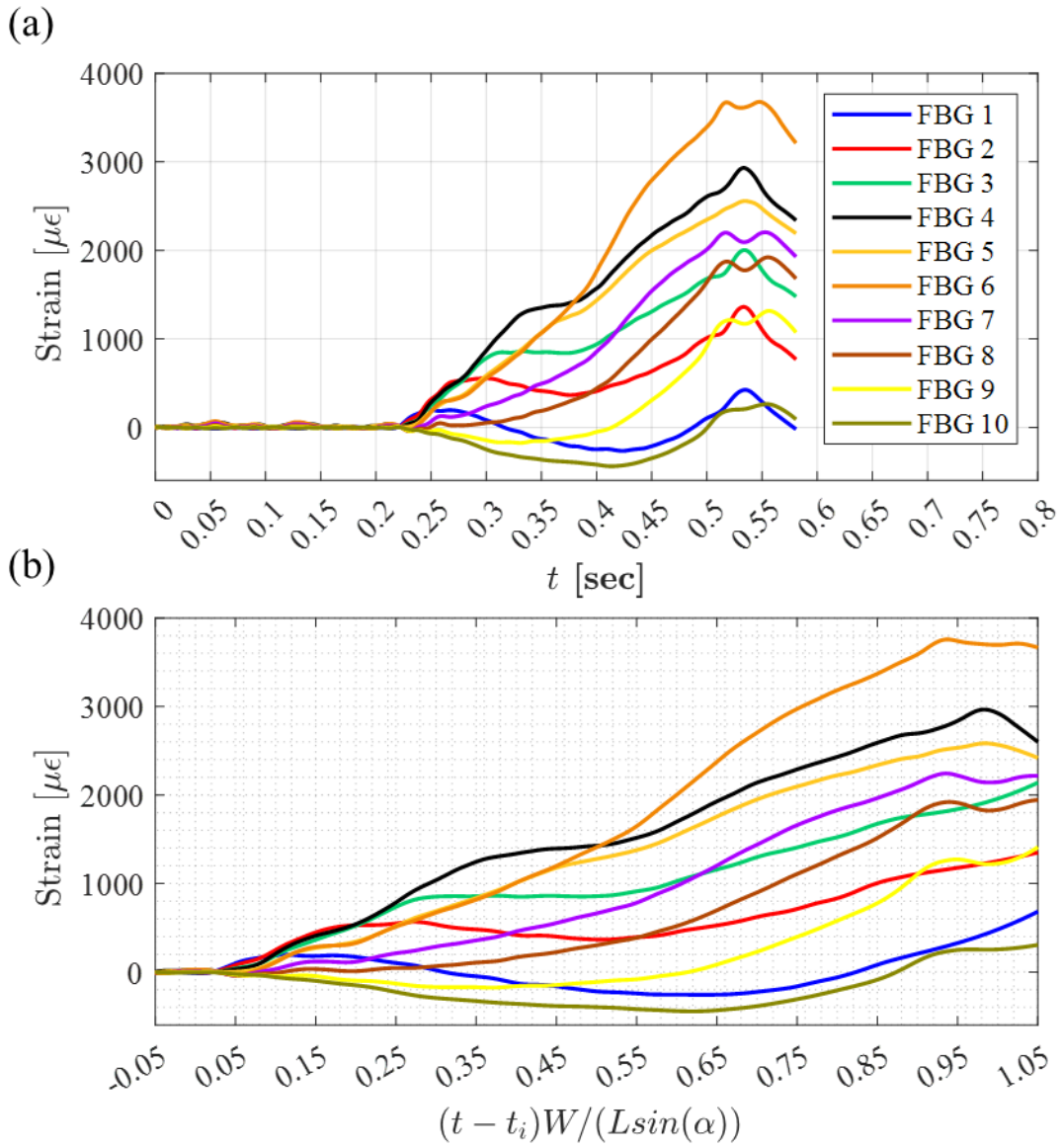

Figure 4-17: Strain response obtained by the FBG longitudinal strain sensors mounted on the plate (h= 6.35 mm) versus time (a) and nondimensional time (b) with a pitch angle of 7.5° at V_n = 1.39 m/s and U/W =7.38.

Figure 4-16 and Figure 4-17 show the strain response obtained by the FBG strain sensors which were mounted longitudinally along with the plate with a thickness of 6.35mm versus time and nondimensional time (tT_S^{-1}). When tT_S^{-1} =1, the experiment is considered finished because the leading edge of the plate had reached the mean water level. Noted that the total duration

time of the measurement is 1.08 sec, and all the slamming events finished under 1sec. However, the signal of the strain sensor is interrupted and lost by a large bending of the fiber when the slamming speed is high as Figure 4-17 shown. This shows the fiber arrangement and installation need to be improved for a more violent motion in the future.

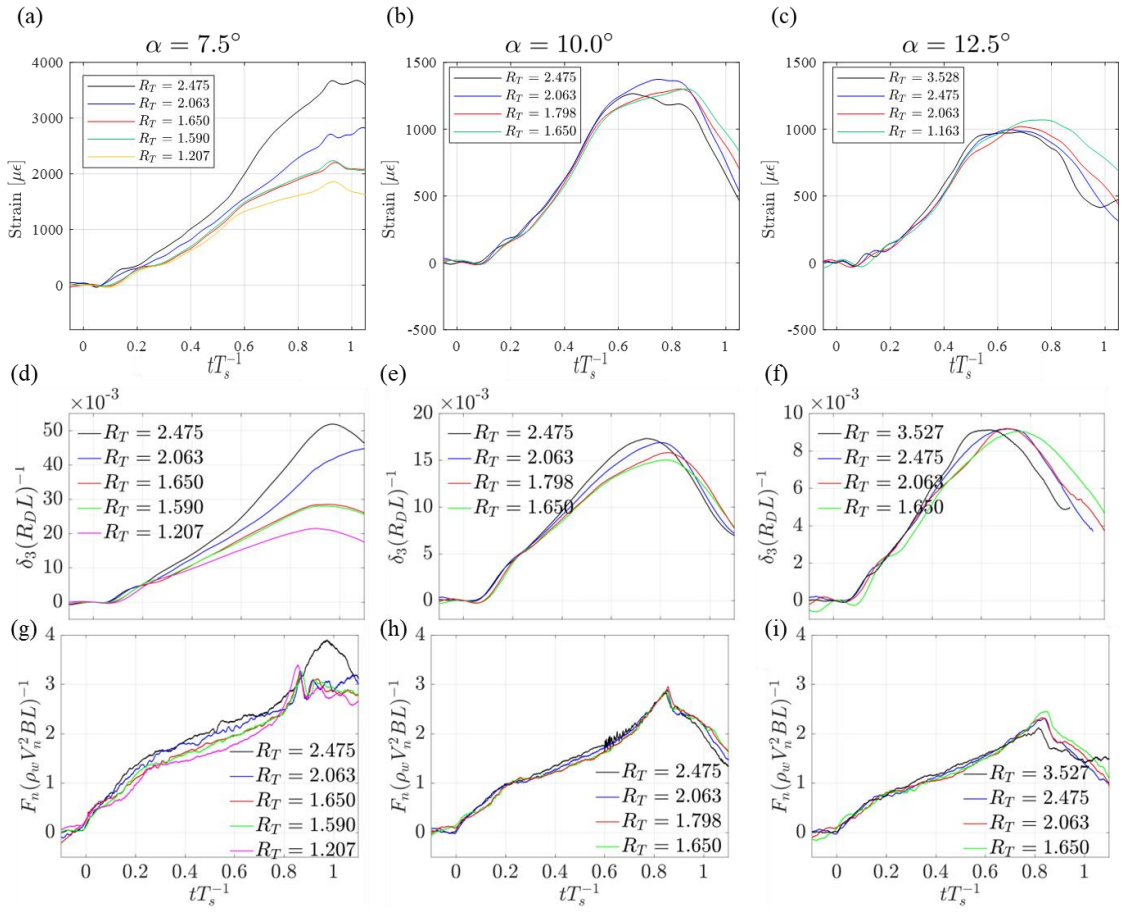

Figure 4-18: The strain response (a-c) of the FBG 6 at the center of the plate, the dimensionless normal force (d-f), and the dimensionless normal force (g-i) versus nondimensional time for various pitch angles with various R_T .

Figure 4-18(a)-(c) shows the strain response versus tT_S^{-1} obtained by the FBG 6 strain sensor which recorded maximum the strain level for varying R_T, where $R_T = \frac{T_s}{T_{1w}}$. And T_{1w} is the

lowest order natural period of the plate when its lower surface is in the water while its upper surface is in air. For the present plate, the T_{1w}= 0.133. The dimensionless deflection $\delta(R_D L)^{-1}$ response versus tT_S^{-1} is shown in figures 4-19 (d)-(f). The location of deflection sensor is at the center of the plate. The dimensionless normal force $F_n^* = F_n(\rho\omega V_n^2 BL)^{-1}$ versus tT_S^{-1} is shown in Figure 4-18(g)-(i). Both deflection and force response is recorded by the hydrodynamic group. At α =12.5°, the maximum strain increased slightly with increasing impact speeds, which was in good agreement with the behavior of the measured maximum deflection and force. The strain peaks occurred before the plate fully submerged into the water ($tT_s^{-1} = 1$) for α =12.5° and 10°. However, the strain keeps increasing after tT_S^{-1} = 1 for α =7.5° with R_T =2.063 and the deflection data was in good agreement as well.

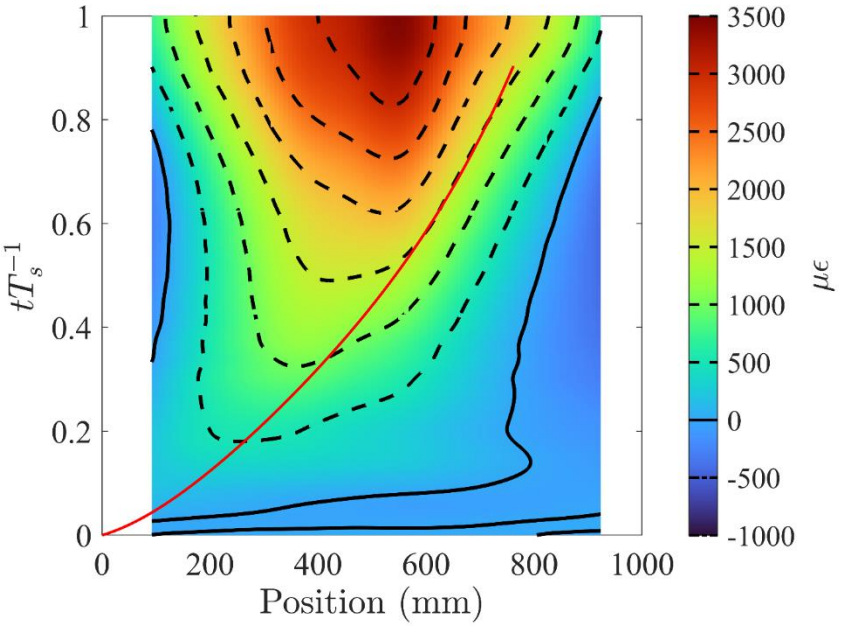

Figure 4-19: The contour plot of the strain response vs position in the dimensionless time domain at V_n= 1.38 m/sec with U/W= 17.27 and α=7.5°. The spray root position vs time is labeled in red color.

The contour plot of the longitudinal strain response versus position in the dimensionless time domain is shown in Figure 4-19. The longitudinal strain response along with the plate also showed a good agreement with the spray root which is labeled in the red line. As the spray root velocity increased, the rate of change of the strain also increased well.

4.4 Preliminary study of pressure sensing

4.4.1 Overview of the preliminary study

Before deploying the FP optical pressure sensor on the flexible plate to monitor the dynamic pressure response during the slamming, the FP pressure sensor was first used to monitor the dynamic pressure response induced by a breaking wave with a reference MEMS pressure sensor. The goals of this experiment were to compare the pressure responses from different mounting orientations and to investigate the temperature drift due to the temperature difference between air and water.

The experiments were performed in the hydrodynamic laboratory at the University of Maryland. The wave tank is 14.8 m long, 1.2 m wide, and 2.2 m tall. The wave tank consists of a programmable wavemaker and a vertical stainless-steel plate. 20 piezoelectric pressure sensors (113B28, PCB Piezotronic Inc) are flush-mounted on the stainless-steel plate to monitor the pressure response induced by the plunging breaking wave. The piezoelectric pressure sensing system was well established by Dr. An Wang. The details of the wave tank and the sensing system were discussed in [89]. Figure 4-20 shows the photograph of the stainless-steel plate with PZT reference sensors and how the wave impacts the structure. The PZT pressure sensor monitors the transient pressure load induced by the plunging breaking wave impacting the wall.

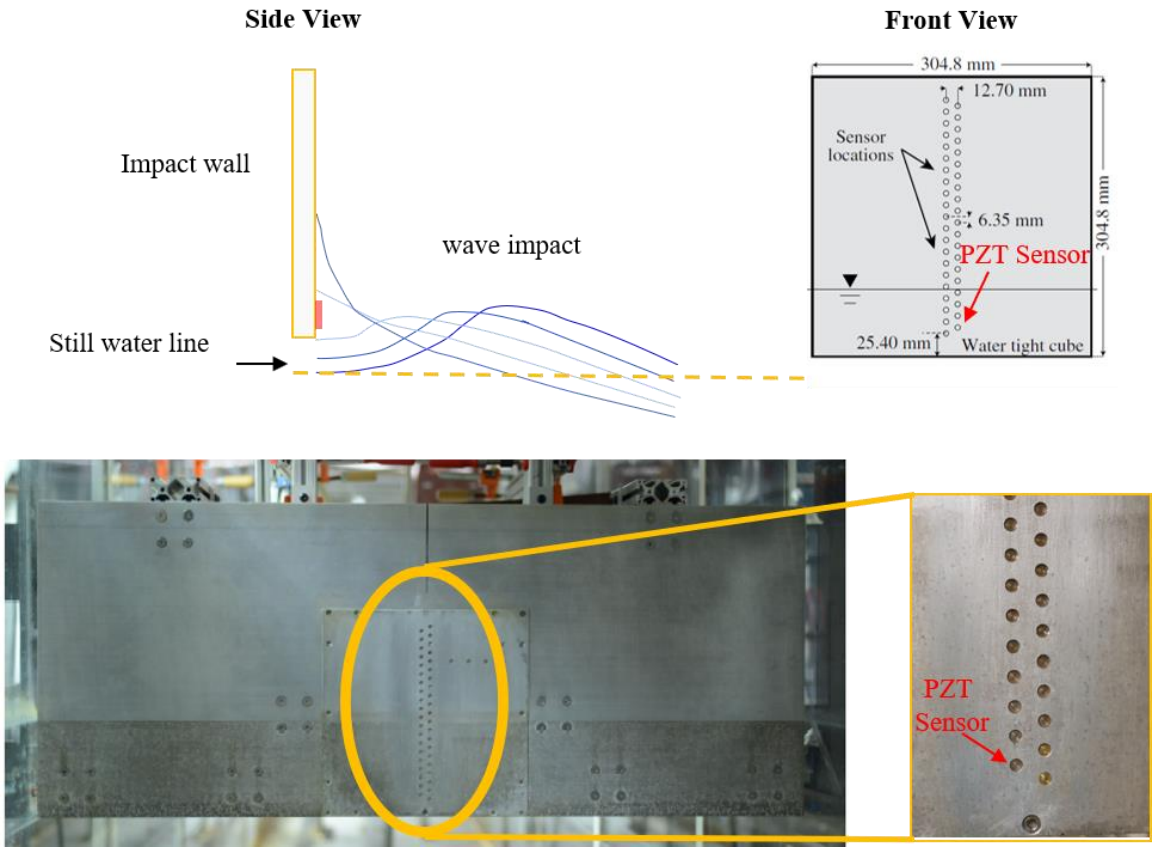

Figure 4-20: Schematic of the plunging breaking wave tank.

Four FP optical single cavity pressure sensors were mounted on the impact wall with different orientations: flush, up, down, and lateral surface mount, as shown in Figure 4-21. The flush mount FP pressure sensor was fixed by using a holder, and the surface mounts FP sensors were bonded to the plate by using instant glue and Kapton tapes. The FP sensors were placed close to the reference PZT sensor to obtain a similar pressure response.

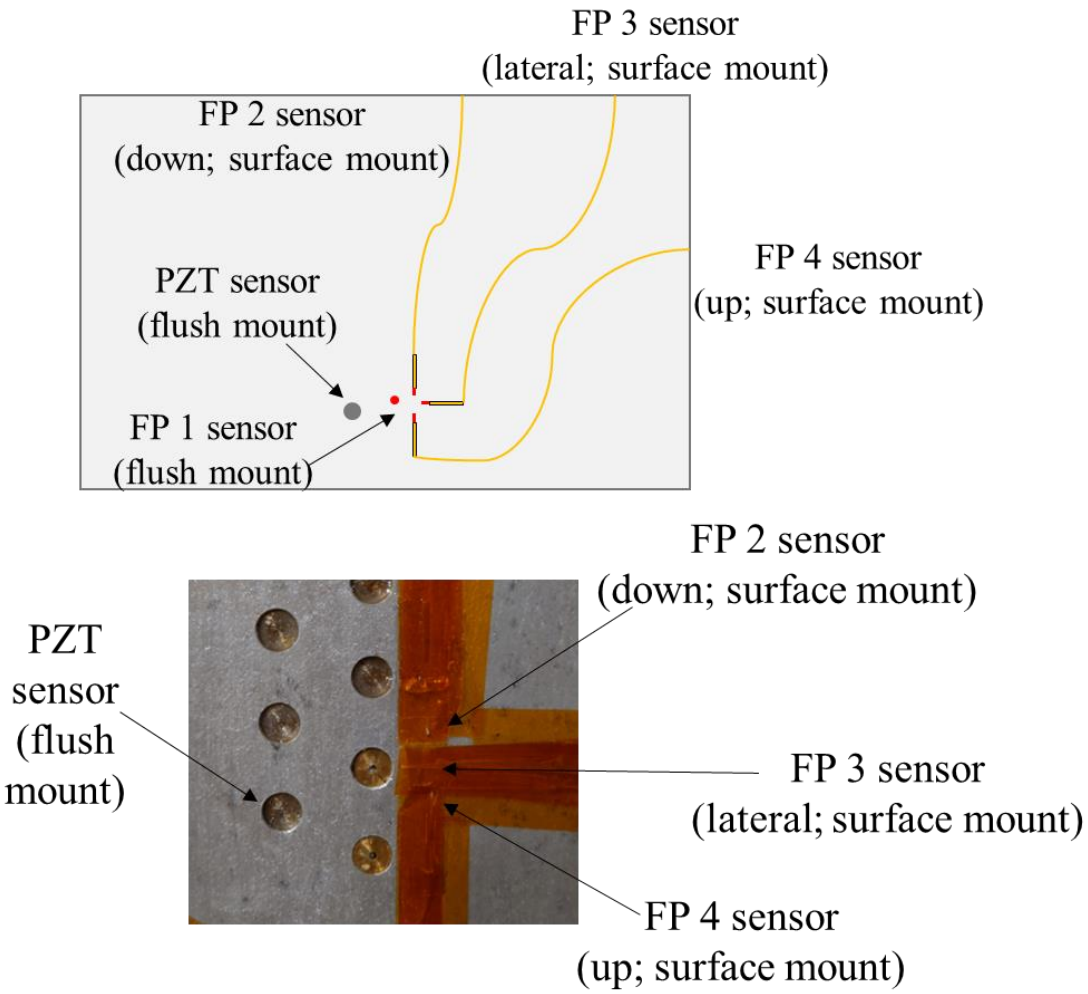

Figure 4-21: Pressure sensors layout.

The acquired signal was demodulated to retrieve the pressure value by using the quadrature point sensing method, as shown in Figure 4-22. A broadband light source is coupled to the FP tunable filter. A DC voltage is applied to the tunable filter by using a function generator. It allows a narrow bandwidth light to pass through to the FP sensor. The tunable filter is adjusted by the offset of the DC voltage so that the narrow bandwidth light is set on the linear region of spectra of the FP sensor, as shown in Figure 4-23. The output light from the tunable filter is coupled to the FP sensor through a circulator. The reflected light intensity is measured by the

photodetector, and the output signal from the photodetector is received by DAQ. The reflected light intensity changed as the reflection spectra shifted [90][91][92][93].

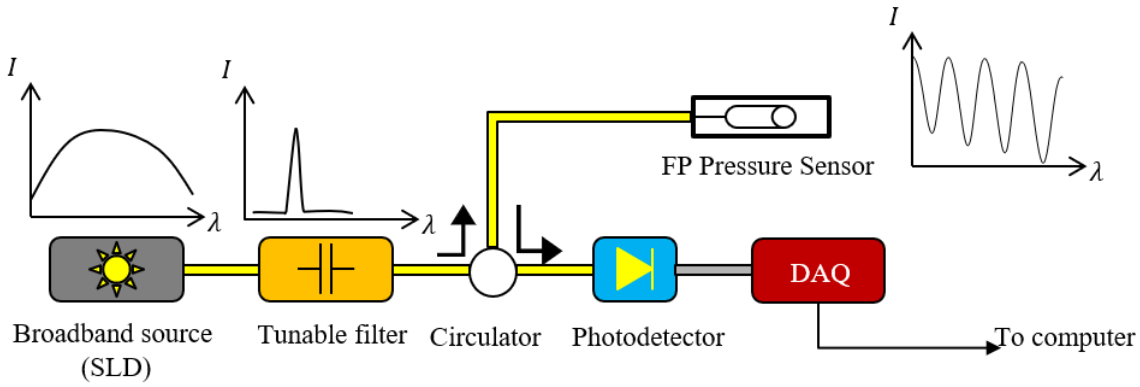

Figure 4-22: Schematic diagram of quad-point sensing with FP sensor.

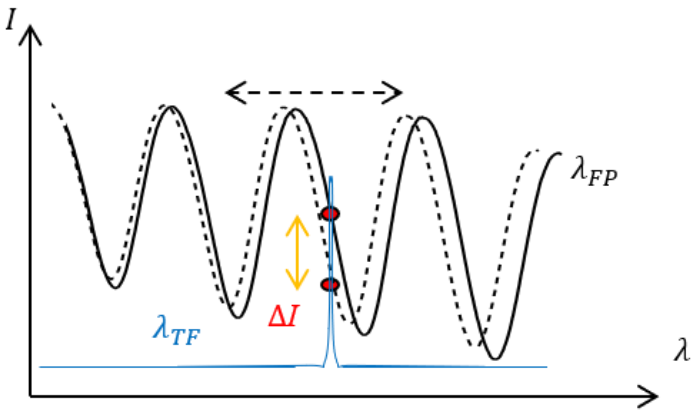

Figure 4-23: Schematic of the principle of quad-point sensing interrogation.

4.4.1.1 Results and discussion

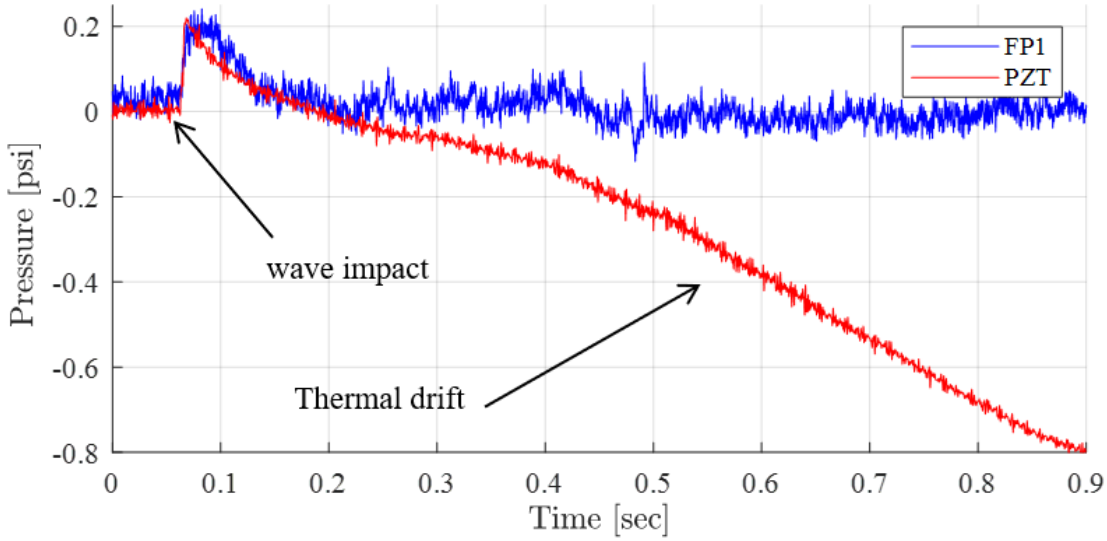

Figure 4-24: Pressure response of FP flush mount sensor and PZT sensor.

Figure 4-24 shows the pressure responses obtained by the flush mount FP pressure sensor and PZT reference sensor on the plate. After the plunging breaking wave hit the plate (t = 0.064 sec), a transient pressure was developed on the plate induced by the water jet. After the impact, the pressure level should be zero. The PZT sensor is covered with insulating grease, which delays the thermal drift. However, the PZT sensor still suffered from thermal drift (Δtemp = 1.2 °C) between the air and the water. The signal obtained by the FP sensor was filtered by a bandpass filter (10-100 kHz) to remove the thermal drift. The pressure responses of the FP sensor and PZT sensor show good agreement in terms of pressure value and timing.

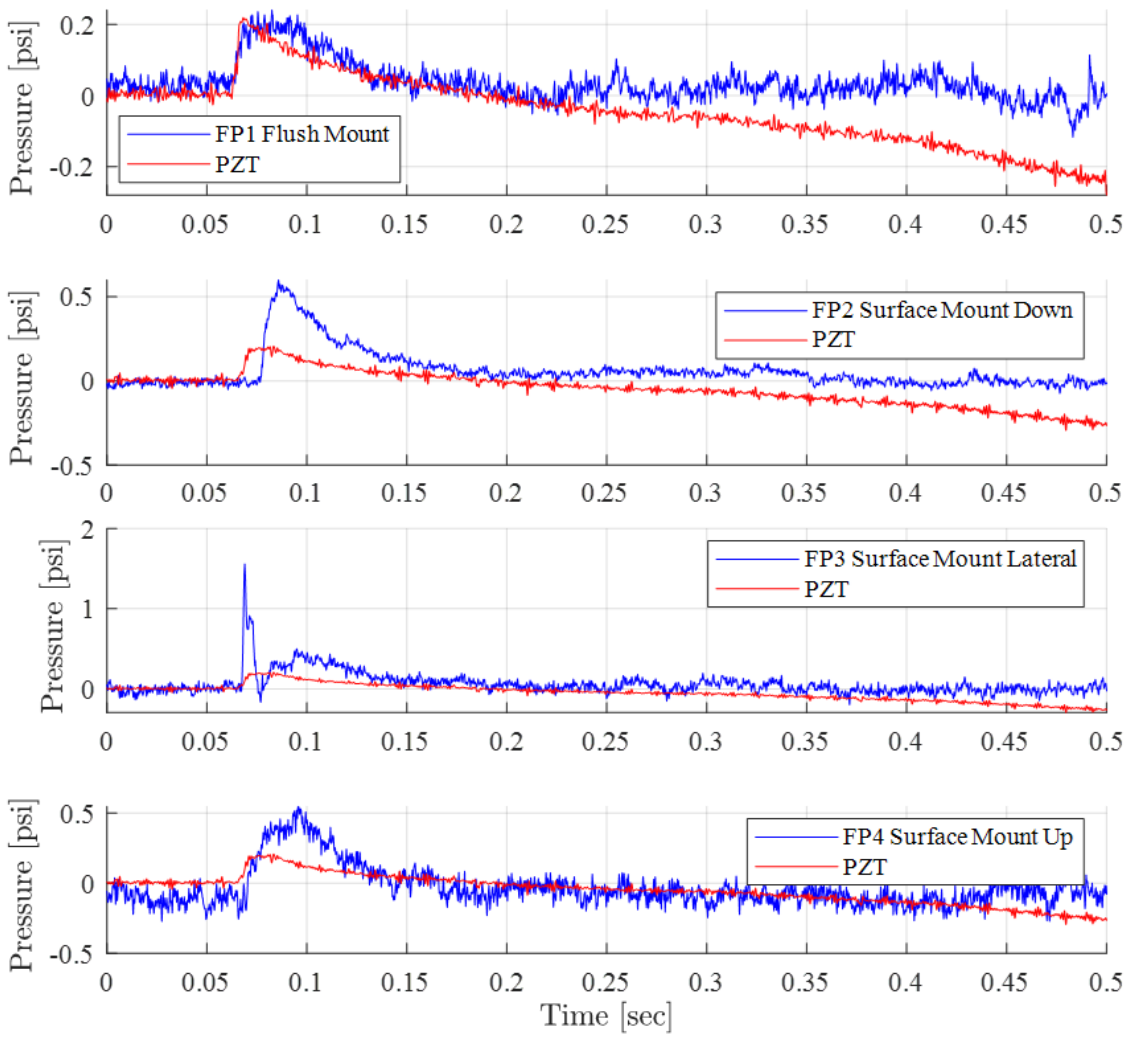

Figure 4-25: Pressure responses of FP sensors versus reference PZT sensor.

Figure 4-25 shows the pressure response of four FP pressure sensors versus the reference PZT sensor. The pressure response of the FP 2 surface occurred later (Δt = 0.01 sec) than the reference PZT sensor because of the location of the sensor. When the wave impacted the plate, the water sprayed from the bottom to the up. The pressure response of flush mount FP pressure is similar to the pressure response of the PZT pressure sensor in terms of pressure value and tread. The surface mounts FP sensors have a similar tread but a different pressure value. Figure 4-26 shows the flush mount FP sensor is more repeatable than the surface mount sensors.

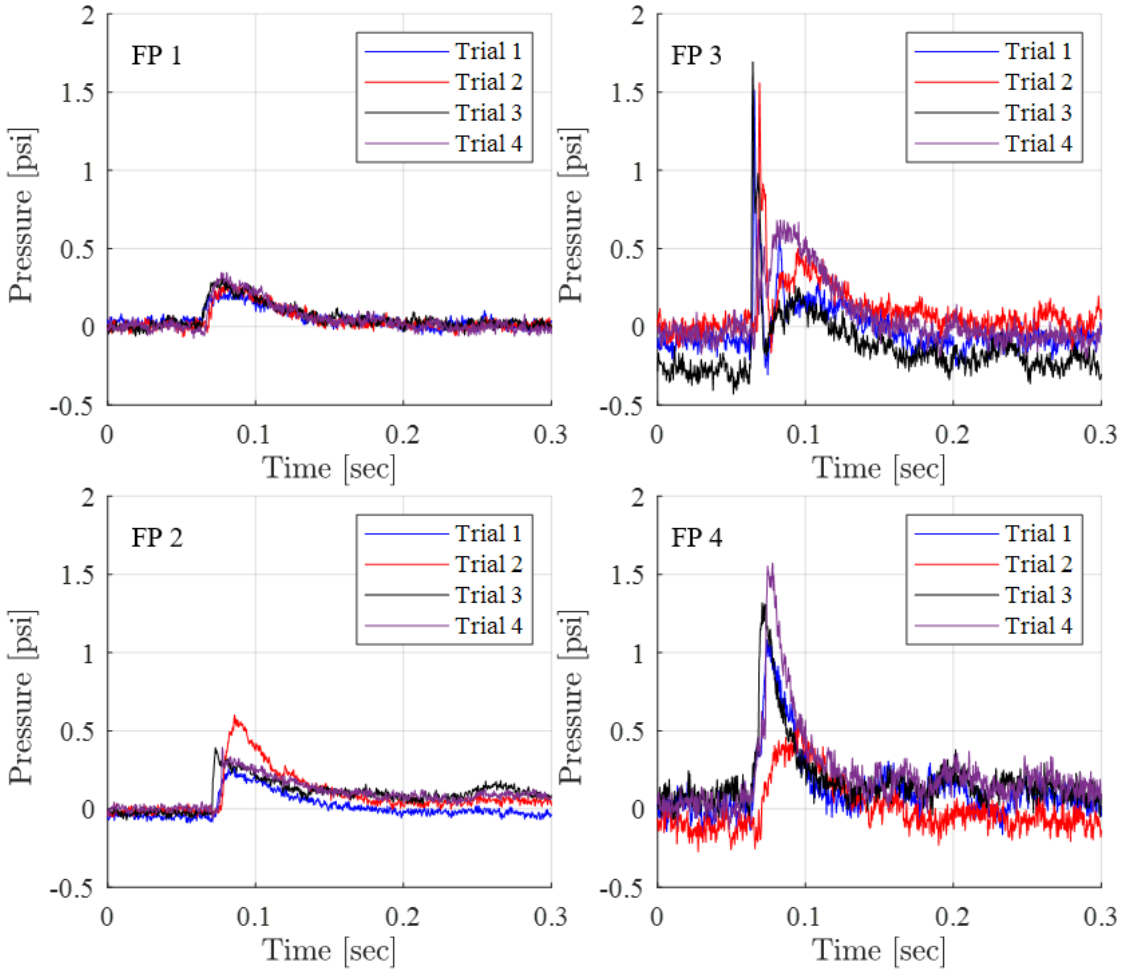

Figure 4-26: Reparability of pressure responses of FP sensors.

In conclusion, the preliminary study shows that flush-mounted orientation is the better approach to tackle the pressure measurement on the flexible plate during slamming in terms of repeatability and accuracy of reading the pressure level. The preliminary study also shows that the photon-detector bandpass filter can remove the thermal drift due to the temperature change between water and air. The temperature compensation with the bandpass filter is used in the following transient pressure measurement.

4.5 Pressure response of slamming experiments

4.5.1 Pressure response of the vertical slamming experiments

Before deploying multiple FP pressure sensors for the measurement of a flexible plate slamming to a water surface with all the conditions, a single FP sensor was used for this preliminary testing. The schematic of pressure installation is shown in Figure 4-27. A high-speed camera was also used to capture the spray root motion from the bottom of the tank. It provides more information on the spray root interaction with the pressure response.

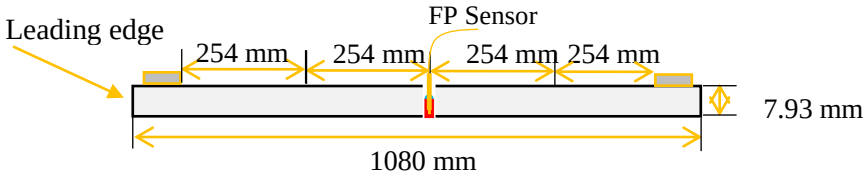

Figure 4-27: Schematic of the experimental setup for dynamic pressure measurements of the flexible plate during water slamming test.

In the following preliminary experiment, a thickness of 7.93mm aluminum plate was used. A single cavity FP pressure with the diaphragm of 2µm was flushed-mounted at the center of the plate as Figure 4-27 shown. The speeds of the W were 17 in/s, 23 in/s, 35 in/s, and 40 in/s in the z-direction. In addition to the pressure measurements, the motion of the spray root was monitored by using a high-speed camera at a frame rate of 800 Hz.

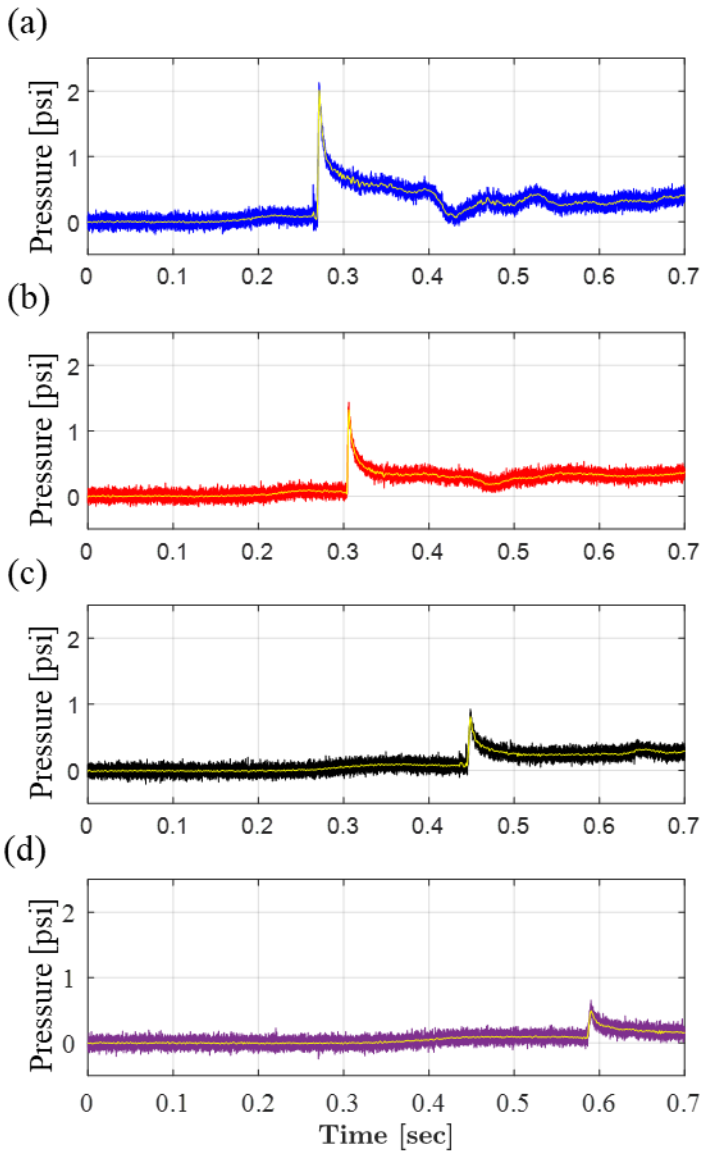

Figure 4-28: Pressure responses of the FP sensor versus time at the speeds of 40 in/s (a), 35 in/s (b), 23 in/s (c) and 17 in/s (d). The smoothed data was labeled in a yellow line.

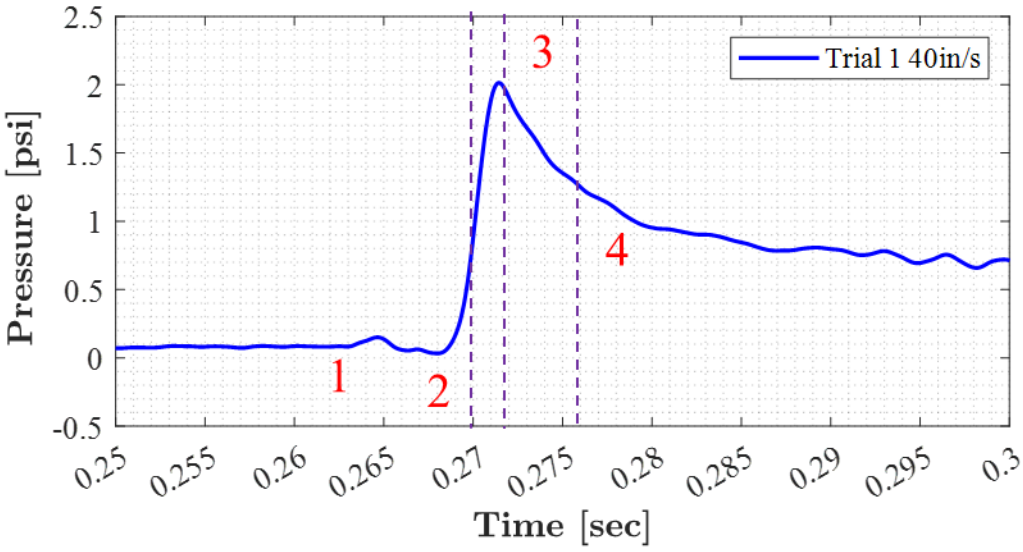

Figure 4-29: Pressure measured by FP pressure sensors flush-mounted on the plate during the vertical impact of the plate on the water surface at W = 40 in/s.

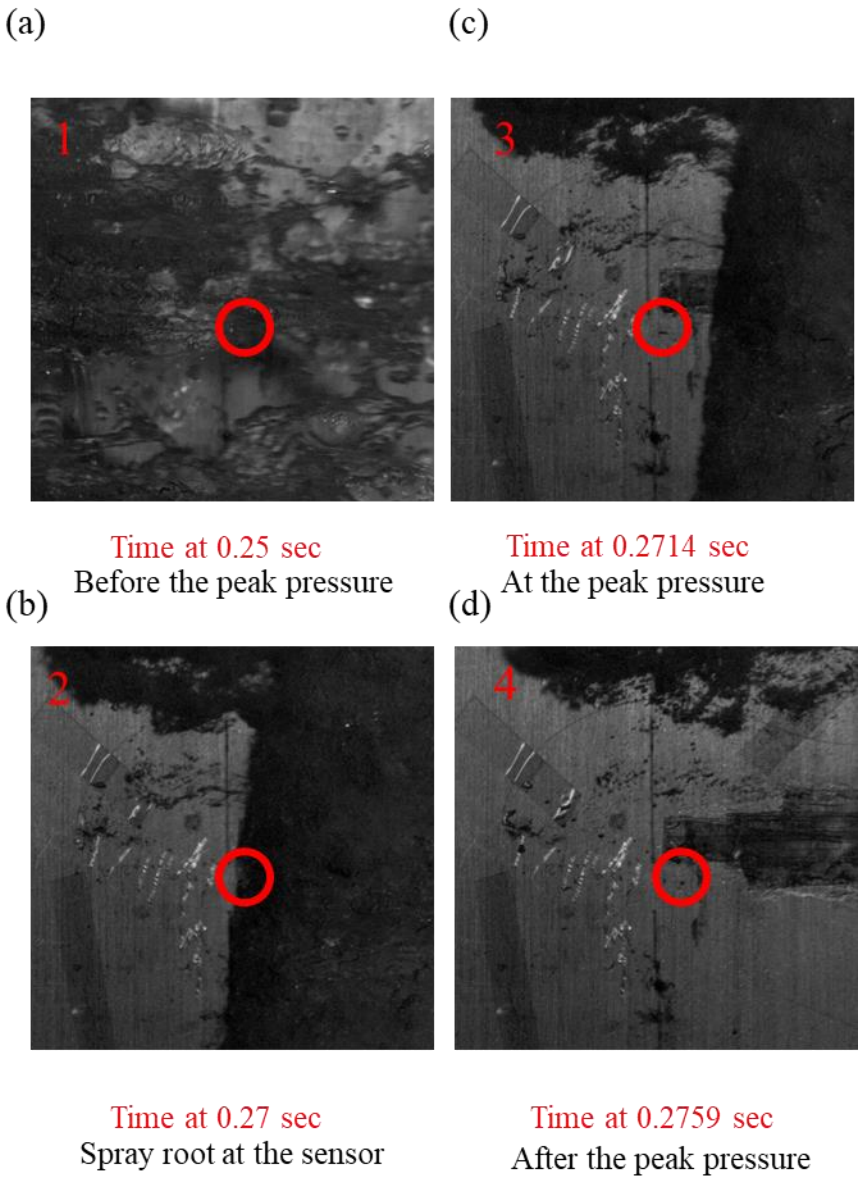

Figure 4-30: (a-d) are the images taken by the high-speed camera at different timing in Figure 4-30.

Figure 4-28 shows the pressure response of the FP pressure sensor from the experiment with four different vertical speeds. The yellow smoothed data will be used for the following discussion. As shown, the value of the pressure peak increased as the W increased from 17 in/s to 40 in/s. The temporal pressure curve exhibited a sharp increase to the peak value followed

by a gradual drop back to zero. This characteristic behavior is similar to other study had been reported[94]. Figure 4-29 shows the close-up pressure response measured by the FP pressure sensor during the vertical impact of the plate on the water surface at W = 40 in/s. Also, Figure 4-31 demonstrated the good repeatability of the experiment. Pressure responses of three slamming experiments are overlapping as Figure 4-31 shown. The high-speed camera captured the spray root motion while the plate entered the water surface as shown in Figure 4-30Figure 4-29(a)-(d). As Figure 4-30(b) shows, the pressure level remained at zero before the spray root passed by. When the spray root overlapped the pressure sensor as Figure 4-30(d) shows, the pressure level increased. The maximum pressure peak occurred at t = 0.2744 sec. At the time, the spray root had passed the pressure sensor as Figure 4-30(c) shows. This result shows the transient pressure peak induced by the spray root and can be used for the hydrodynamic group to investigate the fluid-structure interaction.

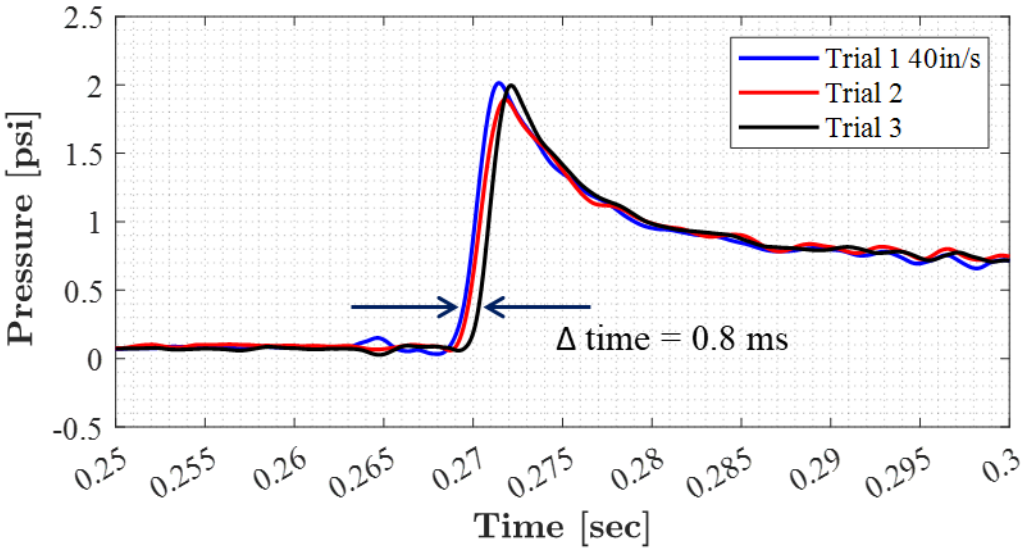

Figure 4-31: Demonstration of the repeatability of the pressure response measured by FP pressure sensors flush-mounted on the plate during the vertical impact of the plate on the water surface at W = 40 in/s.

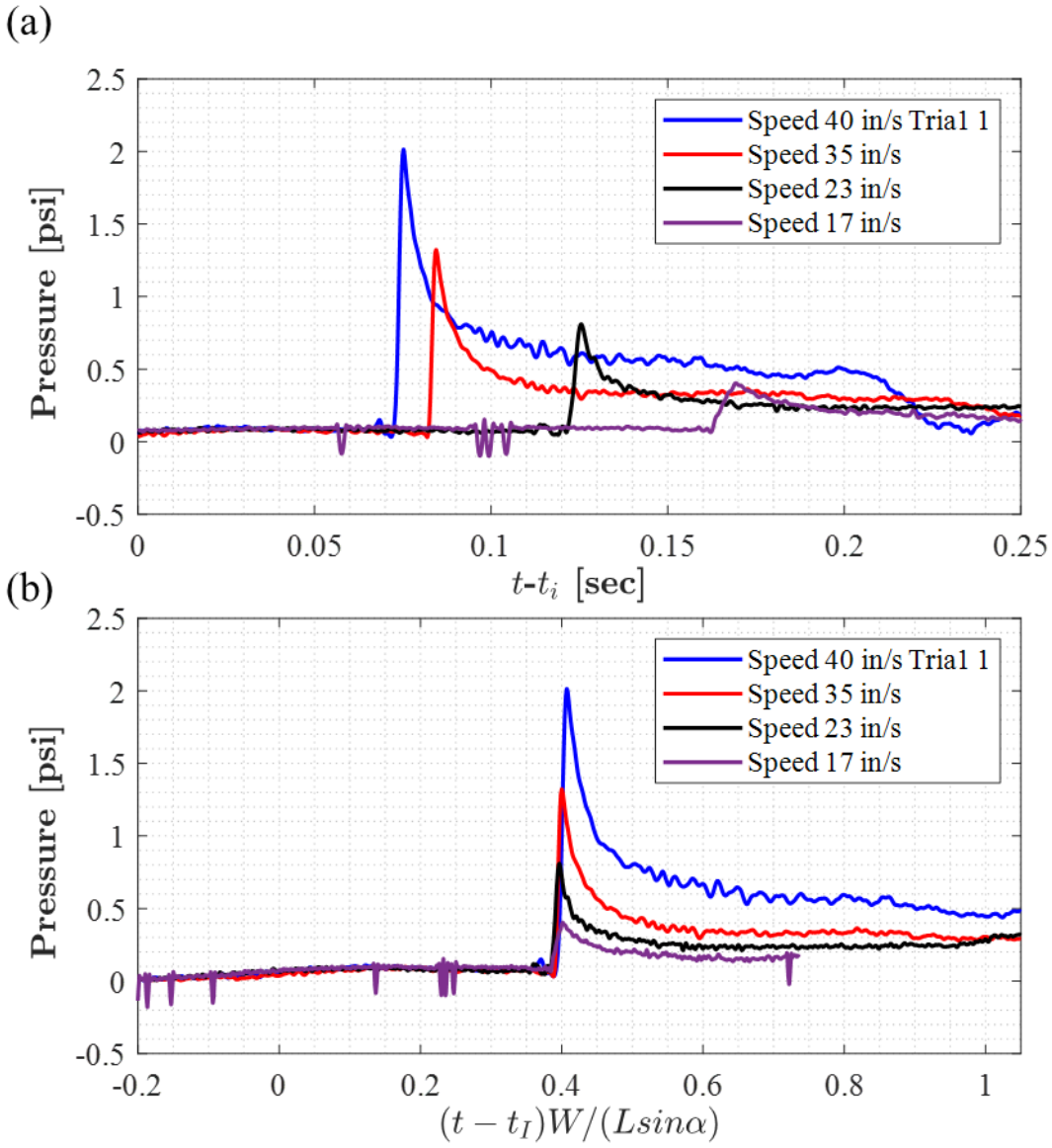

Figure 4-32: Pressure response versus time (a) and dimensionless time (b) measured by the FP pressure sensor during the vertical slamming experiment with W = 17in/s, 23 in/s, 35 in/s, and 40 in/s.

Figure 4-32 shows the pressure response of the vertical slamming with W = 17 in/s, 23 in/s, 35 in/s, and 40 in/s in the time and nondimensional time domain. As the speed increased from 17 in/s to 40 in/s, the time of rising of the shape peak occurred sooner as shown in Figure 4-32(a).

When the pressure response with different W in the nondimensional time domain, the rising time of all the pressure response are the same, tT_S^{-1} = 0.4.

4.5.2 Pressure response of the oblique slamming experiments

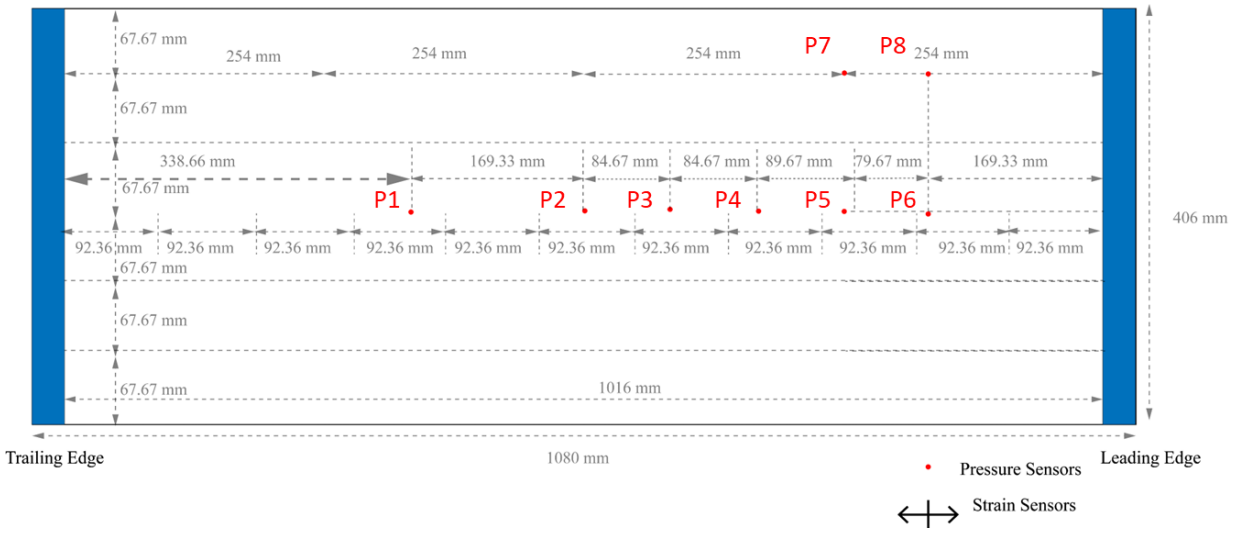

Figure 4-33: The schematic of the distributed 8 FP pressure sensors flushed mounted on the bottom surface of the plate.

In this subsection, the pressure responses of the 2nd slamming experiments are presented to further explore the effect of the pitch angle (α = 7.5°, 10°, and 12.5°). 8 FP pressure sensors were deployed, but only 6 FP pressure sensors were working properly (P4 and P5 are not working). The schematic of the FP sensors layouts is shown in Figures 4-33. Figure 4-34 to Figure 4-39 show the pressure response measured by the FP pressure sensors mounted on the flexible plate (h = 6.35 mm) during the oblique impact of the water under varying slamming conditions.

The pressure response of oblique slamming is similar to the result of the preliminary study, with a sharp increase to the peak value followed by a gradual drop back to zero. The peak pressure occurrence time was influenced by the sensor location. The pressure peak occurred

earlier for the FP pressure sensor close to the trailing edge. Given the location of sensors P6 and P8 are on the same transverse plane, the peak pressure should have the same occurrence time. However, the experiment results show the pressure response of P8 is slightly behind the P6. That can be explained by the shape of the spray root. When the spray root propagated at the leading edge, the shape of the spray root became a U-shape from I-shape.

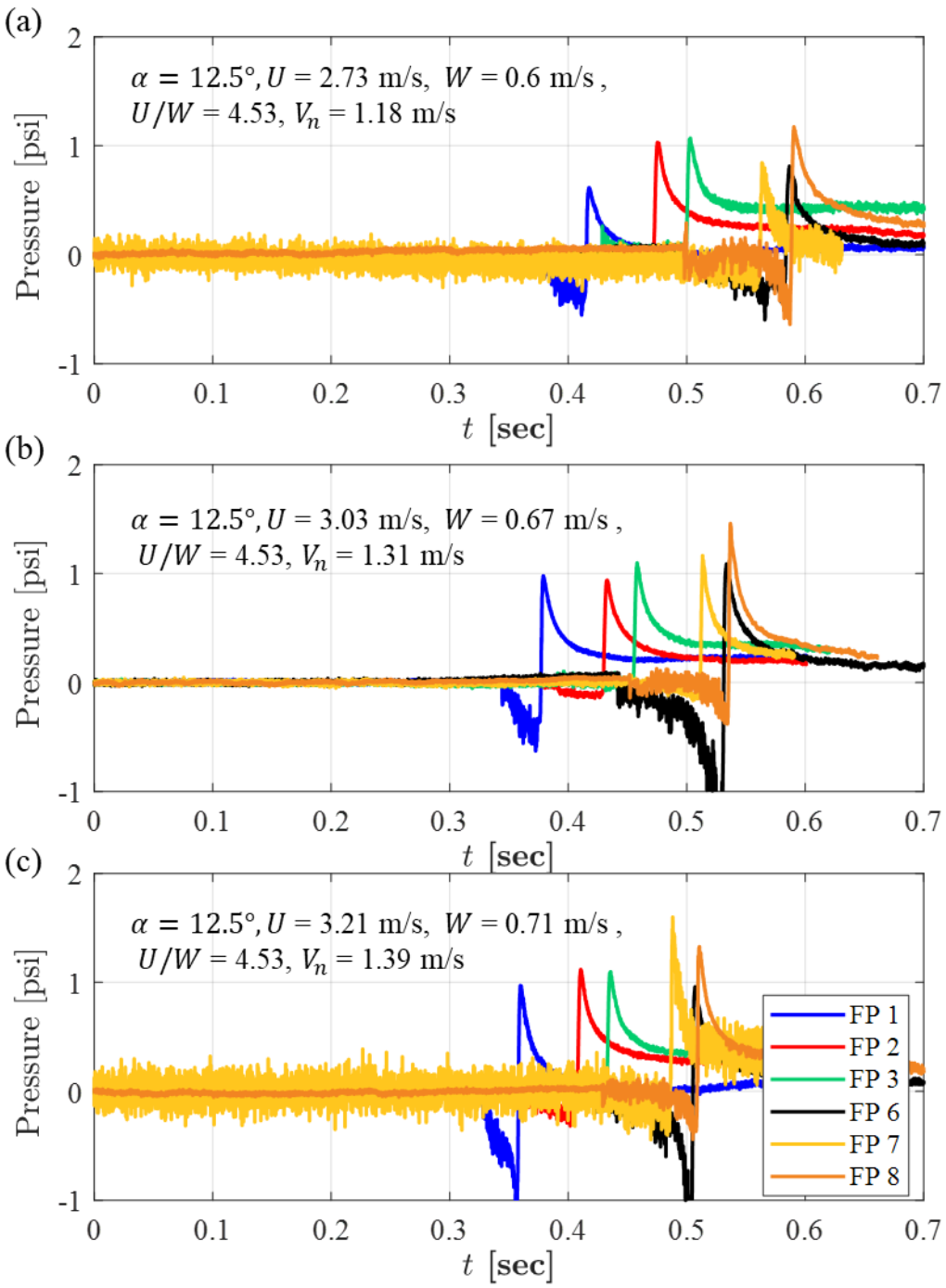

Figure 4-34: Pressure responses of the FP sensors versus time at various V_n of 1.18 m/s (a), 1.31 m/s (b) and 1.39 m/s (c) with U/W = 4.53 and α =12.5°.

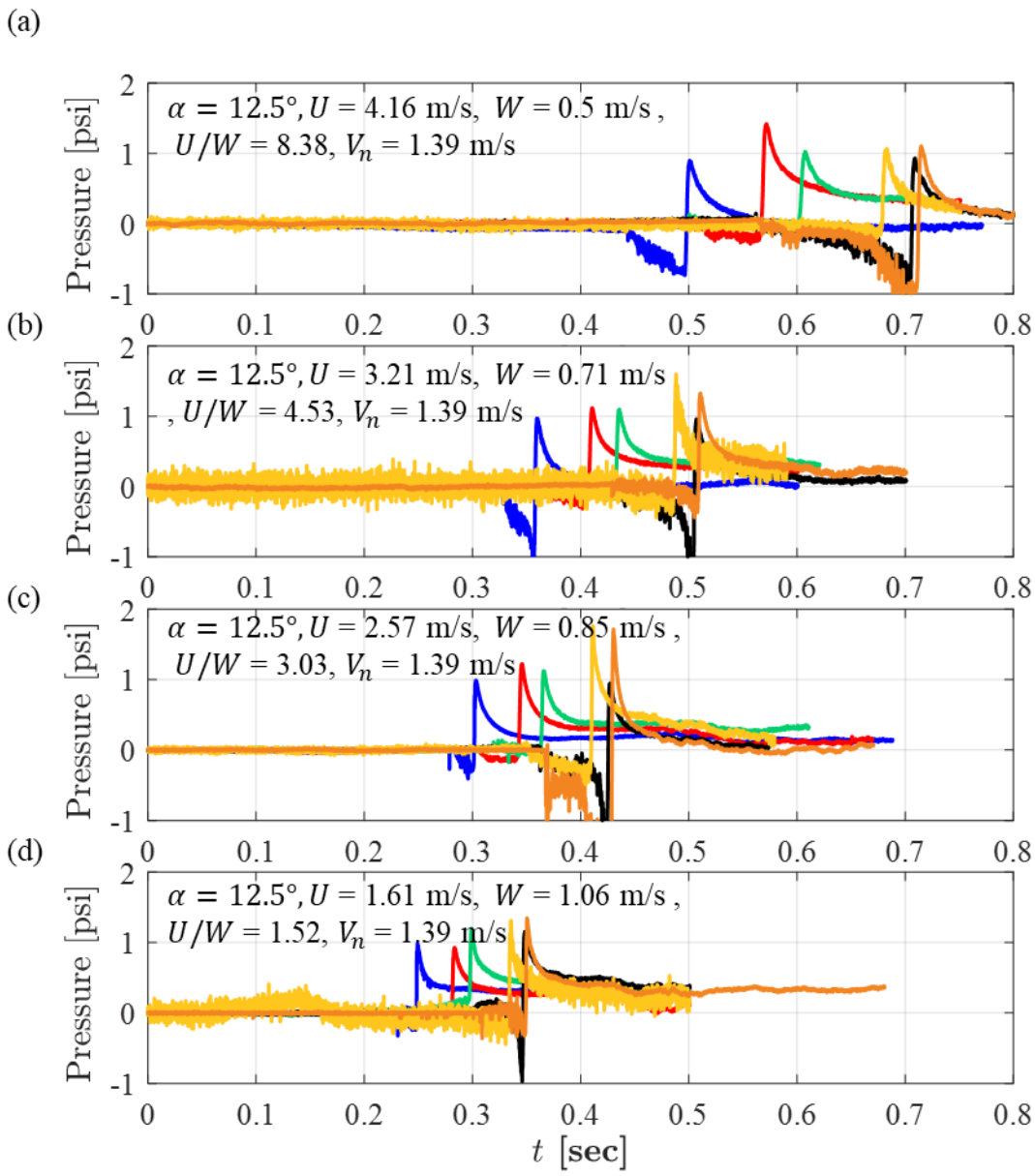

Figure 4-35: Pressure responses of the FP sensors versus time at various U/W of 8.38 (a), 4.53 (b), 3.03 (c), and 1.52 (d) with V_n = 1.39 and α =12.5°

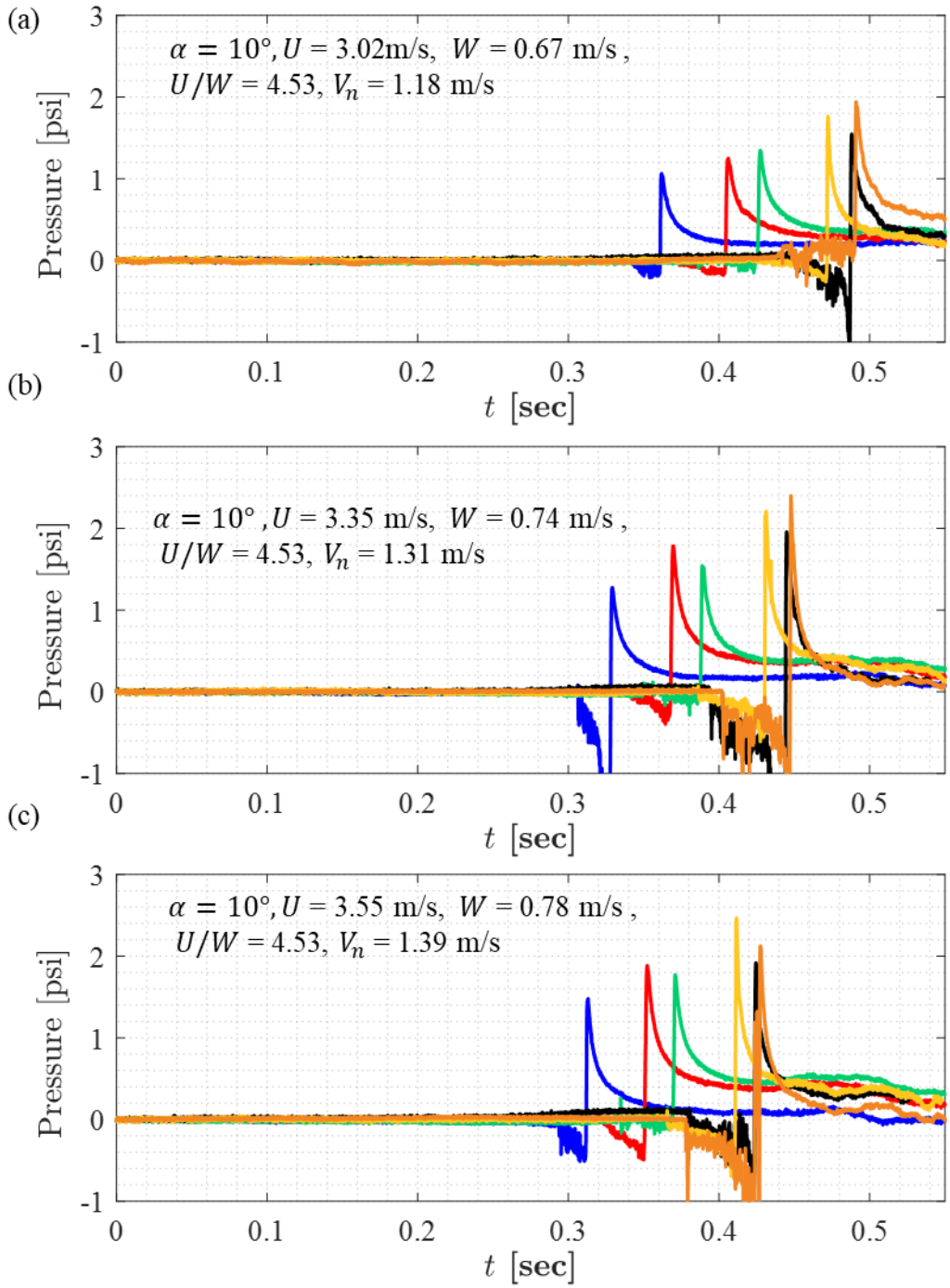

Figure 4-36: Pressure responses of the FP sensors versus time at various V_n of 1.18 m/s (a), 1.31 m/s (b) and 1.39 m/s (c) with U/W = 4.53 and α =10°.

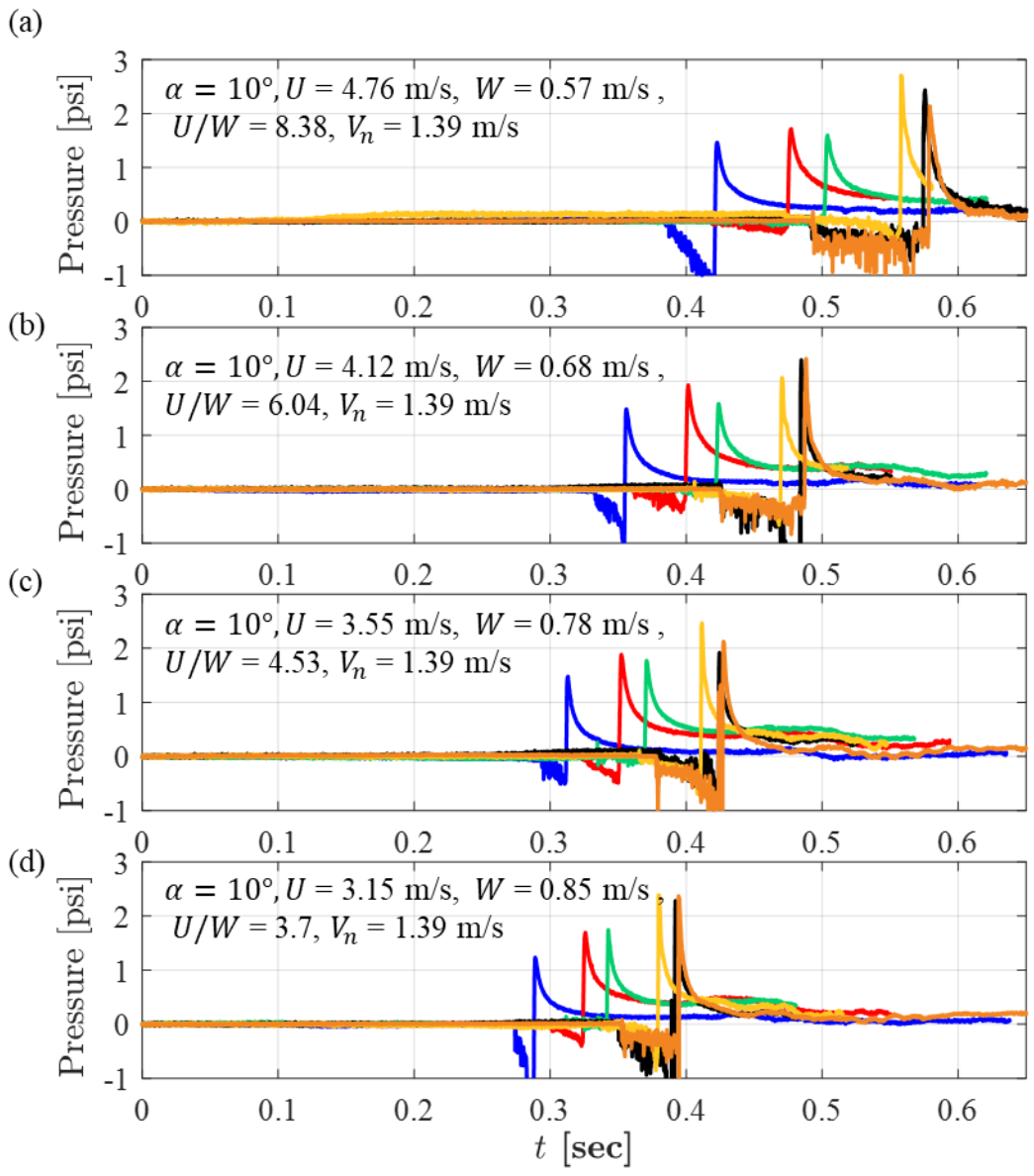

Figure 4-37: Pressure responses of the FP sensors versus time at various U/W of 8.38 (a), 6.04 (b), 4.53 (c), and 3.7 (d) with V_n = 1.39 and α =10°.

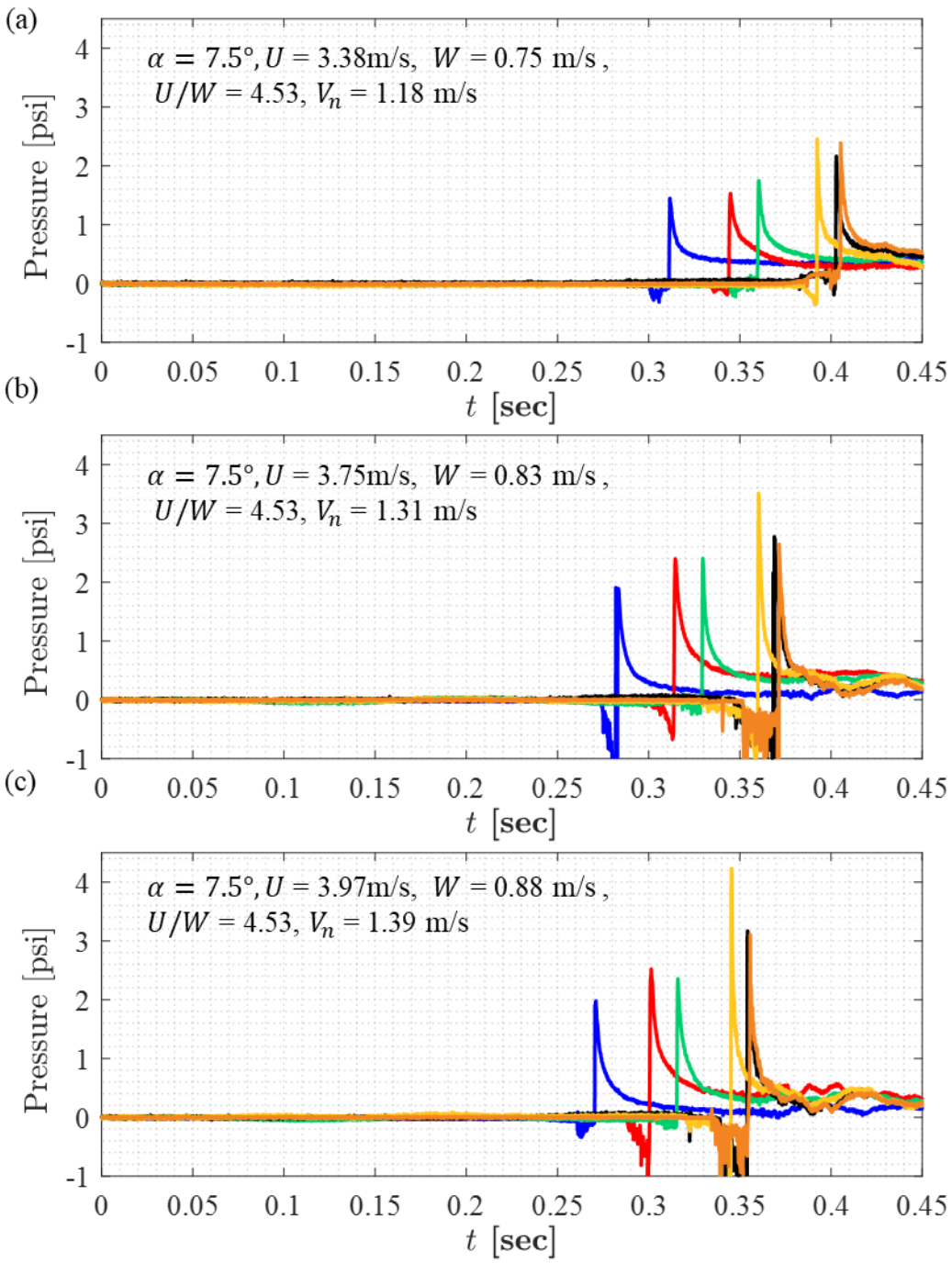

Figure 4-38: Pressure responses of the FP sensors versus time at various V_n with U/W = 4.53 and α =7.5°.

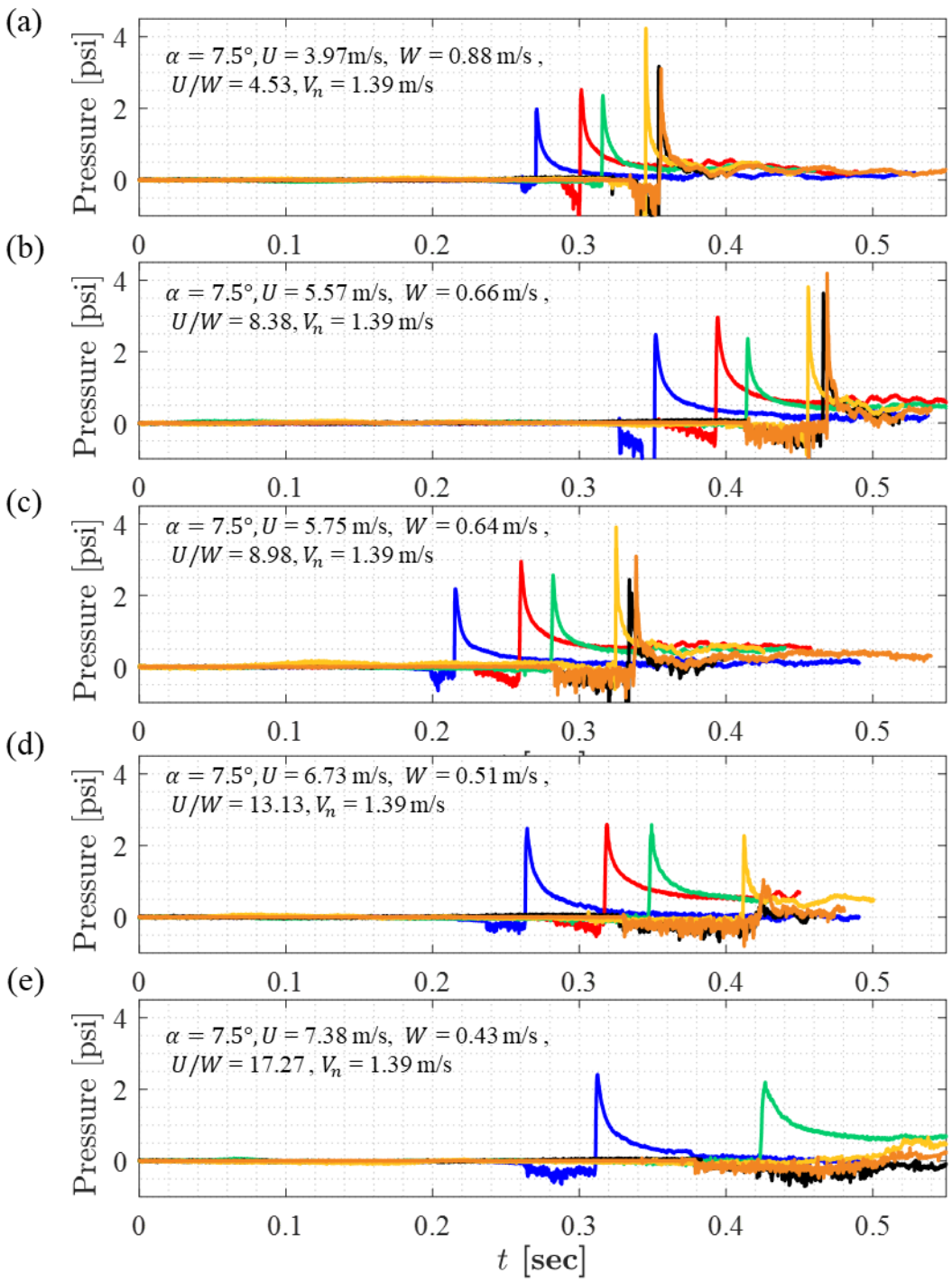

Figure 4-39: Pressure responses of the FP sensors versus time at various U/W of 4.53 (a), 8.38 (b), 8.98 (c), 13.13 (d), and 17.27 (e) with V_n = 1.39 and α =7.5°.

4.6 Summary

With multiplexed FBG strain sensors and FP pressure sensors mounted on the flexible plate, the dynamic strain and pressure responses that occurred on the plate during the slamming event were successfully monitored. Two sets of FBG sensors were deployed in the strain measurements during the slamming experiments. The strain responses showed good agreement with the deflection and spray root measurements as well. The pressure measurements with the FP pressure sensors also showed good agreement with the results obtained with the high-speed camera. Owing to its capability of monitoring distributed, highly transient structural responses and pressure responses, the high-speed fiber optic interrogation system with FBG strain sensors and FP pressure sensors can serve as a useful measurement tool for a better understanding of fluid and structure interaction during slamming events.

5. Summary and future work

5.1 Summary of the dissertation work

A high-speed optical system for interrogation of fiber Bragg grating strain sensors and FP pressure sensors has been developed. Miniature fiber-optic pressure sensors have been investigated. Experimental studies of pressure and strain measurements of the flexible plate during the slamming event have been carried out. This sensing system and pressure sensors can be used for other applications as well.

Through this dissertation work, a high-speed spectral domain interrogation system has been developed for fiber-optic FP interferometric sensors and fiber Bragg grating sensors. This system employs a broadband light source, a piezoelectric FPTF, and an array of FBGs for wavelength referencing to enable fast speed, and wide spectral range interrogation of the FP sensors. By operating the FPTF at its resonance frequency, a 98 nm interrogation range and an FP cavity length resolution of 1.8 nm were realized at an interrogation speed of ~110 kHz. Furthermore, the performance of the proposed high-speed spectral domain interrogation scheme has been investigated with diaphragm-based fiber-tip FP sensors. The pressure measurement results show that the spectral domain interrogation method has the advantages of robustness to light intensity noise and large dynamic range compared with the intensity-based interrogation method. The acoustic measurement results have demonstrated the ability of the high-speed spectral domain interrogation method for the measurement of dynamic parameters as high as 20 kHz. The interrogation system offers a new way of achieving high-speed, large dynamic range fiber-optic FP interferometric sensor systems.

With multiplexed FBG strain sensors mounted on the flexible plate, the dynamic strain responses that occurred on the plate during the slamming event have been successfully

monitored. Owing to its capability of monitoring distributed, highly transient structural responses, the high-speed FBG strain sensor interrogation system can serve as a useful measurement tool for a better understanding of fluid and structure interaction during slamming events.

A tailor-making polymer-diaphragm-based fiber-tip Fabry-Perot pressure sensor has been developed for varying applications such as pressure and acoustic measurements. Owing to its advantage of small size, it makes it possible to measure a high transient pressure response of a flexible plate. Temperature compensation has been successfully implemented to decouple pressure reading from temperature loading. Finally, the pressure sensor has been deployed to measure the pressure response of the oblique slamming on a flexible plate.

Experimental studies of pressure and strain measurements of the flexible plate during the slamming event have been carried out. The high-speed spectral domain interrogation system and fiber-optic pressure and strain sensors enable to the measurement of the strain and pressure response of a flexible plate during the violent motions of the hull and the water free surface. In such studies, monitoring the dynamic structural responses is important for a better understanding of the complex fluid-structure interaction during the slamming event.

The original contributions of the dissertation work can be summarized as follows.

Contribution 1: A high-speed, large dynamic range spectral-domain fiber optic interrogation system is developed, which is capable of demodulation of multiplexed FBG strain sensors and Fabry-Perot pressure sensors.

A high-speed spectral-domain optical interrogation system has been developed, which employs a piezoelectric tunable filter operating at its resonant frequencies to achieve a large

tuning range, high resolution, and high speed. High-speed interrogation of multiplexed FBG and FP sensors has been demonstrated with this system.

Contribution 2: Enhanced understanding of miniature FP pressure sensors based on 3D printing techniques and their temperature compensation has been achieved.

Miniature FP pressure sensors have been designed and fabricated to monitor the dynamic pressure response of a flexible plate slamming onto a water surface. Owings to its small size and immunity to electromagnetic interference, these sensors can be integrated with the flexible plate to carry out the intended experimental studies for understanding fluid-structure interactions during slamming events.

Contribution 3: Distributed strain and pressure measurements of a flexible plate slamming on a water surface have been carried out with fiber-optic sensors for the first time.

The distributed fiber-optic strain and pressure sensor system have been integrated with a flexible plate and used for monitoring the dynamic strain and pressure response during the slamming experiments. The highly transient strain and pressure responses during the slamming event have been successfully measured by the high-speed spectral-domain interrogation system with the fiber-optic sensors.

5.2 Future Work

As an extension of this dissertation work, future work is recommended as follows.

1. Investigate the reliability of the polymer-based FP pressure sensors.

The polymer degradation is one of the known problems for any polymer-based sensors. The degradation reduces the physical properties of the polymer, such as strength. The change of

the strength of the polymer would affect the calibrated pressure sensitivity. However, this issue has not been addressed in this dissertation since a new patch of sensors is made upon required. The lifetime of the sensor is usually less than 3-6 months and the sensor performance changes over time due to the degradation of the polymer. Therefore, investigations into the polymer degradation and methods of improving the reliability of the pressure sensor should be performed in the future work.

2. Design a metamaterial-based pressure sensor with thermal insulation

Currently, the temperature compensation is achieved by super-positioning the different sensitivities. To fully take advantage of the 3D printing technique using the Nanoscribe, a more sophisticated structure of the pressure sensor can be fabricated. Metamaterials are defined as artificially designed materials with unusual physical properties such as thermal expansion. Future work is suggested to develop a thermal metamaterial as the sensing structure. This will enable the design of a pressure sensor with an extremely low thermal expansion coefficient while maintaining a good pressure sensitivity.

References:

[1] I. García, J. Zubia, G. Durana, G. Aldabaldetreku, M. A. Illarramendi, and J. Villatoro, "Optical fiber sensors for aircraft structural health monitoring," *Sensors (Switzerland)*. 2015. doi: 10.3390/s150715494.

[2] M. J. Nicolas, R. W. Sullivan, and W. L. Richards, "Large scale applications using FBG sensors: Determination of in-flight loads and shape of a composite aircraft wing," *Aerospace*, vol. 3, no. 3, 2016, doi: 10.3390/aerospace3030018.

[3] Z. Gao, X. Zhu, Y. Fang, and H. Zhang, "Active monitoring and vibration control of smart structure aircraft based on FBG sensors and PZT actuators," *Aerosp. Sci. Technol.*, vol. 63, 2017, doi: 10.1016/j.ast.2016.12.027.

[4] A. Iadicicco, D. Natale, P. Di Palma, F. Spinaci, A. Apicella, and S. Campopiano, "Strain monitoring of a composite drag strut in aircraft landing gear by fiber bragg grating sensors," *Sensors (Switzerland)*, vol. 19, no. 10, 2019, doi: 10.3390/s19102239.

[5] X. Ye, Y. Ni, and J. Yin, "Safety monitoring of railway tunnel construction using FBG sensing technology," *Adv. Struct. Eng.*, 2013, doi: 10.1260/1369-4332.16.8.1401.

[6] Q. Nan *et al.*, "A novel monitoring approach for train tracking and incursion detection in underground structures based on ultra-weak FBG sensing array," *Sensors (Switzerland)*, 2019, doi: 10.3390/s19122666.

[7] D. Kang, D. H. Kim, and S. Jang, "Design and development of structural health monitoring system for smart railroad-gauge-facility using FBG sensors," *Exp. Tech.*, vol. 38, no. 5, 2014, doi: 10.1111/j.1747-1567.2012.00844.x.

[8] A. Catalano, F. A. Bruno, M. Pisco, A. Cutolo, and A. Cusano, "Intrusion detection system for the protection of railway assets by using Fiber Bragg Grating sensors: A Case Study," 2014. doi: 10.1109/MePhoCo.2014.6866483.

[9] H. H. Zhu, J. H. Yin, L. Zhang, W. Jin, and J. H. Dong, "Monitoring internal displacements of a model dam using FBG sensing bars," *Adv. Struct. Eng.*, 2010, doi: 10.1260/1369-4332.13.2.249.

[10] L. Ren, J. Chen, H. N. Li, G. Song, and X. Ji, "Design and application of a fiber Bragg grating strain sensor with enhanced sensitivity in the small-scale dam model," *Smart Mater. Struct.*, vol. 18, no. 3, 2009, doi: 10.1088/0964-1726/18/3/035015.

[11] H. Zhu, J. Yin, L. Zhang, J. Dong, K. Fung, and W. Jin, "Deformation monitoring of dam model test by optical fiber sensors," *Yanshilixue Yu Gongcheng Xuebao/Chinese J. Rock Mech. Eng.*, vol. 27, no. 6, 2008.

[12] H. H. Zhu, J. H. Yin, J. H. Dong, and L. Zhang, "Physical modelling of sliding failure of concrete gravity dam under overloading condition," *Geomech. Eng.*, vol. 2, no. 2, 2010, doi: 10.12989/gae.2010.2.2.089.

[13] C. Rodrigues, F. Cavadas, C. Félix, and J. Figueiras, "FBG based strain monitoring in the rehabilitation of a centenary metallic bridge," *Eng. Struct.*, 2012, doi: 10.1016/j.engstruct.2012.05.040.

[14] X. W. Ye, Y. H. Su, and P. Sen Xi, “Statistical analysis of stress signals from bridge monitoring by FBG system,” *Sensors (Switzerland)*, vol. 18, no. 2, 2018, doi: 10.3390/s18020491.

[15] F. Xiao, G. S. Chen, and J. Leroy Hulsey, “Monitoring bridge dynamic responses using fiber bragg grating tiltmeters,” *Sensors (Switzerland)*, vol. 17, no. 10, 2017, doi: 10.3390/s17102390.

[16] X. X. Li, W. X. Ren, and K. M. Bi, “FBG force-testing ring for bridge cable force monitoring and temperature compensation,” *Sensors Actuators, A Phys.*, vol. 223, 2015, doi: 10.1016/j.sna.2015.01.003.

[17] C. Rodrigues, C. Félix, A. Lage, and J. Figueiras, “Development of a long-term monitoring system based on FBG sensors applied to concrete bridges,” *Eng. Struct.*, vol. 32, no. 8, 2010, doi: 10.1016/j.engstruct.2010.02.033.

[18] F. Guo, T. Fink, M. Han, L. Koester, J. Turner, and J. Huang, “High-sensitivity, high-frequency extrinsic Fabry–Perot interferometric fiber-tip sensor based on a thin silver diaphragm,” *Opt. Lett.*, 2012, doi: 10.1364/ol.37.001505.

[19] S. Jinachandran and G. Rajan, “Fibre bragg grating based acoustic emission measurement system for structural health monitoring applications,” *Materials (Basel).*, vol. 14, no. 4, 2021, doi: 10.3390/ma14040897.

[20] C. Li, L. Sun, Z. Xu, X. Wu, T. Liang, and W. Shi, “Experimental Investigation and Error Analysis of High Precision FBG Displacement Sensor for Structural Health Monitoring,” *Int. J. Struct. Stab. Dyn.*, vol. 20, no. 6, 2020, doi: 10.1142/S0219455420400118.

[21] B. Torres, I. Payá-Zaforteza Ignacio, P. A. Calderón, and J. M. Adam, “Analysis of the strain transfer in a new FBG sensor for Structural Health Monitoring,” *Eng. Struct.*, vol. 33, no. 2, 2011, doi: 10.1016/j.engstruct.2010.11.012.

[22] T. H. T. Chan *et al.*, “Fiber Bragg grating sensors for structural health monitoring of Tsing Ma bridge: Background and experimental observation,” *Eng. Struct.*, 2006, doi: 10.1016/j.engstruct.2005.09.018.

[23] S. Poeggel, D. Tosi, G. Leen, and E. Lewis, “Low-cost miniature fiber optic extrinsic fabry-perot interferometric sensor for cardiovascular pressure measurement,” 2013. doi: 10.1109/CLEOE-IQEC.2013.6801216.

[24] T. Tsukioka *et al.*, “An on-site preparable, novel bone-grafting complex consisting of human platelet-rich fibrin and porous particles made of a recombinant collagen-like protein,” *J. Biomed. Mater. Res. - Part B Appl. Biomater.*, vol. 107, no. 5, 2019, doi: 10.1002/jbm.b.34234.

[25] G. T. Kanellos, G. Papaioannou, D. Tsiokos, C. Mitrogiannis, G. Nianios, and N. Pleros, “Two dimensional polymer-embedded quasi-distributed FBG pressure sensor for biomedical applications,” *Opt. Express*, vol. 18, no. 1, 2010, doi: 10.1364/oe.18.000179.

[26] H. Qiu, F. Min, S. Zhong, X. Song, and Y. Yang, “Hypersonic force measurements using internal balance based on optical micromachined Fabry-Perot interferometry,” *Rev. Sci. Instrum.*, 2018, doi: 10.1063/1.5017310.

[27] Z. Ma and X. Chen, “Fiber bragg gratings sensors for aircraft wing shape measurement: Recent applications and technical analysis,” *Sensors (Switzerland)*, vol. 19, no. 1, 2019, doi: 10.3390/s19010055.

[28] Q. Dong *et al.*, “Miniature Fiber Optic Acoustic Pressure Sensors with Air-Backed Graphene Diaphragms,” *J. Vib. Acoust. Trans. ASME*, 2019, doi: 10.1115/1.4042929.

[29] T. Fu, P. Wei, X. Han, and Q. Liu, “Application of fiber bragg grating acoustic emission sensors in thin polymer-bonded explosives,” *Sensors (Switzerland)*, vol. 18, no. 11, 2018, doi: 10.3390/s18113778.

[30] C. Li, X. Peng, H. Zhang, C. Wang, S. Fan, and S. Cao, “A sensitivity-enhanced flexible acoustic sensor using side-polished fiber Bragg grating,” *Meas. J. Int. Meas. Confed.*, vol. 117, 2018, doi: 10.1016/j.measurement.2017.12.027.

[31] C. Wang, G. Yan, Z. Lian, X. Chen, S. Wu, and S. He, “Hybrid-cavity fabry-perot interferometer for multi-point relative humidity and temperature sensing,” *Sensors Actuators, B Chem.*, 2018, doi: 10.1016/j.snb.2017.08.224.

[32] K. Chen *et al.*, “Simultaneous measurement of acoustic pressure and temperature using a Fabry-Perot interferometric fiber-optic cantilever sensor,” *Opt. Express*, 2020, doi: 10.1364/oe.387195.

[33] Z. Li, J. Tian, Y. Jiao, Y. Sun, and Y. Yao, “Simultaneous measurement of air pressure and temperature using fiber-optic cascaded Fabry-Perot interferometer,” *IEEE Photonics J.*, 2019, doi: 10.1109/JPHOT.2018.2884776.

[34] K. Chen *et al.*, “Fast demodulated white-light interferometry-based fiber-optic Fabry–Perot cantilever microphone,” *Opt. Lett.*, 2018, doi: 10.1364/ol.43.003417.

[35] K. Liu *et al.*, “Investigation of PZT driven tunable optical filter nonlinearity using FBG optical fiber sensing system,” *Opt. Commun.*, 2008, doi: 10.1016/j.optcom.2008.02.034.

[36] C. Y. Park, B. W. Jang, J. H. Kim, C. G. Kim, and S. M. Jun, “Bird strike event monitoring in a composite UAV wing using high speed optical fiber sensing system,” *Compos. Sci. Technol.*, 2012, doi: 10.1016/j.compscitech.2011.12.008.

[37] J. L. Stay, D. Carr, S. Ferguson, T. Haber, R. Jenkins, and J. Mock, “Dependence on fiber Fabry-Pérot tunable filter characteristics in an all-fiber swept-wavelength laser for use in an optical coherence tomography system,” 2017. doi: 10.1117/12.2252949.

[38] T. Vella *et al.*, “Full-spectrum interrogation of fiber bragg gratings at 100 kHz for detection of impact loading,” *Meas. Sci. Technol.*, 2010, doi: 10.1088/0957-0233/21/9/094009.

[39] A. Propst *et al.*, “Assessment of damage in composite laminates through dynamic, full-spectral interrogation of fiber bragg grating sensors,” *Smart Mater. Struct.*, 2010, doi: 10.1088/0964-1726/19/1/015016.

[40] W. R. Allan, Z. W. Graham, J. R. Zayas, D. P. Roach, and D. A. Horsley, “Multiplexed fiber bragg grating interrogation system using a microelectromechanical fabryperot tunable filter,” *IEEE Sens. J.*, 2009, doi: 10.1109/JSEN.2009.2024849.

[41] H.-T. Kim and M. Yu, “High-speed optical sensor interrogator with a silicon-ring-resonator-based thermally tunable filter,” *Opt. Lett.*, 2017, doi: 10.1364/ol.42.001305.

[42] H. T. Kim and M. Yu, “Thermally-tunable-silicon-ring-resonator-based high-speed optical sensor interrogator for impact monitoring,” 2017. doi: 10.1364/FIO.2017.FTh3A.5.

[43] D. Kinet, P. Mégret, K. W. Goossen, L. Qiu, D. Heider, and C. Caucheteur, “Fiber Bragg grating sensors toward structural health monitoring in composite materials: Challenges and solutions,” *Sensors (Switzerland)*. 2014. doi: 10.3390/s140407394.

[44] J. Frieden, J. Cugnoni, J. Botsis, T. Gmür, and D. Ćorić, “High-speed internal strain measurements in composite structures under dynamic load using embedded FBG sensors,” *Compos. Struct.*, 2010, doi: 10.1016/j.compstruct.2010.01.007.

[45] J. Leng and A. Asundi, “Structural health monitoring of smart composite materials by using EFPI and FBG sensors,” *Sensors Actuators, A Phys.*, 2003, doi: 10.1016/S0924-4247(02)00429-6.

[46] U. Nawrot *et al.*, “Development of a mechanical strain amplifying transducer with Bragg grating sensor for low-amplitude strain sensing,” *Smart Mater. Struct.*, vol. 26, no. 7, 2017, doi: 10.1088/1361-665X/aa746c.

[47] P. Moyo, J. M. W. Brownjohn, R. Suresh, and S. C. Tjin, “Development of fiber Bragg grating sensors for monitoring civil infrastructure,” *Eng. Struct.*, vol. 27, no. 12 SPEC. ISS., 2005, doi: 10.1016/j.engstruct.2005.04.023.

[48] M. Liang, X. Fang, and Y. Ning, “Temperature Compensation Fiber Bragg Grating Pressure Sensor Based on Plane Diaphragm,” *Photonic Sensors*, vol. 8, no. 2, 2018, doi: 10.1007/s13320-018-0417-9.

[49] Y. C. Manie *et al.*, “Intensity and wavelength division multiplexing FBG sensor system using a Raman amplifier and extreme learning machine,” *J. Sensors*, vol. 2018, 2018, doi: 10.1155/2018/7323149.

[50] Y. Qiu, Q. B. Wang, H. T. Zhao, J. A. Chen, and Y. Y. Wang, “Review on composite structural health monitoring based on fiber Bragg grating sensing principle,” *J. Shanghai Jiaotong Univ.*, vol. 18, no. 2, 2013, doi: 10.1007/s12204-013-1375-4.

[51] Z. fang Wang, J. Wang, Q. mei Sui, S. cai Li, and L. Jia, “In-situ calibrated deformation reconstruction method for fiber Bragg grating embedded smart Geogrid,” *Sensors Actuators, A Phys.*, vol. 250, 2016, doi: 10.1016/j.sna.2016.09.027.

[52] B. Zhang and M. Kahrizi, “High-temperature resistance Fiber Bragg grating temperature sensor fabrication,” *IEEE Sens. J.*, 2007, doi: 10.1109/JSEN.2007.891941.

[53] Y. J. Ee, K. S. Tey, K. S. Lim, P. Shrivastava, S. B. R. S. Adnan, and H. Ahmad, “Lithium-Ion Battery State of Charge (SoC) Estimation with Non-Electrical parameter using Uniform Fiber Bragg Grating (FBG),” *J. Energy Storage*, vol. 40, 2021, doi: 10.1016/j.est.2021.102704.

[54] Y. Liu, M. Fisser, J. Fang, Z. Jiang, R. Mataira, and R. A. Badcock, “Feasibility Study of Fiber Bragg Grating Sensor for Quench Detection of High Temperature

Superconductors," *IEEE Trans. Appl. Supercond.*, vol. 29, no. 5, 2019, doi: 10.1109/TASC.2019.2909539.

[55] F. Yu and Y. Okabe, "Fiber-optic sensor-based remote acoustic emission measurement in a 1000 °C environment," *Sensors (Switzerland)*, vol. 17, no. 12, 2017, doi: 10.3390/s17122908.

[56] Z. Shao *et al.*, "Excellent repeatability, all-sapphire Fabry Perot optical Pressure sensor based on wet etching and direct bonding for Harsh Environment Applications," *Opt. Express*, 2021, doi: 10.1364/oe.423753.

[57] M. Li, M. Wang, and H. Li, "Optical MEMS pressure sensor based on Fabry-Perot interferometry," *Opt. Express*, 2006, doi: 10.1364/oe.14.001497.

[58] H. Gao, Y. Jiang, Y. Cui, L. Zhang, J. Jia, and J. Hu, "Dual-Cavity Fabry-Perot Interferometric Sensors for the Simultaneous Measurement of High Temperature and High Pressure," *IEEE Sens. J.*, 2018, doi: 10.1109/JSEN.2018.2875435.

[59] J. Luo *et al.*, "Fiber optic hydrogen sensor based on a Fabry-Perot interferometer with a fiber Bragg grating and a nanofilm," *Lab Chip*, 2021, doi: 10.1039/d1lc00012h.

[60] D. Chen *et al.*, "An in-line fiber optic fabry-perot sensor for high-temperature vibration measurement," *Micromachines*, vol. 11, no. 3, 2020, doi: 10.3390/mi11030252.

[61] X. Zhang, W. Wang, H. Chen, Y. Tang, Z. Ma, and K. Wang, "Two-parameter elliptical fitting method for short-cavity fiber fabry–perot sensor interrogation," *Sensors (Switzerland)*, vol. 19, no. 1, 2019, doi: 10.3390/s19010036.

[62] X. Liu *et al.*, "A compact fiber optic fabry-perot sensor for simultaneous measurement of acoustic and temperature," *IEEE Photonics J.*, vol. 11, no. 6, 2019, doi: 10.1109/JPHOT.2019.2948045.

[63] C. Pang, H. Bae, A. Gupta, K. Bryden, and M. Yu, "MEMS Fabry-Perot sensor interrogated by optical system-on-a-chip for simultaneous pressure and temperature sensing," *Opt. Express*, 2013, doi: 10.1364/oe.21.021829.

[64] R. S. Tucker, D. M. Baney, W. V. Sorin, and C. A. Flory, "Thermal noise and radiation pressure in MEMS Fabry-Pérot tunable filters and lasers," *IEEE J. Sel. Top. Quantum Electron.*, vol. 8, no. 1, 2002, doi: 10.1109/2944.991403.

[65] T. Kääriäinen, P. Jaanson, A. Vaigu, R. Mannila, and A. Manninen, "Active hyperspectral sensor based on MEMS fabry-pérot interferometer," *Sensors (Switzerland)*, vol. 19, no. 9, 2019, doi: 10.3390/s19092192.

[66] M. Zhao, K. Jiang, H. Bai, H. Wang, and X. Wei, "A MEMS based Fabry–Pérot accelerometer with high resolution," *Microsyst. Technol.*, vol. 26, no. 6, 2020, doi: 10.1007/s00542-020-04747-3.

[67] G. C. Hill *et al.*, "SU-8 MEMS Fabry-Perot pressure sensor," *Sensors Actuators, A Phys.*, vol. 138, no. 1, 2007, doi: 10.1016/j.sna.2007.04.047.

[68] J. Liu *et al.*, "MgO Single Crystals MEMS-Based Fiber-Optic Fabry-Perot Pressure

Sensor for Harsh Monitoring," *IEEE Sens. J.*, vol. 21, no. 4, 2021, doi: 10.1109/JSEN.2020.3029152.

[69] Y. S. Kim, N. G. Dagalakis, and Y. M. Choi, "Optical fiber Fabry-Pérot micro-displacement sensor for MEMS in-plane motion stage," *Microelectron. Eng.*, vol. 187–188, 2018, doi: 10.1016/j.mee.2017.11.010.

[70] H. Mao *et al.*, "Large-Area MEMS Tunable Fabry-Perot Filters for Multi/Hyperspectral Infrared Imaging," *IEEE J. Sel. Top. Quantum Electron.*, vol. 23, no. 2, 2017, doi: 10.1109/JSTQE.2016.2643782.

[71] C. R. Liao, T. Y. Hu, and D. N. Wang, "Optical fiber Fabry-Perot interferometer cavity fabricated by femtosecond laser micromachining and fusion splicing for refractive index sensing," *Opt. Express*, 2012, doi: 10.1364/oe.20.022813.

[72] D. Duan, Y. Rao, and T. Zhu, "High sensitivity gas refractometer based on all-fiber open-cavity Fabry–Perot interferometer formed by large lateral offset splicing," *J. Opt. Soc. Am. B*, vol. 29, no. 5, 2012, doi: 10.1364/josab.29.000912.

[73] J. li Zhu, M. Wang, C. di Yang, and T. ting Wang, "Miniature fiber Fabry-Perot sensors based on fusion splicing," *Optoelectron. Lett.*, vol. 9, no. 2, 2013, doi: 10.1007/s11801-013-2432-9.

[74] R. Flores, R. Janeiro, and J. Viegas, "Optical fibre Fabry-Pérot interferometer based on inline microcavities for salinity and temperature sensing," *Sci. Rep.*, vol. 9, no. 1, 2019, doi: 10.1038/s41598-019-45909-2.

[75] H. Yu, Z. Luo, Y. Zheng, J. Ma, Z. Li, and X. Jiang, "Temperature-Insensitive Vibration Sensor with Kagomé Hollow-Core Fiber Based Fabry-Perot Interferometer," *J. Light. Technol.*, vol. 37, no. 10, 2019, doi: 10.1109/JLT.2019.2901845.

[76] H. Wei, M. Chen, and S. Krishnaswamy, "Three-dimensional-printed Fabry–Perot interferometer on an optical fiber tip for a gas pressure sensor," *Appl. Opt.*, 2020, doi: 10.1364/ao.385573.

[77] H. Liang *et al.*, "Diaphragm-free fiber-optic fabry-perot interferometric gas pressure sensor for high temperature application," *Sensors (Switzerland)*, vol. 18, no. 4, 2018, doi: 10.3390/s18041011.

[78] P. Chen, Y. Dai, D. Zhang, X. Wen, and M. Yang, "Cascaded-cavity fabry-perot interferometric gas pressure sensor based on vernier effect," *Sensors*, vol. 18, no. 11, 2018, doi: 10.3390/S18113677.

[79] H. Gao *et al.*, "Antiresonant mechanism based self-temperature-calibrated fiber optic Fabry–Perot gas pressure sensors," *Opt. Express*, vol. 27, no. 16, 2019, doi: 10.1364/oe.27.022181.

[80] Z. Li *et al.*, "High-Sensitivity Gas Pressure Fabry-Perot Fiber Probe with Micro-Channel Based on Vernier Effect," *J. Light. Technol.*, vol. 37, no. 14, 2019, doi: 10.1109/JLT.2019.2917062.

[81] S. Liu *et al.*, "Nano silica diaphragm in-fiber cavity for gas pressure measurement," *Sci.*

Rep., vol. 7, no. 1, 2017, doi: 10.1038/s41598-017-00931-0.

[82] X. Hao, Y. Jiang, H. Takao, K. Maenaka, and K. Higuchi, "An annular mechanical temperature compensation structure for gas-sealed capacitive pressure sensor," *Sensors (Switzerland)*, 2012, doi: 10.3390/s120608026.

[83] H. Bae and M. Yu, "Miniature Fabry-Perot pressure sensor created by using UV-molding process with an optical fiber based mold," *Opt. Express*, 2012, doi: 10.1364/oe.20.014573.

[84] H. W. Lee, H. J. Park, J. H. Lee, and M. Song, "Accuracy improvement in peak positioning of spectrally distorted fiber Bragg grating sensors by Gaussian curve fitting," *Appl. Opt.*, 2007, doi: 10.1364/AO.46.002205.

[85] B. Qi, "Novel data processing techniques for dispersive white light interferometer," *Opt. Eng.*, 2003, doi: 10.1117/1.1613958.

[86] Y. Ge, M. Wang, and H. Yan, "Optical MEMS pressure sensor based on a mesa-diaphragm structure," *Opt. Express*, vol. 16, no. 26, 2008, doi: 10.1364/oe.16.021746.

[87] A. Wang, H. T. Kim, K. P. Wong, M. Yu, K. T. Kiger, and J. H. Duncan, "Spray formation and structural deformation during the oblique impact of a flexible plate on a quiescent water surface," *J. Sh. Res.*, 2019, doi: 10.5957/JOSR.10180093.

[88] A. Iafrati, "Experimental investigation of the water entry of a rectangular plate at high horizontal velocity," *J. Fluid Mech.*, 2016, doi: 10.1017/jfm.2016.374.

[89] A. Wang, C. M. Ikeda-Gilbert, J. H. Duncan, D. P. Lathrop, M. J. Cooker, and A. M. Fullerton, "The impact of a deep-water plunging breaker on a wall with its bottom edge close to the mean water surface," *J. Fluid Mech.*, 2018, doi: 10.1017/jfm.2018.109.

[90] X. Zou *et al.*, "Ultrafast Fabry-Perot fiber-optic pressure sensors for multimedia blast event measurements," *Appl. Opt.*, 2013, doi: 10.1364/AO.52.001248.

[91] W. Ni *et al.*, "Ultrathin graphene diaphragm-based extrinsic Fabry-Perot interferometer for ultra-wideband fiber optic acoustic sensing," *Opt. Express*, 2018, doi: 10.1364/oe.26.020758.

[92] B. Cong, K. Kondo, M. Yamakawa, T. Shiina, T. Nakajima, and Y. Asao, "A fast acoustic field mapping approach based on fabry-perot sensor with high-speed camera," *IEEJ Trans. Electr. Electron. Eng.*, 2014, doi: 10.1002/tee.21996.

[93] Q. Wu, Y. Okabe, and F. Yu, "Ultrasonic structural health monitoring using fiber bragg grating," *Sensors (Switzerland)*. 2018. doi: 10.3390/s18103395.

[94] Z. Ren, Z. Wang, F. Stern, C. Judge, and C. Ikeda-Gilbert, "Vertical water entry of a flexible wedge into calm water: A fluid–structure interaction experiment," *J. Sh. Res.*, vol. 63, no. 1, 2019, doi: 10.5957/JOSR.09180087.